# Age of Air and the Circulation of the Stratosphere

by

Marianna Katherine Linz

A.B., Harvard University, 2011

Submitted to the Joint Program in Oceanography/Applied Ocean Science & Engineering
in partial fulfillment of the requirements for the degree of

Doctor of Philosophy

at the

MASSACHUSETTS INSTITUTE OF TECHNOLOGY

and the

WOODS HOLE OCEANOGRAPHIC INSTITUTION

September 2017



Author ... Signature redacted .....
Joint Program in Oceanography
Massachusetts Institute of Technology
& Woods Hole Oceanographic Institution
July 17, 2017

Certified by.. Signature redacted .....
R. Alan Plumb
Professor Emeritus of Meteorology
Massachusetts Institute of Technology
Thesis Supervisor

Accepted by .... Signature redacted .....
Larry J. Pratt
Chair, Joint Committee for Physical Oceanography
Woods Hole Oceanographic Institution

**Age of Air and the Circulation of the Stratosphere**

by

Marianna Katherine Linz

Submitted to the Joint Program in Oceanography
Massachusetts Institute of Technology
& Woods Hole Oceanographic Institution
on July 17, 2017, in partial fulfillment of the
requirements for the degree of
Doctor of Philosophy

## Abstract

The circulation of air in the stratosphere is important for the distribution of radiatively-important trace gases, such as ozone and water vapor, and other chemical species, including ozone-depleting chlorofluorocarbons. Age of air in the stratosphere is an idealized tracer with unique mathematical properties, which we exploit to derive a theory for the relationship of tracer observations to the stratospheric circulation. We show that the meridional age gradient is a measure of the global diabatic circulation, the total overturning strength through an isentropic surface, and test this time-dependent theory in a simple atmospheric general circulation model. We apply the theory to satellite data of sulfur hexafluoride ($SF_6$) and nitrous oxide to derive the first observationally-based estimates of the global meridional overturning circulation strength at all levels in the stratosphere. These two independent global satellite data products agree to within 5% on the strength of the diabatic circulation in the lower stratosphere. We compare to reanalyses and find broad agreement in the lower stratosphere and disagreement ($\sim$ 100%) in the upper stratosphere. To understand the relationship between the diabatic circulation and other metrics of the circulation, we calculate it in a state-of-the-science atmospheric model and in three different reanalysis data products. The variability of the global diabatic circulation is very similar to one typical circulation metric, and it is correlated with total column ozone in the tropics and in Southern hemisphere midlatitudes in both a model and in reanalysis–data comparisons. Furthermore, we develop a metric for the mean adiabatic mixing, showing that it is related to the meridional age difference and the vertical gradient of age. We calculate this metric for a range of simple model runs to determine its utility as a measure of mixing. We find very little mixing of air into the tropics in the mid-stratosphere, and the vertical structure of mixing in the lower stratosphere and upper stratosphere varies among model runs and between hemispheres. A picture of global average stratospheric circulation could thus be obtained using age of air data, given reliable long-term records.

Thesis Supervisor: R. Alan Plumb
Title: Professor Emeritus of Meteorology
Massachusetts Institute of Technology

## Acknowledgments

Funding for this thesis was provided by the National Defense Science and Engineering Graduate fellowship. This work was supported in part by the National Science Foundation grant AGS-1547733 to MIT.

I would like to thank Alan for your patience and guidance, my committee for sharing their wisdom and expertise, my collaborators—Ailson Ming, Diane Ivy, Douglas Kinnison, Marta Abalos, Gabriele Stiller and Florian Haenel—my group, my officemates throughout the years and all of the fantastic PAOC community. My peers, past and present, have provided advice, friendship, and support. I thank Marena Lin, my doppelganger and sock broker; Camiller Leibler for the many hours of writing together and for always listening to me; Erin Wells-Weiss for being my surrogate older sister, therapist, and role model; Lindsy Peterson for your relentless positivity; my many other friends, who have always believed in me even when I've doubted myself. I would like to thank WiXII for giving me hope, my bridge team and especially my partner Becca Wernis, and the MIT Glass Lab.

I would like to thank my brother for inspiring to be a physicist.
I would like to thank my parents for their love and support.
My most sincere thanks goes to Peter for everything.

# Contents

# Chapter 1

# Introduction

Understanding the circulation of the stratosphere has developed through observations of trace gases. In 1929, Dobson tried to explain the ozone distribution in the atmosphere, writing, "The only way we could reconcile the observed high ozone concentration in the Arctic spring and the low concentration within the Tropics with the hypothesis that the ozone is formed by the action of sunlight, would be to suppose a general slow poleward drift in the highest atmosphere with a descent of the air near the Pole." He proceeded to dismiss this idea as unlikely (Dobson et al., 1929). However, in 1949 Brewer hypothesized the meridional overturning circulation from the equator to the pole to explain the observations of water vapor. He had observed extremely low values of water vapor in the stratosphere over England, values not consistent with the temperatures there. Thus he suggested that the water vapor rose into the stratosphere through a colder tropopause and air parcels were mostly dehydrated before moving towards the poles (Brewer, 1949).

Neither meridional motion on a rotating sphere nor vertical motion through a stratified fluid are easily achieved. Zonal motion within a layer is unimpeded by either angular momentum or buoyancy and can happen freely. Meridional motions and vertical motions require forcing, a torque in the former case and diabatic heating in the latter. Both of these are provided by the deposition of pseudo momentum caused by the breaking of planetary scale waves in the stratosphere. These breaking waves also cause a substantial amount of stirring within the isentropic layers; indeed, this is the dominant effect. Thus we arrive at the most basic picture of stratospheric circulation: Wave breaking drives rapid isentropic motions that are faster in the zonal than the meridional direction; it also causes slow vertical motions and associated diabatic heating and cooling. The rising of air in the tropics followed by the slow poleward and downward motion has come to be known as the Brewer–Dobson Circulation (BDC).

This thesis serves to build upon the foundations of understanding the stratospheric circulation through trace gas distributions. We have developed the theoretical framework to quantify the circulation strength from the distribution of an idealized stratospheric tracer. By considering the system in the natural vertical coordinate for a stratified fluid, we isolate the adiabatic mixing and the diabatic transport and arrive at new metrics for understanding the circulation. We have quantified the strength of the global overturning circulation from the available satellite data and from state-of-the-art reanalysis products, and we have explored the relationship of our new metrics with the more traditional BDC metrics.

In the remainder of this introduction, I have provided more background, as an extended introduction could be beneficial to some readers. The reader is encouraged to skip to Chapter

2 if they feel sufficiently familiar with the subject area. In Section 1.1, I have described the BDC in more detail and discussed its impact on the troposphere. Section 1.2 provides an introduction to the traditionally used residual mean theory and to the idealized tracer age of air. Section 1.3 reviews the literature on predicted changes to the circulation and the extent to which these have been borne out by observations.

Chapter 2 develops a theory to describe the diabatic circulation of the stratosphere using the idealized age tracer. This theory is then validated in an idealized atmospheric general circulation model. Chapter 3 shows the application of this theory to the available age data from satellites and a comparison to a comprehensive climate model and to the state-of-the-art reanalysis products. By calculating age difference using satellite data, I have calculated the first data-based estimate of the strength of the global diabatic circulation of the stratosphere. Chapter 4 is an exploration of the diabatic circulation and its relationship with more traditional circulation metrics and with ozone. Chapter 5 returns to the theory of Chapter 1 and expands upon it by introducing a relationship between age of air and the adiabatic mixing and by considering the two hemispheres separately. In Chapter 6, I summarize the conclusions of this thesis and discuss the significance of this work for future stratospheric research.

## 1.1 The Brewer–Dobson circulation, trends, and stratospheric impacts on the troposphere

A schematic of the BDC (from Plumb 2007) is presented in Figure 1-1. It shows a two cell structure in the lower stratosphere and a one cell structure in the middle and upper stratosphere. On the left side of the figure is the winter pole. In the stratosphere, above the dark grey line that extends from pole to pole representing the tropopause, the winter pole has a strong vortex associated with the extremely cold temperatures. The interior of this vortex is isolated from lower latitudes, as represented schematically by the thick nearly vertical light grey band. At midlatitudes in the winter hemisphere is the "surf zone" (McIntyre and Palmer, 1984), where wave breaking drives both along and cross isentropic transport and the majority of the air leaving the stratosphere exits through the tropopause (Orbe et al., 2012). The tropics are relatively isolated from this, as represented by the mixing barrier in light grey. In the tropics, diabatic upwelling is the dominant non-zonal motion. Between the tropics and the summer hemisphere is a further mixing barrier. In reality, in the upper stratosphere, the single cell of the circulation extends further into the summer hemisphere than this diagram suggests. In the summer hemisphere, mixing is weak in the upper stratosphere, and in the lower stratosphere, the air that upwells at the tropics returns at midlatitudes. At the summer pole, the zonal winds are weak and typically easterly. For an extensive list of references documenting these behaviors, refer to the review in Plumb (2007).

Models of the stratosphere generally agree that the tropical upwelling from the troposphere into the stratosphere will increase by about 2%/decade in experiments that increase greenhouse gases either by abruptly increasing $CO_2$ or in the medium warming (A1B) scenario implying a strengthening of the overall Brewer–Dobson circulation (Butchart et al., 2006, 2010). The mechanism for this increase in models involves the warming of the troposphere and cooling of the stratosphere strengthening the upper flank of the subtropical jets, causing the critical layers and Rossby wave drag to move upwards, allowing more Rossby wave activity in the lower stratosphere (Shepherd and McLandress, 2011; Garny

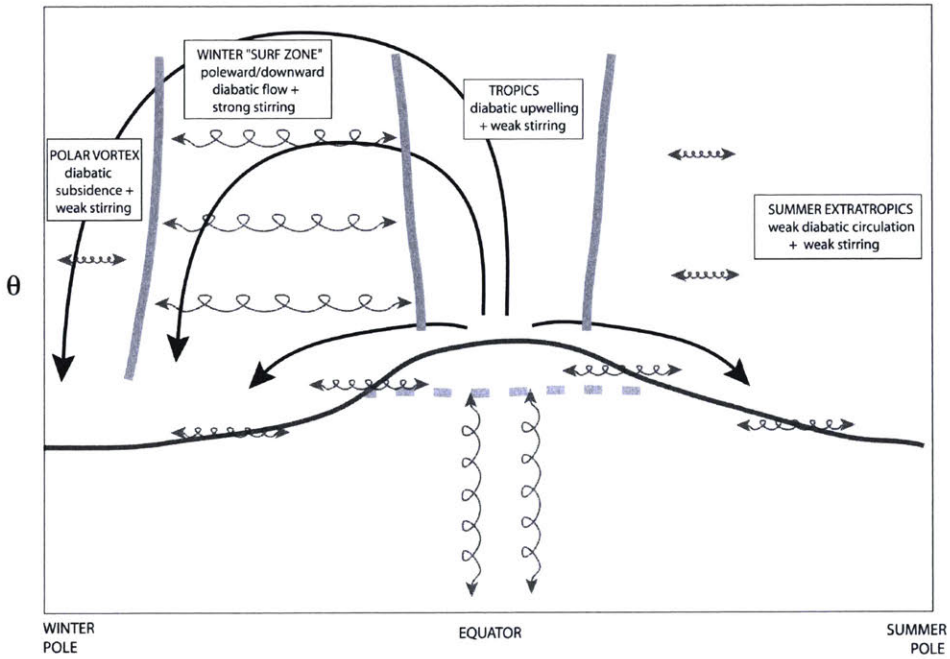


Figure 1-1: Schematic of stratospheric transport from Plumb 2007. The curve that extends across all latitudes is the tropopause and the black lines with arrows represent the meridional residual circulation. The grey bands are transport barriers, and the looped arrows represent along isentropic mixing. The vertical coordinate is $\theta$. See the text for a more detailed discussion

et al., 2011). It has also been suggested that this represents more of a "lifting" of the circulation as the height of the tropopause increases and that the mass circulation is largely unchanged (Oberländer-Hayn et al., 2016). Because the strength of the circulation is typically evaluated at a fixed pressure level, the rising tropopause height and associated rising circulation patterns would appear as an acceleration even if the total mass transport through the stratosphere were to remain unchanged.

The stratospheric circulation can have significant impacts on the troposphere. Dobson proposed the existence of the BDC based on the distribution of stratospheric ozone, which absorbs ultraviolet radiation, warming the surrounding atmosphere. The impact of the ozone distribution on tropospheric dynamics is highlighted by the effects of ozone loss on tropospheric circulation. In the Antarctic, ozone depletion causes a colder pole, leading to a stronger polar vortex that persists longer into the spring (Thompson and Solomon, 2002). Because Rossby waves propagate vertically through weak westerly winds, this also changes the climatology of the wave forcing. The zonal wind responds to the eddy forcing, and then through a positive feedback, the winds then affect the eddy forcing in the troposphere (Lorenz and Hartmann, 2001). A stronger polar vortex is also associated with a poleward shift of the tropospheric jet (Baldwin and Dunkerton, 1999). Polvani et al. (2011) examined in detail the effects of lowering ozone in a model and found that the lower ozone resulted in lower stratospheric cooling with an associated raised tropopause, leading to a) movement

of the midlatitude tropospheric jet poleward, b) a stronger Southern Annular Mode and c) poleward motion of the edge of the Hadley cell. Shifts in circulation are dominated by ozone depletion effects rather than greenhouse gas effects (Polvani et al., 2011). Furthermore, as the ozone hole has begun to recover, the variations in the dynamics have modulated the rapidity of that recovery (Solomon et al., 2016).

The BDC helps determine the exchange between the stratosphere and troposphere as well as the stratospheric distributions of trace gases; as such, it has important implications for climate. Stratospheric water vapor is a greenhouse gas (Forster and Shine, 1999), and a substantial portion of variability in stratospheric water vapor is associated with changes in tropical upwelling (Dessler et al., 2013). Models predict that the strength of the BDC will increase with global warming (e.g. McLandress and Shepherd, 2009; Butchart et al., 2010; Garcia and Randel, 2008), and thus this effect would tend to enhance the warming, acting as a positive feedback. Meanwhile, the impact of the changing BDC on climate through ozone is two-fold. Ozone in the troposphere is a strong greenhouse gas, but ozone in the stratosphere has a cooling effect (Forster et al., 2007). It has been predicted that stratospheric ozone transport into the troposphere will increase with global warming (Hegglin and Shepherd, 2009), which could serve to enhance warming both due to the increase in upper-tropospheric ozone and a decrease in stratospheric ozone. Decadal variations in lower stratospheric water vapor have changed the rate of global temperature increase over the past few decades (Solomon et al., 2010), demonstrating that stratospheric water vapor has an important impact on surface climate.

## 1.2 Theoretical background: age of air and the residual mean circulation

The "age" of air describes how long an air parcel has been in the stratosphere since it entered at the tropopause (Hall and Plumb, 1994). Of course, there are many different pathways traveled by the bits of air that make up the parcel, and so more accurately, any air parcel can be described by an age spectrum, which describes the statistical distribution of ages of air at a given location (Kida, 1983). A mathematical formulation for the age spectrum was developed by Hall and Plumb (1994), treating the age spectrum as a Green's function that propagates the tropopause variations of a tracer into the stratosphere. For completeness, the formulation for age from a linearly increasing tracer (Hall and Plumb, 1994) is included here.

A conservative tracer satisfies

$$\frac{\partial n}{\partial t} + \mathcal{L}(n) = 0, \tag{1.1}$$

where $n$ is the mixing ratio and $\mathcal{L}$ is the full advection-diffusion operator. We treat the transport described by $\mathcal{L}$ as stationary in time. If $n = n(P,t)$ is known at location $P_0$ and some time $t$ and $n(P_0,t) = 0$ for $t < 0$, then at some other point, the mixing ratio is given by

$$n(P,t) = \int_0^t n(P_0, t-t')G(P,P_0,t')dt', \tag{1.2}$$

where $G$ is the Green's function that satisfies the condition that if $n(P_0,t) = \delta(t-t_0)$, then $n(P,t) = G(P,P_0,t-t_0)$. The integral over all time of the Green's function $G(P,P_0,t)$ is 1.

The tracer mixing ratio is assumed to be known at the tropical tropopause, $P_0$. The

Green's function is the age spectrum or the distribution of transit times within a parcel. Then the age is

$$\Gamma(P, P_0) = \int_0^\infty tG(P, P_0, t)dt. \tag{1.3}$$

When the air travels with no mixing, $G = \delta(t - t_0)$, so $\Gamma = t_0$ and this is simply the transit time. In this case,

$$n(P, t) = n(P_0, t - \Gamma). \tag{1.4}$$

When the age spectrum has finite width and the tracer concentration is linearly growing in time at $P_0$,

$$n(P_0, t) = \gamma t, \ t > 0, \tag{1.5}$$

then (1.2) yields

$$n(P, t) = n(P_0, t) \int_0^t G(P, P_0, t')dt' - \gamma \int_0^t t'G(P, P_0, t')dt'. \tag{1.6}$$

As $t \to \infty$, this gives once again the result when there was no mixing, from (1.4). This limit is valid when integrating beyond the transient response of the system, and so when there is a linearly growing source that has been linearly growing for long enough, then the age of the air is equivalent to the lag time. For a discussion of an exponentially growing tracer and a periodic tracer, see Hall and Plumb (1994). Holzer and Hall (2000) generalized this theory to have explicit sources rather than particular mixing ratios at the boundary.

A reformulation of this theory was used by Neu and Plumb (1999) after being brought to light by Boering et al. (1996). Now instead of this conserved tracer, consider a tracer that has a source of one unit per unit time, an "ideal age", $\Gamma_i$. The evolution will be governed by

$$\frac{\partial \Gamma_i}{\partial t} + \mathcal{L}(\Gamma_i) = 1, \tag{1.7}$$

with $\Gamma_i = 0$ at the surface (Waugh and Hall, 2002). This is equivalent to the mean of the age spectrum: taking the time average of (1.1) with the Green's function $G$ with the surface boundary condition $\delta(t)$ results in (1.7).

The first moment of the age spectrum is known as the mean age in the literature. Considering the wide variety of averaging calculations that are involved in this document, however, I will refer to this "mean age" simply as the age and specify when I refer to a spectrum instead of this mean.

Ideal age of air records the transport of the various components of a parcel of air and as such provides a full description of the transport circulation of the stratosphere. Age has been used extensively as a model evaluation tool (e.g. Hall et al. 1999) and the age has been linked with the overall strength of the stratospheric circulation (Austin and Li, 2006). The mean of the age spectrum is a mean of a right-tailed distribution and thus is a biased estimate of the median transit time realized by the majority of air parcels. Nevertheless, if a model were to produce the age distribution of the stratosphere perfectly correctly, it would necessarily be representing the transport circulation of the real world correctly as well. When a model does not reproduce the correct age distribution, however, it is not straightforward to diagnose why. Even if a model did get the age distribution perfectly correct, it could be doing so for the wrong reasons, getting the wave forcing magnitude correct but the source incorrect. Relating age to the dynamical variables more commonly used by modelers is thus a priority.

As it has been described from tracers, the BDC encompasses the Lagrangian-mean mass transport, and thus the relevant horizontal and vertical velocities are not the Eulerian velocity fields. The standard approach is to use the transformed Eulerian mean residual velocities, $\bar{v}^*$ and $\bar{w}^*$, (Andrews and McIntyre, 1976; Andrews et al., 1987) to approximate the mean Lagrangian meridional transport. These are defined (Andrews and McIntyre, 1976):

$$\bar{v}^* = \bar{v} - \left(\overline{v'\theta'}/\bar{\theta}_z\right)_z, \tag{1.8}$$

and

$$\bar{w}^* = \bar{w} + \left(\overline{v'\theta'}/\bar{\theta}_z\right)_y. \tag{1.9}$$

The bar denotes a zonal average, and the primes are deviations from this. $\theta$ is the potential temperature, and the subscripts are derivatives. This formulation creates a mean thermodynamic equation that does not depend on the eddies for quasigeostrophic flow and a zonal momentum equation in which the divergence of the Eliassen-Palm flux acts a body force and is the only representation of the eddy component of the flow. This treatment also has the advantage of being equivalent to the density-weighted isentropic mean circulation for adiabatic, small-amplitude eddies. The residual circulation is therefore a dynamically useful way to describe the stratospheric circulation, reflecting both the dynamical forcing by eddies and the mass transport.

In an ideal case, a tracer could be directly related to the transport: a tracer with a linearly increasing (in time) concentration at the tropical tropopause that purely underwent advection along the residual mean circulation would give a simple estimate of the transit time from the tropical tropopause to any point in the stratospheric interior and thus define the residual circulation exactly. Age does not simply follow the zonal mean trajectories, however, and this makes it a fundamentally different measure of the circulation than the residual circulation. Any time spent moving exclusively in the third dimension (zonal) or moving back and forth meridionally, that is to say any time spent "mixing", will make the age of air older than if it were purely following the residual circulation trajectories. Garny et al. (2014) demonstrate this by comparing idealized mean age of air to transit times for parcels purely following the residual circulation, finding that the mean age is greater than the transit time in the midlatitudes and less than the transit time at high latitudes and low altitudes, where they infer mixing with tropospheric air. The mean age is therefore an imperfect proxy for the residual circulation.

Alternatively, if the transport circulation—that is the circulation that is felt by and transports trace gases—and not the residual circulation is the quantity of interest, age of air potentially contains the necessary information as it is a representation of the full histories of the air parcels; the difficulty lies in disentangling that information such that we can understand physically its relationship to the dynamical terms output by a model. This thesis has developed a way to use the age distribution to understand both the diabatic and adiabatic circulation.

## 1.3 Tracer observations

The idealized age of air tracer is zero at the tropopause and ages at a rate of 1 year/year while it is in the stratosphere. As discussed above, the theory for age of air also applies to a tracer with a concentration that is linearly increasing in time at the tropical tropopause and then is conserved in the stratosphere, known as a "clock" tracer. Two species that roughly

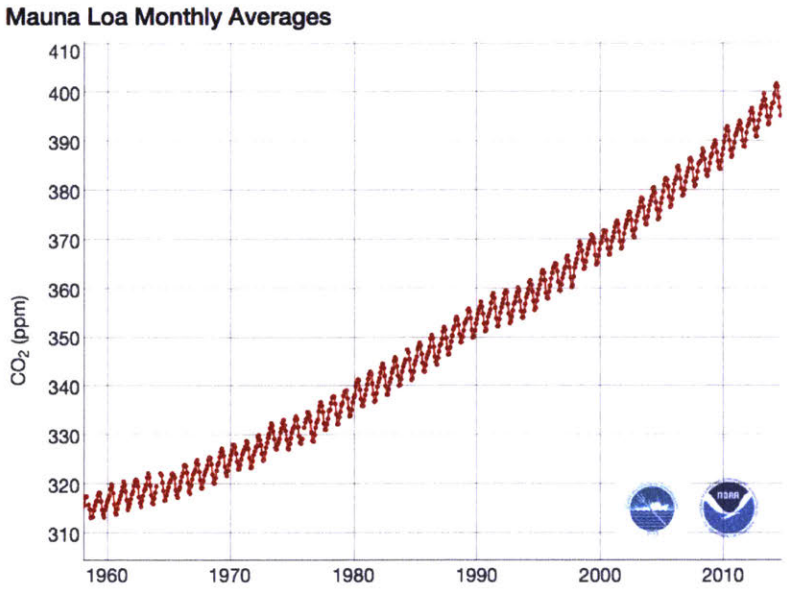


Figure 1-2: Measurements of monthly averaged $CO_2$ from Mauna Loa (http://www.esrl.noaa.gov/gmd/ccgg/trends/graph.html)

match that description are carbon dioxide ($CO_2$) and sulfur hexafluoride ($SF_6$). These both have a seasonal cycle and have long term behavior that is nonlinear, but they are close to linear for recent years. In calculating age from these tracers, the nonlinear behavior of the annual average $CO_2$ and $SF_6$ can be corrected for, and generally the impact of this nonlinearity is small (Garcia et al., 2011). The time series of $CO_2$ observations at Mauna Loa is shown in Figure 1-2, demonstrating the nonlinearity. $CO_2$ has a strong seasonal cycle, much stronger than that for $SF_6$. This seasonal cycle impacts the estimation of age from $CO_2$, especially in the lower stratosphere. $SF_6$ has a sink in the mesosphere, which complicates its interpretation in the uppermost stratosphere. Together, global observations of these two species would present a robust picture of age of air in the stratosphere.

Since the introduction of the concept of stratospheric age of air, tracers have been used to estimate ages and age spectra. A linear combination of water vapor and methane concentrations yields the total hydrogen tracer, which is conserved upon entry into the stratosphere and was used by Johnson et al. (1999) to estimate the age spectrum, combining satellite data with balloon measurements. This method relied on the assumption that the transport is independent of time, however, and the seasonal cycle and interannual variability of transport are actually quite strong (Orbe et al., 2014). Long-lived stratospheric tracers, those with lifetimes longer than the adiabatic transport time scales, share mixing ratio isopleths and are related by compact relationships; those with lifetimes greater than the diabatic transport time scales are related by linear relationships and can be used to predict each other (Plumb and Ko, 1992). Characterizing these compact relationships can give additional information about age (e.g. Andrews et al., 2001).

Mostly, however, researchers have used measurements of the clock tracers to calculate age. A summary of high altitude balloon measurements was made by Engel et al. (2009), with measurements of $SF_6$ and $CO_2$ from 27 balloon flights that indicated a trend of $+0.24$

$\pm 0.22$ years/decade for air above 24 km, implying there has been no detectable trend over the last 30 years. This estimate is limited by the sparse spatial and temporal coverage of the observations, and a transformative development in the study of age of air is global coverage provided by satellites. The Michelson Interferometer for Passive Atmospheric Sounding (MIPAS) instrument, which was on the Environmental Satellite (Envisat) in sun-synchronous orbit, provided a decade of $SF_6$ measurements. The analysis of the MIPAS $SF_6$ data from 2002 to 2010 indicates a linear trend of increasing age of air at 25 km of +0.59 years/decade (Stiller et al., 2012). The increase in age of air might suggest a slowing of the Brewer–Dobson circulation, although the spatial patterns of the trends suggest a more complicated story and are qualitatively consistent with a strengthening of the mean circulation and a weakening of the mixing barriers. Recent work has shown that records of 30 years are necessary to statistically significantly detect a 2%/decade trend from the background variability in the BDC (Hardiman et al., 2017), and so studies of periods shorter than this do not reflect the long-term trend associated with global warming.

This thesis serves to create a framework for understanding the relationship between the circulation and age of air from tracer observations in a quantitative way. In Chapter 3, I have reexamined the MIPAS data and used the compact relationship of $N_2O$ with age to derive the a novel observationally-based calculation of the strength of the global overturning circulation of the stratosphere.

# Chapter 2

# The relationship between age of air and the diabatic circulation of the stratosphere

This chapter was published as Marianna Linz, R. Alan Plumb, Edwin P. Gerber, Aditi Sheshadri, 2016: The Relationship between Age of Air and the Diabatic Circulation of the Stratosphere. J. Atmos. Sci., 73, 4507–4518, doi: 10.1175/JAS-D-16-0125.1.  ML performed the research and wrote the manuscript, under the supervision of AP. EG and AS assisted by providing model output and guidance.

## 2.1 Introduction

The Brewer–Dobson circulation (BDC) is the slow meridional overturning circulation of the stratosphere, consisting of upwelling through the tropical tropopause then poleward motion and downwelling through the midlatitudes and at the poles. This circulation is critical for the vertical transport of tracers such as ozone, volcanic aerosols, and CFCs; for the temperature of the tropical tropopause and consequently the amount of water vapor in the stratosphere; and for stratosphere–troposphere exchange (e.g. Butchart 2014, and references therein). Stratosphere–resolving climate models show a positive trend in the BDC—an increase in the tropical upwelling at a fixed pressure level—as a robust response to increasing greenhouse gases (Butchart et al., 2006; Hardiman et al., 2014). This increasing trend in the residual circulation, however, might better be described as a "lifting" trend, associated with the upward expansion of the tropopause (and entire tropospheric circulation) in response to global warming (Singh and O'Gorman, 2012; Oberländer-Hayn et al., 2016). Reanalysis products are in qualitative agreement with the climate models, showing positive trends over the period 1979–2012, but with differing spatial structures for each individual product (Abalos et al., 2015). Satellite-derived temperature trends are also consistent with the model predictions (Fu et al., 2015).

The mean age of air (Hall and Plumb, 1994; Waugh and Hall 2002) has been used as a metric for models' ability to reproduce the stratospheric circulation (e.g., Hall et al. 1999; Butchart et al. 2011). The apparent increase in the residual circulation has led to predictions that the mean age of air should decrease. Attempts to identify trends of decreasing age of air from observations of transient tracers in the stratosphere have found little evidence; in fact age appears to be mostly increasing (Engel et al., 2009; Stiller et al., 2012; Haenel et al., 2015). However, for one thing, available data records are short enough — global satellite coverage of age tracers is available for less than a decade — that apparent trends could be indicative of interannual variability rather than of long-term trends (cf. Garcia et al. 2011). Moreover, mean age is a statistical average over many transport pathways (Hall and Plumb, 1994), and at a given location it depends on mixing processes and not just mean advection (Waugh and Hall, 2002; Garny et al., 2014; Ploeger et al., 2015a). Satellite observations of $SF_6$ have been used to identify spatially inhomogeneous trends in age between 2002–2012 (Stiller et al., 2012; Haenel et al., 2015), and while these trends can be compared to model output, for which the contributions of advection and mixing can be isolated (Ploeger et al., 2015b), in reality they are difficult to disentangle (Ray et al., 2010).

There are certain aspects of the stratospheric age distribution that are dependent on the mean circulation alone. Using a "leaky tropical pipe" model, Neu and Plumb (1999) showed that, in steady state, the tropics–midlatitude age difference on an isentrope depends only on the overturning mass flux and is independent of isentropic mixing, provided that diabatic mixing is negligible. This result has been used to assess transport in chemistry–climate models (Strahan et al., 2011). Here we present a generalization of this analysis. In Section 2.2.1 we show that the steady–state result of a simple and direct relationship between age gradient and overturning diabatic mass flux holds even in the absence of a "tropical pipe," provided the isentropic age gradient is defined appropriately. For the more realistic case of an unsteady circulation, we show in Section 2.2.2 that the result holds for the time average; in Section 2.2.3, the fully transient case is discussed. The accuracy of the theoretical predictions is demonstrated in Section 2.3 using results from a simple general circulation model; the theory works well when applied to multi-year averages, though there are systematic discrepancies which appear to indicate a role for large–scale diabatic diffusion.

Applications and limitations of the theory are discussed in Section 2.4.

## 2.2 Age difference theory

A passive tracer $\chi$ follows the tracer continuity equation

$$\frac{\partial \chi}{\partial t} + \mathcal{L}(\chi) = \mathcal{S}, \tag{2.1}$$

where $\mathcal{L}$ is the advection–diffusion operator and $\mathcal{S}$ is the source. For the stratospheric age tracer, $\Gamma$, the source is 1 (year/year) with a boundary condition of $\Gamma = 0$ at the tropopause. In equilibrium, age determined from a conservative tracer ($\mathcal{S} = 0$) with a boundary condition that is linearly growing at the tropopause will be equivalent to the age tracer $\Gamma$ (Waugh and Hall, 2002). Considering the tracer continuity equation for the age tracer $\Gamma$ in potential temperature ($\theta$) coordinates, we rewrite the full advection–diffusion operator as the divergence of a flux to obtain,

$$\frac{\partial}{\partial t}(\sigma\Gamma) + \nabla \cdot \mathbf{F}^{\Gamma} = \sigma, \tag{2.2}$$

where $\sigma = -\frac{1}{g}\frac{\partial p}{\partial \theta}$ is the isentropic density and $\mathbf{F}^{\Gamma}$ is the advective–diffusive flux of age.

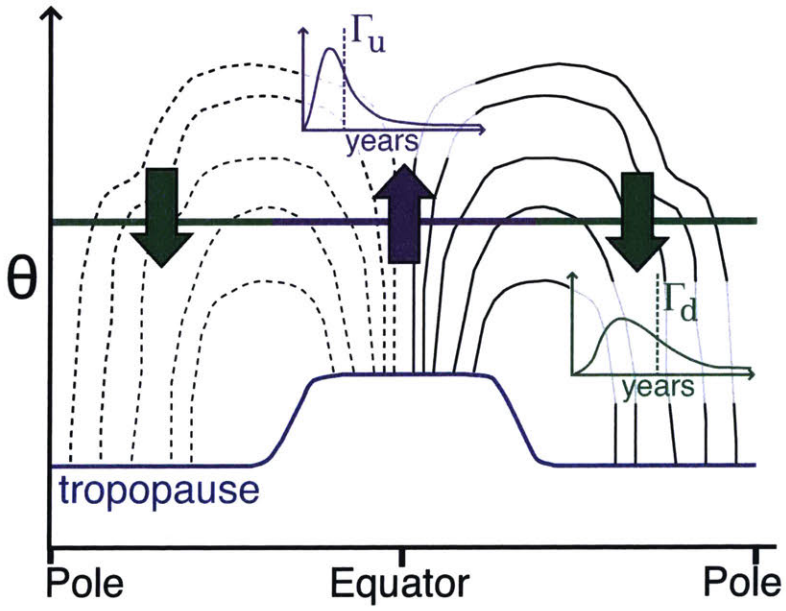


Figure 2-1: A schematic diagram of the time–average circulation of the stratosphere, and the overturning through one isentrope. The diabatic circulation streamfunction is sketched in the black contours. The upwelling region of the isentrope is colored purple and the downwelling region is colored green. In the insets, the age spectra are shown schematically for the upwelling and downwelling air, along with the means, $\Gamma_u$ and $\Gamma_d$. Based on a similar diagram in Waugh and Hall (2002).

### 2.2.1 Steady–state

In a steady state, integrating (2.2) over the volume $\mathcal{V}$ above any surface $\mathcal{S}$ shows that

$$\int_{\mathcal{S}} \mathbf{n} \cdot \mathbf{F}^{\Gamma} dA = \int_{\mathcal{V}} \sigma dA d\theta = \int_{\mathcal{V}} \rho dV, \tag{2.3}$$

where $\mathbf{n}$ is the downward unit normal to the surface $\mathcal{S}$ and assuming hydrostatic balance. The net age flux through a surface is equal to the mass above that surface, so that, for example, the age flux through the tropopause is equal to the mass of the stratosphere and the rest of the atmosphere above (Volk et al., 1997; Plumb, 2002).

Let us choose $\mathcal{S}$ to be an isentropic surface that is entirely within the stratosphere. If the motions are strictly adiabatic, isentropic stirring will cause no flux through the surface. Assuming diabatic diffusion of age is negligible, the diabatic transport is entirely advective, and (2.3) gives

$$\int_{\theta} \sigma \dot{\theta} \Gamma dA = -M(\theta), \tag{2.4}$$

where $\int_{\theta}$ is the integral over the $\theta$ surface and $M(\theta) = \int_{\mathcal{V}} \rho dV$ is the mass above the $\theta$ surface. We define the mass–flux–weighted age of upwelling and downwelling air as

$$\Gamma_u(\theta) = \left[\int_{up} \sigma \dot{\theta} dA\right]^{-1} \int_{up} \sigma \dot{\theta} \Gamma dA, \tag{2.5}$$

and

$$\Gamma_d(\theta) = \left[\int_{down} \sigma \dot{\theta} dA\right]^{-1} \int_{down} \sigma \dot{\theta} \Gamma dA. \tag{2.6}$$

where $\int_{up}$ and $\int_{down}$ are integrals over the portion of the area of the isentropic surface through which air is upwelling and downwelling respectively as shown in Figure 5-1. Although this schematic is for a zonal mean, the regions are defined in two dimensions and not simply by the zonal mean turnaround latitudes. While the schematic shows upwelling in the tropics and downwelling in the extratropics, nothing in the derivation presented here requires any particular structure for the diabatic circulation, provided only that it is nonzero.

In equilibrium under steady–state conditions, the mass flux through the upwelling and downwelling areas must be equal, and let this be called $\mathcal{M}(\theta)$:

$$\int_{up} \sigma \dot{\theta} dA = -\int_{down} \sigma \dot{\theta} dA = \mathcal{M}(\theta). \tag{2.7}$$

Then

$$\int_{up} \sigma \dot{\theta} \Gamma dA = \mathcal{M} \Gamma_u; \tag{2.8}$$

$$\int_{down} \sigma \dot{\theta} \Gamma dA = -\mathcal{M} \Gamma_d. \tag{2.9}$$

The global integral in (2.4) is the sum of (2.8) and (2.9):

$$\int_{\theta} \sigma \dot{\theta} \Gamma dA = \mathcal{M} \left(\Gamma_u - \Gamma_d\right) = -M(\theta), \tag{2.10}$$

which can be rewritten as

$$\Delta\Gamma(\theta) = \Gamma_d(\theta) - \Gamma_u(\theta) = \frac{M(\theta)}{\mathcal{M}(\theta)}. \tag{2.11}$$

Thus, the gross mass–flux–weighted age difference, as defined by (2.11), (2.5), and (2.6), between downwelling and upwelling air is simply the ratio of the mass above the isentrope to the mass flux through it, i.e. the gross residence time of the air above the surface.

This relationship is essentially identical to that obtained by Neu and Plumb (1999) in their tropical pipe model, but the present approach avoids assumptions made in that model, other than steadiness and the neglect of diabatic diffusion (which will both be addressed in the following sections). As discussed by those authors (and by Plumb 2002 and Waugh and Hall 2002), (2.11) is remarkable and counter–intuitive in that the gross isentropic age gradient is independent of isentropic mixing (except insofar as the mixing of potential vorticity drives the diabatic circulation) and depends only on the overturning mass flux through the $\theta$ surface—it is independent of path in the diabatic circulation. For a given mass flux, the age gradient is the same whether the circulation is deep or shallow.

The potential power of (2.11) lies in the fact that, unlike age itself, $\Delta\Gamma$ is a measure of the age distribution that is directly dependent only on the overturning mass flux and hence provides a tracer–based means of quantifying the strength of the circulation. The one isentrope on which the age itself is relevant is that which skims the tropical tropopause; there $\Gamma_u \approx 0$ and so $\Gamma_d \approx \Delta\Gamma$. Below this isentrope (i.e. in the "lowermost stratosphere"), (2.11) is no longer applicable as the assumptions made (in particular, the neglect of diabatic diffusion) do not apply where portions of the isentropes are below the tropopause.

### 2.2.2 Time–average

The atmosphere is not in steady state; the stratospheric circulation varies on synoptic, seasonal, and interannual timescales. We can instead consider the time–average age equation. The time derivative in (2.2) goes to zero for a long enough averaging period, provided the trends are small. Then (2.4) becomes

$$\overline{\int_\theta \sigma\dot{\theta}\Gamma dA}^t = -\overline{M(\theta)}^t, \tag{2.12}$$

where $\overline{\phantom{x}}^t$ is the time mean. We can define the time–average mass–flux–weighted age of upwelling and of downwelling air as:

$$\Gamma_{\overline{u}}(\theta) = \left[\overline{\int_{\overline{up}^t} \sigma\dot{\theta}dA}^t\right]^{-1} \overline{\int_{\overline{up}^t} \sigma\dot{\theta}\Gamma dA}^t , \tag{2.13}$$

and

$$\Gamma_{\overline{d}}(\theta) = \left[\overline{\int_{\overline{down}^t} \sigma\dot{\theta}dA}^t\right]^{-1} \overline{\int_{\overline{down}^t} \sigma\dot{\theta}\Gamma dA}^t , \tag{2.14}$$

where now the upwelling region is defined by where the time–average diabatic vertical velocity is positive ($\overline{\dot{\theta}}^t > 0$). When we equivalently define the mass flux

$$\overline{\int_{\overline{up}^t} \sigma\dot{\theta}dA}^t = -\overline{\int_{\overline{down}^t} \sigma\dot{\theta}dA}^t = \overline{\mathcal{M}(\theta)}^t, \tag{2.15}$$

this allows us to write (2.12) as

$$\overline{\int_\theta \sigma\dot{\theta}\Gamma dA}^t = \overline{\mathcal{M}}^t \left(\Gamma_{\overline{u}} - \Gamma_{\overline{d}}\right) = -\overline{M(\theta)}^t, \tag{2.16}$$

or

$$\left(\Gamma_{\overline{d}} - \Gamma_{\overline{u}}\right) = \frac{\overline{M(\theta)}^t}{\overline{\mathcal{M}}^t}. \tag{2.17}$$

With time–averaging, we thus recover the form of the result from the steady–state theory.

Although this derivation has been done for upwelling and downwelling regions, the time–average formulation does not require the two regions of the isentrope to be strictly upwelling or downwelling. As long as the isentrope is split into only two regions which together span the surface, any division will do. The overturning mass flux $\overline{\mathcal{M}(\theta)}^t$ will be the net mass flux up through one region and down through the other. For example, the "upwelling" could be defined as 20°S–20°N and the "downwelling" the rest of the isentrope. The difference between the mass–flux–weighted age averaged over the area outside of 20°S–20°N and averaged over the area within 20°S–20°N would give the total overturning mass flux through those regions. Because some of the true upwelling is now in the "downwelling" region, the total overturning mass flux between these two regions will be necessarily less than the true total overturning mass flux through the surface. We will demonstrate this and discuss further in Section 2.3. We emphasize that the "age difference" in all of these cases is based on the mass–flux–weighted average ages; hence in principle, it is necessary to know the circulation in order to accurately calculate the age difference as defined here.

### 2.2.3 Time–varying

Here we use a different approach that allows us to look at seasonal variability and fully account for time variations. The upwelling and downwelling mass fluxes are not necessarily equal, and the mass above the isentrope may be changing. The age at a given location can also change in time. Returning to the ideal age equation, (2.2), integrating over the volume above an isentropic surface, there is now an additional time–dependent term:

$$\int_\theta \sigma\dot{\theta}\Gamma dA = -M(\theta) + \frac{\partial}{\partial t}\left[\int \Gamma dM\right], \tag{2.18}$$

where

$$\int \Gamma dM = \int_{\mathcal{V}} \sigma\Gamma dA d\theta \tag{2.19}$$

is the mass–integrated age above the isentrope. This term accounts for fluctuations in the mass–weighted total age above the isentrope. If the mass above the isentrope is varying in time,

$$\mathcal{M}_d + \mathcal{M}_u = \frac{\partial M}{\partial t}. \tag{2.20}$$

The upwelling and downwelling regions can also be varying in time and must now be defined instantaneously. Define the total overturning circulation

$$\mathcal{M}(\theta) = (\mathcal{M}_u - \mathcal{M}_d)/2, \tag{2.21}$$

recalling that $\mathcal{M}_u > 0$ and $\mathcal{M}_d < 0$ so that $\mathcal{M}(\theta)$ is always positive. From (2.20) and (2.21) we write

$$\mathcal{M}_u = \mathcal{M}(\theta) + \frac{1}{2}\frac{\partial M}{\partial t}, \tag{2.22}$$

and

$$\mathcal{M}_d = -\mathcal{M}(\theta) + \frac{1}{2}\frac{\partial M}{\partial t}. \tag{2.23}$$

Then we rewrite the flux equations, (2.8) and (2.9):

$$\int_{up} \sigma\dot{\theta}\Gamma dA = \mathcal{M}_u\Gamma_u = \Gamma_u\left[\mathcal{M}(\theta) + \frac{1}{2}\frac{\partial M}{\partial t}\right], \tag{2.24}$$

and

$$\int_{down} \sigma\dot{\theta}\Gamma dA = \mathcal{M}_d\Gamma_d = -\Gamma_d\left[\mathcal{M}(\theta) - \frac{1}{2}\frac{\partial M}{\partial t}\right]. \tag{2.25}$$

As in the steady–state case, the net global flux is the sum of these two. Using (2.18), the time–dependent version of (2.10) is

$$\mathcal{M}\Delta\Gamma - M = -(M\Gamma_s)_t + \frac{1}{2}(\Gamma_u + \Gamma_d)\frac{\partial M}{\partial t}, \tag{2.26}$$

where $\Delta\Gamma = \Gamma_d - \Gamma_u$ as before, and

$$\Gamma_s(\theta) = \frac{1}{M}\int_\theta \Gamma dM \tag{2.27}$$

is the mean age of air above the isentrope. The two terms on the right side of (2.26) arise because the time–derivatives are no longer zero. Throughout the rest of the paper, these two terms will be collectively referred to as the "time–derivative terms."

The balance expressed by (2.26) should hold true at any time. However, averaging over a year or several years will make the time derivatives smaller, as the high frequency variability and seasonal cycle are stronger than the interannual variability. The time derivatives will now be expressed with a subscript. Rearranging and taking the time average gives

$$\overline{\mathcal{M}\Delta\Gamma}^t = \overline{M}^t - \overline{(M\Gamma_s)_t}^t + \frac{1}{2}\overline{M_t(\Gamma_u + \Gamma_d)}^t. \tag{2.28}$$

Separating the overturning, $\mathcal{M}$, and the age difference, $\Delta\Gamma$, into time mean components and deviations therefrom ($\mathcal{M} = \overline{\mathcal{M}}^t + \mathcal{M}'$ and $\Delta\Gamma = \overline{\Delta\Gamma}^t + \Delta\Gamma'$) yields

$$\overline{\mathcal{M}}^t\ \overline{\Delta\Gamma}^t = \overline{M}^t - \overline{\mathcal{M}'\Delta\Gamma'}^t - \overline{(M\Gamma_s)_t}^t + \frac{1}{2}\overline{M_t(\Gamma_u + \Gamma_d)}^t, \tag{2.29}$$

or

$$\overline{\Delta\Gamma}^t = \frac{\overline{M}^t}{\overline{\mathcal{M}}^t} - \frac{\overline{\mathcal{M}'\Delta\Gamma'}^t}{\overline{\mathcal{M}}^t} - \frac{\overline{(M\Gamma_s)_t}^t}{\overline{\mathcal{M}}^t} + \frac{1}{2}\frac{\overline{M_t(\Gamma_u + \Gamma_d)}^t}{\overline{\mathcal{M}}^t}. \tag{2.30}$$

If the time–derivative terms and the term involving fluctuations, $\overline{\mathcal{M}'\Delta\Gamma'}^t$, are small, then we arrive at the same result as in steady state and the age difference is the mean residence time in the region above the isentrope.

Note that this differs from the time–average version of the theory, presented in Section 2.2.2. In the derivation of (2.30), the average of $\Delta\Gamma$ is taken after calculating the mass–flux–weighted upwelling and downwelling ages instantaneously. The time–varying theory is sensitive to the definition of region of upwelling/downwelling, in contrast to the time–average theory, because the instantaneous mass flux averaged over either the upwelling or downelling region could change sign in time. If the flux were zero in one region and nonzero in the other, then because of the mass–flux weighting, $\Delta\Gamma$ would be singular. In contrast, the time–average mass flux through a region as defined in (2.17) will be well defined as long as the regions are defined to have nonzero overturning mass flux. The time–varying theory is therefore only appropriate when the upwelling and downwelling regions are defined instantaneously.

## 2.3 Verification in a simple atmospheric GCM

### 2.3.1 Model setup

To verify the theory, we evaluate the terms in (2.11), (2.17), and (2.26) in a simple atmospheric GCM with and without a seasonal cycle. The model is a version of the dynamical core developed at the Geophysical Fluid Dynamics Laboratory (GFDL). It is dry and hydrostatic, with radiation and convection replaced with Newtonian relaxation to a zonally–symmetric equilibrium temperature profile. We use 40 hybrid vertical levels that are terrain–following near the surface and transition to pressure levels by 115 hPa. Unlike previous studies using similar idealized models (e.g. Polvani and Kushner 2002, Kushner and Polvani 2006, Gerber and Polvani 2009, Gerber 2012, Sheshadri et al. 2015), the model solver is not pseudospectral. It is the finite–volume dynamical core used in the GFDL Atmospheric Model Version 3 (AM3; Donner et al. 2011), the atmospheric component of GFDL's CMIP5 coupled climate model. The model utilizes a cubed–sphere grid (Putnam and Lin, 2007) with "C48" resolution, where there is a 48×48 grid on each side of the cube, and so roughly equivalent to a $2° \times 2°$ resolution. Before analysis, all fields are interpolated to a regular latitude–longitude grid using code provided by GFDL.

In the troposphere, the equilibrium temperature profile is constant in time and similar to Held and Suarez (1994) with the addition of a hemispheric asymmetry in the equilibrium temperature gradient that creates a colder Northern Hemisphere (identical to Polvani and Kushner 2002). In the polar region (50°–90° N/S), the equilibrium temperature profile decreases linearly with height with a fixed lapse rate of $\gamma$, which sets the strength of the stratospheric polar vortex. The stratospheric thermal relaxation timescale is 40 days. As an analog for the planetary scale waves generated by land–sea contrast, flow over topography, and nonlinear interactions of synoptic scale eddies, wave–2 topography is included in the Northern Hemisphere at the surface centered at 45°N as in Gerber and Polvani (2009). The Southern Hemisphere has no topography. As in Gerber (2012), a "clock" tracer is specified to increase linearly with time at all levels within the effective boundary layer of the Held and Suarez (1994) forcing (model levels where $p/p_s = 0.7$) and is conserved otherwise, providing an age of air tracer.

The seasonally–varying run has a seasonal cycle in the stratospheric equilibrium temperature profile following Kushner and Polvani (2006), with a 360 day year consisting of a

| | configuration | $\gamma$ (K/km) | h (km) |
|---|---|---|---|
| 1 | seasonally–varying | 4 | 4 |
| 2 | perpetual–solstice | 1.5 | 3 |
| 3 | perpetual–solstice | 4 | 4 |
| 4 | perpetual–solstice | 4 | 0 |
| 5 | perpetual–solstice | 5 | 3 |

Table 2.1: Summary of setup for the five runs used in this study. One run has a seasonal cycle as described in the text and the others are perpetual–solstice with varying stratospheric lapse rates ($\gamma$, in K/km) and wavenumber–2 topographic forcing (h in km) in the one hemisphere only. The winter hemisphere in these perpetual–solstice runs is the same as the hemisphere with topography.

constant summer polar temperature and sinusoidal variation of the winter polar temperature, so that equilibrium temperature in the polar vortex is minimized at winter solstice. The lapse rate is $\gamma = 4$ K/km, and the topography is 4 km high. With a lower stratosphere–troposphere transition, this topographic forcing and lapse rate were found by Sheshadri et al. (2015) to create the most realistic Northern and Southern Hemisphere–like seasonal behavior. The model is run until the age has equilibrated (27 years) and then for another 50 years, which provide the statistics for these results.

For the perpetual–solstice runs, the model is run in a variety of configurations as described in Table 2.1. These four simulations correspond to those highlighted in detail in Figs. 1–3 of Gerber (2012), capturing two cases with an "older" stratosphere and two cases with a "younger" stratosphere. Note however, that Gerber (2012) used a pseudo–spectral model and the age is sensitive to model numerics. All are run to equilibrium, at least 10000 days, and the final 2000 days are averaged for the results presented here.

### 2.3.2 Model seasonality

Panel a) of Figure 2-2 shows a 20 year climatology of the residual vertical velocity at 53 hPa for the seasonally–varying model run. Because of artefacts from the interpolation from the cubed–sphere grid and the high frequency of temporal variability, the field has been smoothed in time and latitude using a binomial filter of two weeks and 10°. Discontinuities are nevertheless visible in midlatitudes in both hemispheres. The seasonal cycle is barely evident; there is stronger polar downwelling in Northern Hemisphere winter/spring and weaker tropical upwelling during Southern Hemisphere winter. Panel b) of Figure 2-2 shows the climatology of the zonal mean diabatic velocity, $\dot{\theta}/\overline{\theta}_z$, on the 500 K surface for the same model run. The 500 K surface is, in the annual mean, near the 53 hPa surface. The diabatic vertical velocity is similar to the residual vertical velocity in the annual mean, but differs at the equinoxes and has a much stronger seasonal cycle in high latitudes. These differences are primarily a result of the motion of the isentropes over the course of the year; in spring, the isentropes descend as the polar region warms, and hence the air moves upward relative to the isentropes. This strong seasonal variability in the diabatic vertical velocity, the relevant vertical velocity for the age difference theory, suggests the importance of the time–derivative terms in (2.26) and (2.30). Panel c) of Figure 2-2 shows the climatology of age on the 500K isentrope for the same run. The ages for this model tend to be older than observed ages, which can be attributed partially to the age being zero at 700 hPa

rather than at the tropopause and partially to the strength of the circulation in the model. Nevertheless, the pattern of age is as expected given the circulation; the air is younger in the tropics and older at the poles, with little variability in the tropics and the oldest air in the vortices in late winter. As in observations (Stiller et al., 2012), the Northern Hemisphere air is generally younger than the Southern Hemisphere air. The seasonal variability in age difference, dominated by variability in polar age of air, is also large compared to the variability in the residual vertical velocity. Meanwhile, the total mass above the isentropic surfaces changes very little over the course of the year.

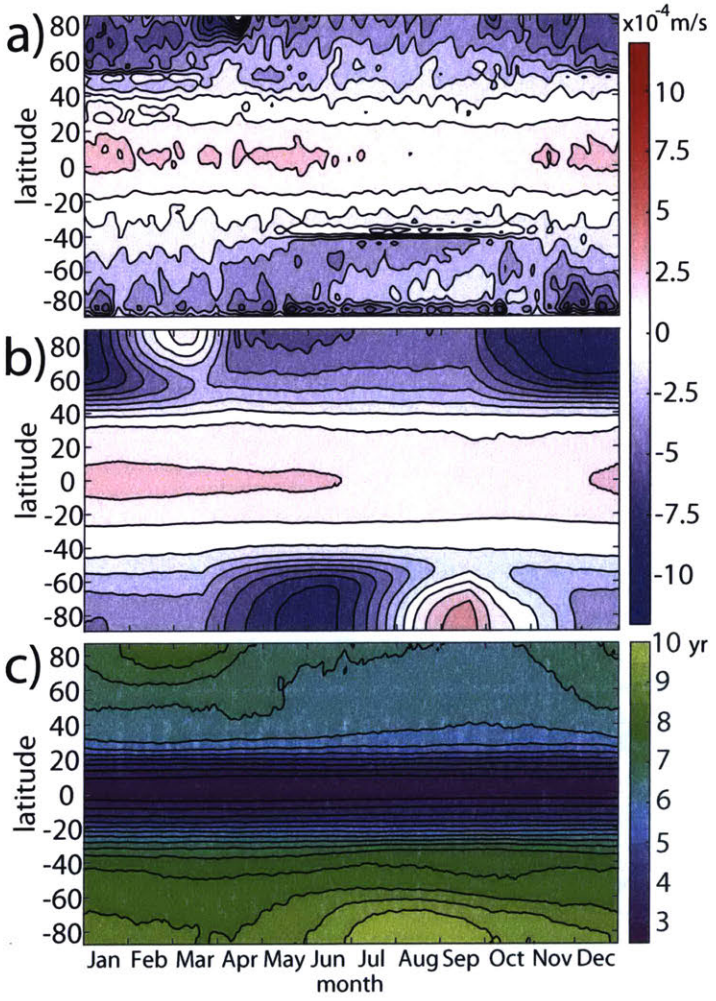


Figure 2-2: Annual cycle based on a 20 year average of the seasonally–varying model run for a) The residual circulation vertical velocity at 53 hPa. The field has been filtered using a binomial filter (14 days in time and 10° in latitude) in order to smooth high temporal variability and cubed–sphere interpolation artifacts. b) The zonal mean diabatic vertical velocity at 500 K divided by the background stratification ($\dot{\theta}/\overline{\theta_z}$). The 500 K isentrope is on the annual average located near the 53 hPa surface. c) The age on the 500 K isentrope. Contour levels are $1.2\times10^{-4}$ m/s and 0.5 years.

### 2.3.3 Time–average results

We examine the time–average theory as described in Section 2.2.2. We calculate the terms in (2.17) for annual averages of 50 years of the seasonally–varying model run and for the average over the last 2000 days of the perpetual–solstice run with the same lapse rate and topography (runs 1 and 3 in Table 2.1). In order to demonstrate the flexibility of the definition of "upwelling" and "downwelling" regions, we have calculated $\left(\Gamma_{\overline{d}} - \Gamma_{\overline{u}}\right)$ and $\overline{M(\theta)}^t / \overline{\mathcal{M}}^t$ for several regions, and these are shown in Figure 2-3. The different "upwelling" regions are defined as follows: the "true" upwelling based on the time–averaged location of positive diabatic vertical velocity (this is not uniform in longitude); between 20°S and 20°N; between 30°S and 30°N; and between 40°S and 40°N. For each case, the "downwelling" region is the rest of the globe. The average age in each region ($\Gamma_{\overline{u}}$ or $\Gamma_{\overline{d}}$) is the mass–flux weighted age through each of these regions as defined in (2.13) and (2.14). Three different levels are shown, and error bars are one standard deviation of the annual averages for the seasonally–varying model run. The maximum overturning mass flux is for the "true" regions, as expected. Because it is most different from the true region, the 20° overturning is the weakest, indicated by the largest age differences. All of the different regions have similar agreement with the theory in both the seasonally–varying model (red and gray points) and in the perpetual–solstice model (blue and teal points). Although the flexibility of the theory is clear from this plot, the 20° tropics does not capture all the upwelling in the model, as can be seen in panel b) of Figure 2-2. Most of the upwelling occurs in the narrow band between 20° S and 20° N, but the 20° overturning is substantially different from the "true" overturning because the weaker upwelling between 20–40° is of older air, and so the age difference neglecting that upwelling is greater than for the "true" regions. Thus although this method can determine the overturning through two regions, to determine the overturning mass flux through the stratosphere, the "true" regions must be used. The agreement of the 40° tropics with the "true" regions is a reflection that on average the "true" regions are bounded by 40° in this simple model. The age difference is largest at 600 K for all of these model runs, which demonstrates a minimum in the relative strength of the overturning circulation. Because the perpetual solstice version of the model has no weakening and reversing of the circulation associated with the seasonal cycle, the annual mean overturning mass flux through an isentrope is greater than in the seasonally-varying model, and so the age difference is smaller.

All of the points fall above the one–to–one line, a discrepancy consistent with the neglect of diabatic diffusion in the theory as will be discussed in Section 2.3.6. The points on the 800 K isentrope are closest to the theory line, which is also consistent with diabatic diffusion. The results from the seasonally–varying model agree as well with the theory as do the results from the perpetual–solstice run, demonstrating the success of the time–average theory in recovering the steady result.

### 2.3.4 Time–varying results

Next we move on to the time–varying theory; consider Figure 2-4. Panel a) shows three years of the the age difference and panel b) shows the total mass divided by the mass flux for the same three years of the seasonally–varying model run. If the steady–state theory held instantaneously, these would be equal at all times. They are obviously not equal; in fact, their seasonal cycles are out of phase, with even negative values of age difference when there is polar diabatic upwelling of very old air associated with the final warming event each

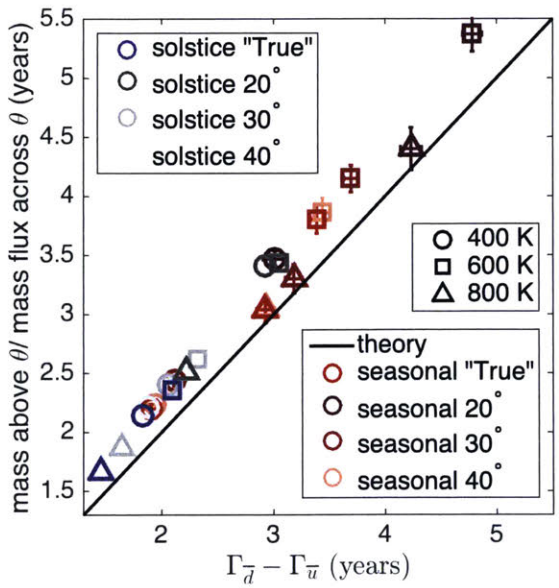


Figure 2-3: The ratio of mass above an isentrope to mass flux through an isentrope versus the difference between age of air in different regions on the isentrope. The red and red-toned points are based on the seasonally–varying model. The blue and gray points are based on the perpetual–solstice model run with $\gamma = 4$ K/km and 4 km topography. The "true" points, in red and blue, are calculated using the time average "true" upwelling and downwelling regions. The gray and red toned points are calculated with the "upwelling" region as the band between 20°S and 20°N, 30°S and 30°N, and 40°S and 40°N, and the "downwelling" region defined as the rest of the globe. The darker points correspond to narrower tropics for both the seasonally–varying and perpetual–solstice runs. Error bars are one standard deviation of the annual averages. The black line is the one–to–one relationship predicted by the theory, and the different symbols are different isentropic levels.

Southern Hemisphere spring.

We evaluate the time–derivative terms in (2.26), $(M\Gamma_s)_t$ and $(\Gamma_u + \Gamma_d)\, M_t/2$. To calculate $(M\Gamma_s)_t$, the mass–weighted average age above each pressure surface is calculated and then interpolated to the isentropes—the integration is performed in pressure coordinates for improved accuracy. The product of the age and the total mass has substantial high–frequency variability. If the model were not run to steady state, long–term changes in the average age of air in the stratosphere would also appear in this term. For example, a relatively dramatic mean age change of 0.5 yr/decade would make this term about 5% of the size of the total mass above the isentrope. The other term, $(\Gamma_u + \Gamma_d)\, M_t/2$, has much less short–term variability.

The average seasonal cycle over twenty years of the model run for each of the terms in (2.26) is shown for three different levels in Figure 2-5. At 400 K, shown in panel a), in the very low stratosphere, there is very little effect of the seasonal cycle. The product of the overturning strength and the age difference, $\mathcal{M}\Delta\Gamma$, is at all times less than the total mass, $M$. This discrepancy will be addressed in Section 2.3.6. The time–derivative terms

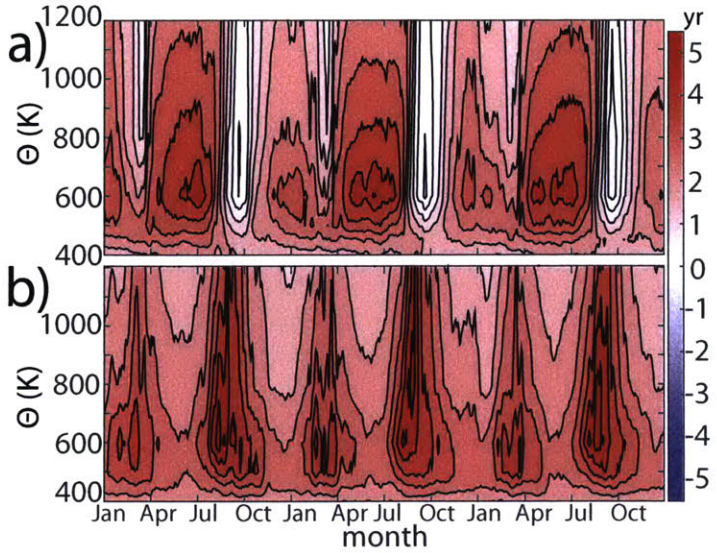


Figure 2-4: Three years of a) the age difference ($\Delta\Gamma$) and b) the ratio of total mass above the isentrope to overturning mass flux through the isentrope ($M(\theta)/\mathcal{M}$) calculated daily for the seasonally–varying model run. Contour levels are 0.5 years.

are small. At 600 K, shown in panel b), the seasonal cycle is much more pronounced, and here the difference between $\mathcal{M}\Delta\Gamma$ and the total mass above the isentrope has a stronger variation in time. The time–derivative terms are approximately the same magnitude, but the variability in $(M\Gamma_s)_t$ is much greater—it has been smoothed with a binomial filter before contributing to the sum. The sum of $\mathcal{M}\Delta\Gamma + (M\Gamma_s)_t + - (\Gamma_u + \Gamma_d)\, M_t/2$ is closer to the total mass above the isentrope $M(\theta)$, and by including the time–dependent terms, the seasonal variation is decreased. Significant discrepancies remain, however. At 800K, shown in panel c), the balance holds even more closely, as the sum is quite close to the total mass for most of the year.

Because of the strong temporal variability, it is clear that the steady–state theory cannot be applied instantaneously. The contributions of the time–derivative terms are smaller upon long–term averaging, however. The magnitude of the annual average of these terms is shown as a percentage of the total mass above each isentrope in the solid lines in Figure 2-7, and the standard deviation is shown in the shading. As we already observed from Figure 2-5, the variability of $(M\Gamma_s)_t$, is much greater than of $(\Gamma_u + \Gamma_d)M_t/2$, up to 10% of $M(\theta)$. The long–term averages of both terms are small. In Figure 2-6, we compare the annual average of $M/\mathcal{M}$ and $\Delta\Gamma$. The mean of 50 years from the seasonally–varying model run are in the red points, with the error bars showing the standard deviation of the annual means. The blue and green points are from the variety of model runs in perpetual–solstice scenarios, as enumerated in Table 2.1. These steady–state runs represent a wide range of climates, with the mass flux across the 600 K surface varying by a factor of about 2. As the total mass above each surface does not change much between the simulations, this results in a factor of 2 in the age difference as well. Examining the blue and green points shows that the theory holds across the whole range of climates simulated here. The annual averages from the seasonally–varying model run result in as good agreement with the steady–state

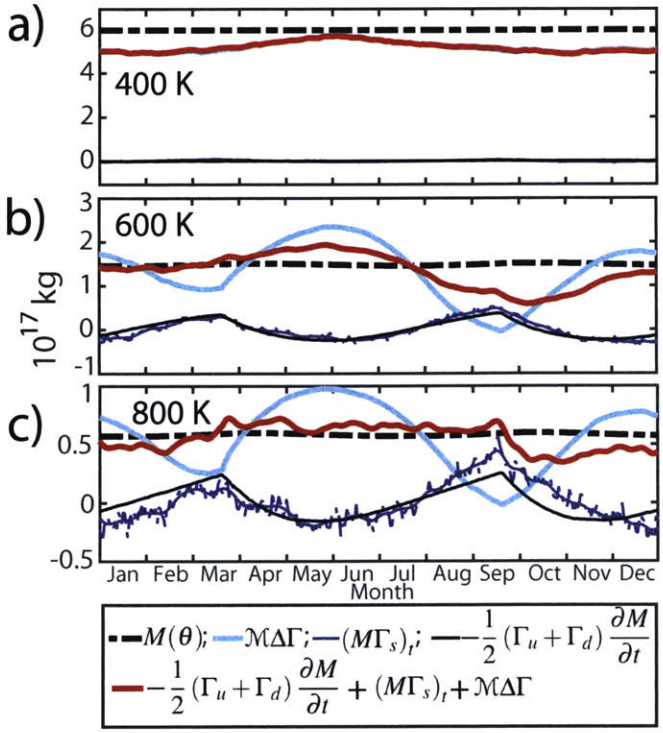


Figure 2-5: 20 years of model output have been averaged at each day of the year to produce a climatological seasonal cycle for the different terms in the age budget: $M(\theta) = \mathcal{M}\Delta\Gamma + (M\Gamma_s)_t + [-(\Gamma_u + \Gamma_d) M_t/2]$. Each panel shows the individual terms and the right hand side at a different level: a) 400 K; b) 600 K; c) 800 K.

theory as the perpetual–solstice model runs, and so we conclude that the annual average overturning strength can be determined by the annual average of the age difference and of the mass above the isentrope.

### 2.3.5 Area weighted averaging

This theory has been developed, by necessity, using mass–flux–weighted age of air. This precludes applying the theory directly to age data, because the circulation is unknown. We therefore try here to determine the bias introduced by using area–weighted age of air rather than mass–flux–weighted age of air. To do this, we define regions of upwelling and downwelling and take the area–weighted average of age in those regions. Because age of air data alone will not inform us as to the upwelling and downwelling regions, we also perform the averaging for the same "upwelling" and "downwelling" regions as for the time–average results (constant latitude bands). The bias introduced by this averaging in the seasonally–varying model is shown at different levels in Figure 2-8, where we show this bias as a fraction of the mass–flux–weighted age difference. The area–weighted age difference is smaller than the mass–flux–weighted age difference in all cases. Using the "true" upwelling and downwelling regions gives a bias of about 10–15%, and the 40° band is similar. When the regions get farther from the "true" upwelling and downwelling, the bias becomes greater.

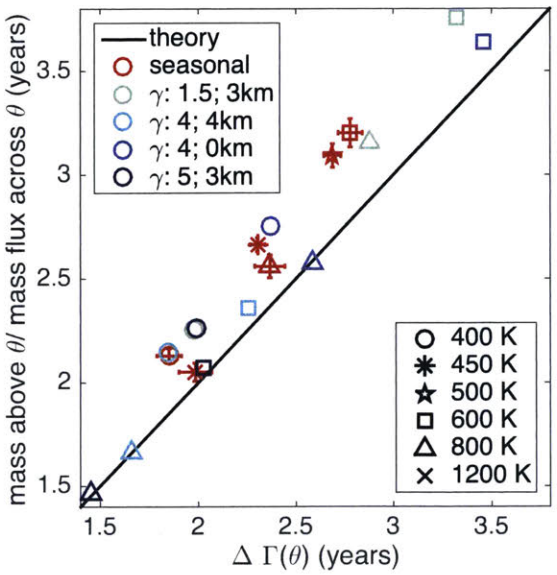


Figure 2-6: The ratio of mass above an isentrope to mass flux through an isentrope versus the difference between downwelling and upwelling age of air on the isentrope. The green and blue points are averages from the last 2000 days of perpetual–solstice runs as described in Table 2.1. The red points are the average of 50 annual averages from the seasonally–varying run with 4000 m topography and lapse rate of 4 K/km. The error bars are one standard deviation of the annual averages. The black line shows the one–to–one relationship predicted by the theory, and the different symbols are different isentropic levels.

In this model, the bias is quite consistent from year to year, as can be seen by the narrow range spanned by one standard deviation from the mean. This investigation demonstrates that we can qualitatively think about the age difference on an isentrope as a proxy for the diabatic circulation through that isentrope.

### 2.3.6 The role of diabatic diffusion

As in Figure 2-3, the points in Figure 2-6 all fall above the one–to–one line, implying that the actual age difference is less than that predicted by the theory by up to about 15%. In the time–average case there is nothing to account for this discrepancy, and in Figure 2-6, the discrepancy is too great to be explained by the time average of the transient terms. Therefore, the discrepancy must arise from terms missing from the theory. Diabatic mixing was neglected at the outset. If we revisit that assumption and include a diffusion of age in (2.4), we obtain

$$\int_\theta \sigma\dot{\theta}\Gamma dA - \int_\theta \sigma K_{\theta\theta}\frac{\partial\Gamma}{\partial\theta}dA = -M, \tag{2.31}$$

or

$$\mathcal{M}\Delta\Gamma + \int_\theta \sigma K_{\theta\theta}\frac{\partial\Gamma}{\partial\theta}dA = M, \tag{2.32}$$

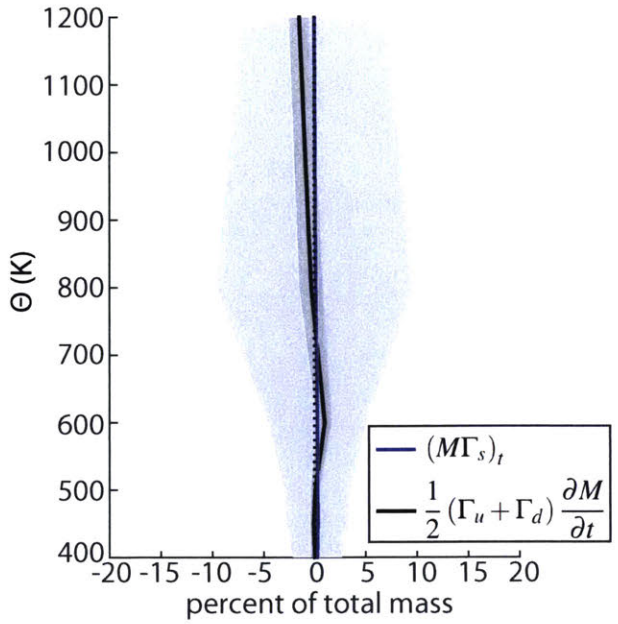


Figure 2-7: The fractional contribution of the annually averaged time–dependent terms in (2.26) as a percentage of the total mass above the isentrope shown in solid lines with the standard deviation of the annual averages in shading. The blue is $(M\Gamma_s)_t/M \times 100\%$, and the black/gray is $(\Gamma_u + \Gamma_d)M_t/2/M \times 100\%$.

where $K_{\theta\theta}$ is the diffusivity. Because of adiabatic mixing in this model, age increases with increasing $\theta$ in all latitudes and altitudes considered here. Since $K_{\theta\theta}$ is positive, the diffusion is a positive term on the left side. In panel a) of Figure 2-5 we noted that the product of the overturning mass flux and the age difference was always less than the total mass above 400K. Now we see that this difference is consistent with the neglect of diffusion. Similarly, the contribution from the diffusive term would account for age differences lower than the theory predicts in both Figures 2-3 and 2-6. To determine whether the diffusivity, $K_{\theta\theta}$, necessary to close the age budget is reasonable, we assume constant diffusivity and find that at 450 K, $K_{\theta\theta} \approx 1.7 \times 10^{-5}\mathrm{K}^2\mathrm{s}^{-1}$. Given the background stratification in the model, this corresponds to about $K_{zz} \simeq 0.1\ \mathrm{m}^2\mathrm{s}^{-1}$, a value that is consistent with observational studies (Sparling et al., 1997; Legras et al., 2003).

In the real world, small–scale diffusion will provide a diabatic component of the age flux, but the model has no representation of such processes and so they cannot be a factor here. However, the large–scale motions are not, as was assumed in the derivation, strictly adiabatic but will exhibit "diabatic dispersion" (Sparling et al., 1997; Plumb, 2007). We can estimate the diffusivity based on Plumb (2007),

$$K_{\theta\theta} \sim |\dot{\theta}'|^2 \tau_{mixing}, \tag{2.33}$$

where $\tau_{mixing}$ is the time scale for isentropic mixing across the surf zone. For the purposes of this estimate, we use the deviation of $\dot{\theta}$ from the zonal mean as an approximation for $\dot{\theta}'$ and use $\tau_{mixing} \approx 30$ days. Using an average value for $|\dot{\theta}'|^2$ in Northern Hemisphere

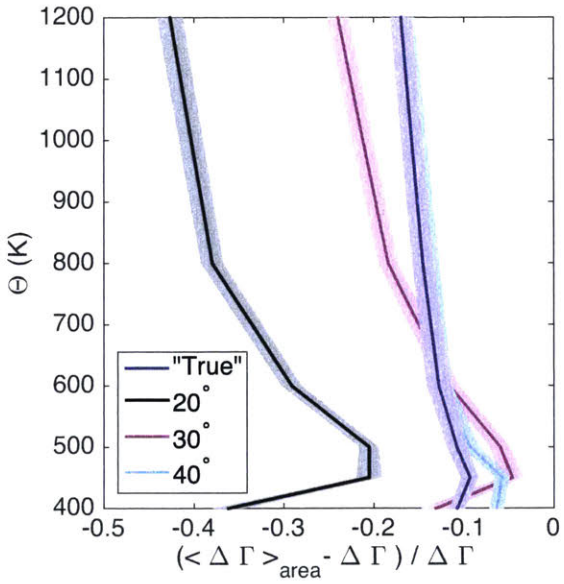


Figure 2-8: The bias introduced by using area–weighted age difference rather than mass–flux–weighted age difference for different regions. The shading shows one standard deviation of the annual average for 50 years of the seasonally varying model run. The overturning regions are defined as in Figure 2-3. The blue shows the "true" region, the black the 20°S–20°N upwelling region, magenta 30 ° and cyan 40°.

midlatitudes at 450 K from the seasonally–varying model run gives $K_{\theta\theta} \approx 1 \times 10^{-5}\mathrm{K}^2\mathrm{s}^{-1}$. The diabatic dispersion is thus close to the diffusivity necessary to close the age budget in this simple model. Now revisiting the observation that the points on the 800 K isentrope seem to have better agreement with the theory line in Figure 2-3, we can understand this as the effect of the reduced cross-isentropic gradient of age higher up in the stratosphere. The same diabatic diffusivity will therefore result in less diffusion of age because of the smaller gradient and the calculated age difference will better match the theory.

## 2.4 Summary and Conclusions

The theoretical developments in this chapter have focused on extension of the simple relationship between the gross latitudinal age gradient on isentropes and the diabatic circulation, obtained by Neu and Plumb (1999) for the "leaky tropical pipe" model. Under their assumptions of steady state and no diabatic mixing, but without any "tropical pipe" construct, an essentially identical result follows. We then show that the result survives intact when applied to time–averages of an unsteady situation, but does not apply locally in time. The predicted age gradient is independent of isentropic mixing, and of the structure of the circulation above the level in question.

Analysis of results from a simplified global model, in both perpetual solstice and fully seasonal configurations, shows that the time-averaged result holds quite well, although the predicted age difference overestimates the actual value by up to 15 percent, a fact that we

ascribe to the neglect of large-scale diabatic mixing in the theory. Indeed, estimates of diabatic dispersion in the model are sufficient to account for the discrepancy.

The theory is, of necessity, formulated in entropy (potential temperature) coordinates and consequently it is the diabatic circulation (rather than, say, the residual circulation) that is related to the latitudinal structure of age. While these two measures of the circulation can, at times (especially around the equinoxes), be very different, in the long-term average to which this theory applies they are essentially identical.

The relationship between age gradient and the circulation is straightforward, but in order to use age data to deduce the circulation there are some subtleties: in order to quantify the mean age difference, in principle one needs to know the geometry of the mean upwelling and downwelling regions, and the spatial structure of the circulation (since, strictly, it is the mass-flux-weighted mean that is required). The theoretical result is unchanged if simpler regions (such as equatorward and poleward of, say, 30°) are used instead of those of upwelling/downwelling, but of course the mass flux involved is that within each chosen region, rather than the total overturning mass flux. When we test the agreement of the theory using an area–weighted age difference using the "true" upwelling and downwelling regions, this introduces a bias of a 10-15% underestimation of the magnitude of the age difference, with a smaller bias lower in the stratosphere. Using 40°S to 40°N as the upwelling region and the rest of the globe as the downwelling region, which is a calculation that is possible entirely from data, we find that the area–weighted age difference has a similar underestimation of the mass–flux–weighted age difference as using the "true" regions. The area–weighted age difference can therefore be used to infer the circulation qualitatively, since the difference is only up to 15%. We caution that this bias estimate was performed with the simple idealized model, and to get a quantitative estimate of the overturning circulation strength from data, a more realistic model is necessary and other factors must be considered.

Despite these caveats, these results offer an avenue for identifying trends in the circulation by seeking trends in age data, as done by Haenel et al. (2015); Ploeger et al. (2015b). For one thing, the theory shows that it is the gross isentropic age difference, and not the age itself, that is related to the strength of the circulation. For another, these results show that annual averages (at least) are necessary to relate the strength of the circulation to the age, and so good data coverage in space and time is necessary to eliminate the seasonal variability for which the theory is not applicable. It will require an accumulation of a long time series of global measurements to separate the long-term trends in the circulation from the short-term variability.

# Chapter 3

# The strength of the meridional overturning circulation of the stratosphere

Much of this chapter is reproduced verbatim from Marianna Linz, R. Alan Plumb, Edwin P. Gerber, Florian J. Haenel, Gabriele P. Stiller, Douglas E. Kinnison, Alison Ming and Jessica L. Neu: The strength of the meridional overturning circulation of the stratosphere, accepted for publication by Nature Geoscience. ML performed the research and wrote the manuscript, under the supervision of AP. EG provided guidance. FH and GS are responsible for the MIPAS age data set. DK ran the WACCM model. AM provided the diabatic heating rates from ERA-I. JN helped with the nitrous oxide data and with the manuscript. I have included some additional discussion that was omitted from the journal article because of space constraints.

## 3.1 Introduction

The Brewer–Dobson circulation, the meridional overturning of mass in the stratosphere, is important for the distribution of gases in the stratosphere, such as ozone and water vapor, which impact surface climate. The distribution of gases such as ozone and water vapour in the stratosphere — which affect surface climate — is influenced by the meridional overturning of mass in the stratosphere, the BrewerâĂŞDobson circulation. However, observation-based estimates of its global strength are difficult to obtain. Here we present two calculations of the mean strength of the meridional overturning of the stratosphere. We analyse satellite data that document the global diabatic circulation between 2007âĂŞ 2011, and compare these to three re-analysis data sets and to simulations with a state-of-the-art chemistry-climate model. Using measurements of sulfur hexafluoride ($SF_6$) and nitrous oxide ($N_2O$), we calculate the global mean diabatic overturning mass flux throughout the stratosphere. In the lower stratosphere, these two estimates agree, and at a potential temperature level of 460 K (about 20 km or 60 hPa in tropics), the global circulation strength is 6.3–7.6 $\times$ $10^9$ kg/s. Higher in the atmosphere, only the $SF_6$-based estimate is available, and it diverges from the re-analysis data and simulations. Interpretation of the $SF_6$ data-based estimate is limited because of a mesospheric sink of $SF_6$; however, the reanalyses also differ substantially from each other. We conclude that the uncertainty in the mean meridional overturning circulation strength at upper levels of the stratosphere amounts to at least 100 %.

Previous calculations of the strength of the stratospheric circulation from data have relied on indirect measures. Observational estimates of the strength of the overturning have been limited to qualitative descriptions based on tracer distributions (e.g. Stiller et al. 2012, Engel et al. 2009, Mahieu et al. 2014, Haenel et al. 2015) or quantitative measures of limited regions, such as the vertical velocity over a narrow range in the tropics (Mote et al. 1996, Schoeberl et al. 2008, Flury et al. 2013). Other metrics are available for stratosphere–troposphere exchange, such as measurements of $^{14}CO_2$ (Kanu et al., 2016). Free-running climate models vary widely in stratospheric circulation metrics, including the tropical upwelling mass flux at 10 hPa and 70 hPa, though the multimodel mean is relatively close to some reanalysis products (Butchart et al., 2011). Reanalyses, meanwhile, differ substantially (about 40% between 10 and 70 hPa and even more lower in the stratosphere) in their mean tropical upwelling velocity, with the magnitude of the mismatch depending on how it is computed (Abalos et al., 2015). They tend to agree for long term trends, showing a weakening of the lowermost stratospheric circulation over the past few decades, and the time period covered by these reanalyses is just about the minimum to assess a long term trend in the stratospheric circulation, based on the time of emergence of a 2%/decade trend (Hardiman et al., 2017). Here we consider the diabatic circulation of the stratosphere; because the stratosphere is stratified, vertical motion moves air across potential temperature surfaces and thus must be associated with warming/cooling in the ascending/descending branches. Hence the net meridional overturning of mass is tightly linked to diabatic processes. We use potential temperature as our vertical coordinate and the meridional overturning becomes explicitly the diabatic circulation in this framework.

In a generalization of the work by Neu and Plumb (1999), Linz et al. (2016) presented a theory to calculate the strength of the diabatic stratospheric circulation through each isentropic surface above the tropical tropopause from the idealized tracer "age of air" (Waugh and Hall, 2002), which is a measure of how long an air parcel has spent in the stratosphere. The difference between the age of the air that is upwelling and downwelling through an

isentropic surface is inversely proportional to the strength of the diabatic circulation through that surface, in steady-state and neglecting diabatic diffusion.

In this paper, we apply the age difference theory to calculate the mean magnitude and vertical structure of the global overturning circulation of the stratosphere based on observations of $SF_6$ and $N_2O$. We demonstrate the validity of the theory and explore limitations of the tracer data with a coupled chemistry-climate model. We calculate the global overturning directly from the diabatic vertical velocity from three reanalyses to compare with the data and model results. Information on the data products, model, and reanalyses is given in Table 3.1.

## 3.2 Age of air observations and model

A trace gas that is linearly increasing in time in the troposphere and has no stratospheric sinks can be converted to age following the theory presented in Waugh and Hall (2002), and these are known as "clock" tracers. Carbon dioxide ($CO_2$) and $SF_6$ are both approximately linearly increasing in the troposphere and have minimal sinks in the stratosphere. $CO_2$ has a strong seasonal cycle in the troposphere, which makes the calculation of age more difficult in the lowermost stratosphere, while $SF_6$ has a mesospheric sink that complicates its interpretation in the uppermost stratosphere. Together these two clock tracers provide useful complementary information to constrain the true age of air. We use age derived from $SF_6$ measurements (henceforth $SF_6$-age) from the Michelson Interferometer for Passive Atmospheric Sounding (MIPAS) on Envisat (Haenel et al., 2015). $CO_2$ is currently not retrieved from satellites with enough accuracy and spatial coverage to calculate age of air differences (Carlotti et al., 2016). We interpolate $SF_6$-age onto isentropic surfaces using simultaneously retrieved pressure and temperature from MIPAS (von Clarmann et al., 2003, 2009). The resulting $SF_6$-age on the 500 K surface is shown in Figure 3-1a. Age is young in the tropics, older in the extratropics, and oldest at the winter poles, consistent with the pattern of upwelling in the tropics and the majority of downwelling in the winter polar region. The $SF_6$-age at high latitudes in wintertime is older than observations of age based on $CO_2$ measurements (Plumb et al., 2002). Because $SF_6$ is not conserved in the mesosphere, areas with mesospheric influence, such as the poles and the upper stratosphere, will have a high bias in $SF_6$-age (Hall and Waugh, 1998).

To explore the limitations of using $SF_6$-age, we compare $SF_6$-age to ideal age of air in a coupled chemistry-climate model, the Community Earth System Model 1 Whole Atmosphere Community Climate Model (WACCM). This fully coupled state-of-the-art interactive chemistry climate model (Marsh et al., 2013; Garcia et al., 2017) includes the physical parameterizations and finite-volume dynamical core (Lin, 2004) from the Community Atmosphere Model, version 4 (Neale et al., 2013). The model domain extends from the Earth's surface to the lower thermosphere (140 km). The WACCM simulations are based on the Chemistry Climate Model Initiative REF-C1 scenario (Morgenstern et al., 2017). WACCM models only one of the two sinks of $SF_6$ in the mesosphere; photolysis at Lyman-alpha wavelengths is included, but associative electron attachment, recently shown to be the dominant loss mechanism for $SF_6$ below 105 km (Totterdill et al., 2015; Kovács et al., 2017), is not. The impact of the mesospheric sink of $SF_6$ on stratospheric $SF_6$ will be determined by the strength of the dynamical coupling between the stratosphere and the mesosphere. We calculate $SF_6$-age following the methods of Stiller et al. (2012) to compare with the MIPAS $SF_6$-age, and for details see the Methods section. Although WACCM is missing the dominant $SF_6$ loss mech-

| Data source | Variables | Resolution | Time period | Reference |
|---|---|---|---|---|
| MIPAS | age from $SF_6$; temperature; pressure | zonal mean, 10° lat, 41 levels from 8 km to 54 km | 2002–2012 | Haenel et al. 2015 |
| GOZ-CARDS | $N_2O$ | zonal mean, 10° lat, 15 pressure levels from 100 to 0.46 hPa | 2004–2014 | Froidevaux et al. 2015, Andrews et al. 2001, Strahan et al. 2011 |
| EPA Climate Indicators | tropospheric $N_2O$ | *in situ* surface | 1980–2014 | US EPA 2016 |
| WACCM | SW; LW; temperature; ideal age; $SF_6$ | 2.5 ° lon, 1.875 ° lat, 31 pressure levels from 193 hPa to 0.3 hPa | 1979–2014 | Marsh et al., 2013, Garcia et al. 2017 |
| JRA 55 | SW; LW; temperature | 1.25°×1.25°, 16 pressure levels from 225 hPa to 1 hPa | 1979–2014 | Kobayashi et al. 2015 |
| MERRA | total dT/dt; temperature | 1.25°×1.25°, 17 pressure levels from 200 hPa to 0.5 hPa | 1979–2014 | Rienecker et al. 2011 |
| ERA-Interim | SW; LW; temperature | 1°×1°, 26 pressure levels from 150 hPa to 0.5 hPa | 1979–2014 | Dee et al. 2011 |

Table 3.1: Data, reanalyses, and model output used in this study. SW is the shortwave radiation and LW is the longwave radiation.

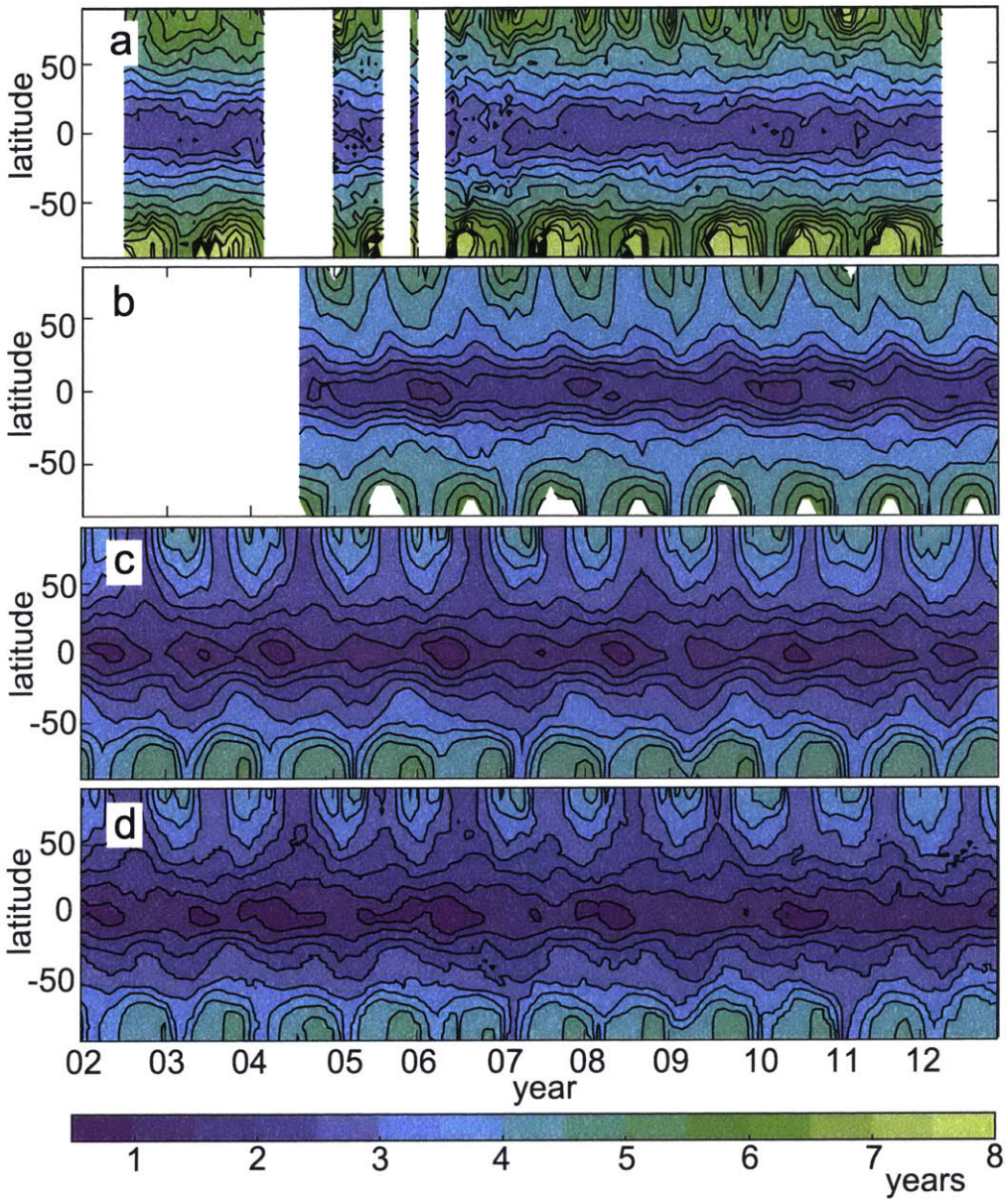


Figure 3-1: Age of air on the 500 K surface. (a) $SF_6$ from MIPAS, (b) $N_2O$ from GOZCARDS, Andrews et al. 2001 (c) $SF_6$ from WACCM, and (d) WACCM ideal age tracer. Contours are every half year, and the ages in the Southern Hemisphere winter for MIPAS get above 8 years old.

anism, the difference between $SF_6$-age and ideal age will qualitatively illustrate the sense and location of any bias introduced by using $SF_6$ as an age tracer.

Age on the 500 K surface between 2002 and 2012 is shown for WACCM $SF_6$-age in Figure 3-1c, and for WACCM ideal age of air in Figure 3-1d. Note that both of these are much

younger than the MIPAS $SF_6$-age, especially at the poles. WACCM age is at most 4 years in the Northern Hemisphere winter at the pole, where the age derived from the $N_2O$ data suggests up to 5 years and the ages from MIPAS $SF_6$ show ages up to 8 years. Ideal age is very similar to $SF_6$-age in the tropics, though there are deviations in the winter poles. The close agreement between ideal age and $SF_6$-age on the 500 K surface suggests that $SF_6$-age might be a good proxy for ideal age for most latitudes on this level. The temporal correlation at each latitude on the 500 K surface is high ($r = 0.93$), and only at the poles is $SF_6$-age older than ideal age by up to half a year. The zonal mean mean correlation coefficient between the time series of $SF_6$-age and ideal age at every latitude and height between ideal age and $SF_6$-age is shown in Figure 3-2a and the slope of that correlation is shown in Figure 3-2b. The correlation is calculated using reduced major axis regression on the detrended time series, with the mean climatology removed. Where there is more mesospheric influence, the correlation is weaker and no longer one-to-one: higher in the stratosphere and at the highest latitudes ($r = 0.52$ and age has only 35% of the magnitude of variations of $SF_6$-age at 1200 K at 85° N). The weakest correlation is at the Southern Hemisphere vortex edge and the center of the Northern Hemisphere vortex at upper levels. The correlation is also weak near the tropopause in the tropics because of how the reference $SF_6$ time series is defined; the location from which the reference time series is drawn impacts this correlation at these low levels, which have values of $SF_6$ similar to those of the reference time series, but does not impact the overall structure of the correlation higher up where we are investigating the impact of the mesospheric sink. The slope of the correlation is less than one for most regions, so $SF_6$-age is more variable than ideal age. In the Southern Hemisphere polar region, as far down as 700 K, the $SF_6$-age is more than twice as variable than the ideal age. Because of the dramatic difference between the tropics and the poles, using $SF_6$-age instead of ideal age will definitely introduce a bias in the age difference between the upwelling and downwelling regions. The correlation is dominated by the seasonal cycle; when the seasonal cycle is removed (not shown), the correlation between $SF_6$-age and ideal age becomes almost negligible throughout the domain, except in certain regions where their temporal evolution is anticorrelated. Since WACCM is missing the dominant sink of $SF_6$, the differences shown here represent a lower bound on the bias from using $SF_6$-age as a proxy for ideal age.

The difference between the MIPAS $SF_6$-age and WACCM $SF_6$-age is substantial. MIPAS $SF_6$-age has been shown to be consistently older than in situ $CO_2$ and $SF_6$-age observations, though typically within error estimates (Stiller et al. 2012; Haenel et al. 2015, see also Supplementary Information). These known biases of 0.5-1.5 years are almost enough to explain the difference between WACCM $SF_6$-age and MIPAS $SF_6$-age in the tropics. In the polar region, a similar amount of bias exists at low levels, and at upper levels there are no in situ measurements for comparison. In WACCM, the dynamical coupling of the stratosphere and mesosphere has been shown in certain events to be too weak (Funke et al., 2011, 2017) and in another case to be accurate (Ray et al., 2017), and so the reliability of the model's transport of mesospheric air into the stratosphere is unclear.

Given the potential biases of $SF_6$-age and the MIPAS data, other age tracers are desirable to corroborate the circulation strength calculations from $SF_6$-age. Since, $CO_2$ is not available, we determine age from $N_2O$, which demonstrates a compact relationship with age, like other long-lived stratospheric tracers (Plumb and Ko, 1992). We use the relationship between age of air and $N_2O$ calculated empirically by Andrews et al. (2001), accounting for the linear growth in tropospheric $N_2O$. Following the procedure outlined in the Methods, we calculate age of air from the Global OZone Chemistry And Related trace gas Data records for the Stratosphere (GOZCARDS) $N_2O$ data for 2004–2013 (Froidevaux et al., 2013). Because

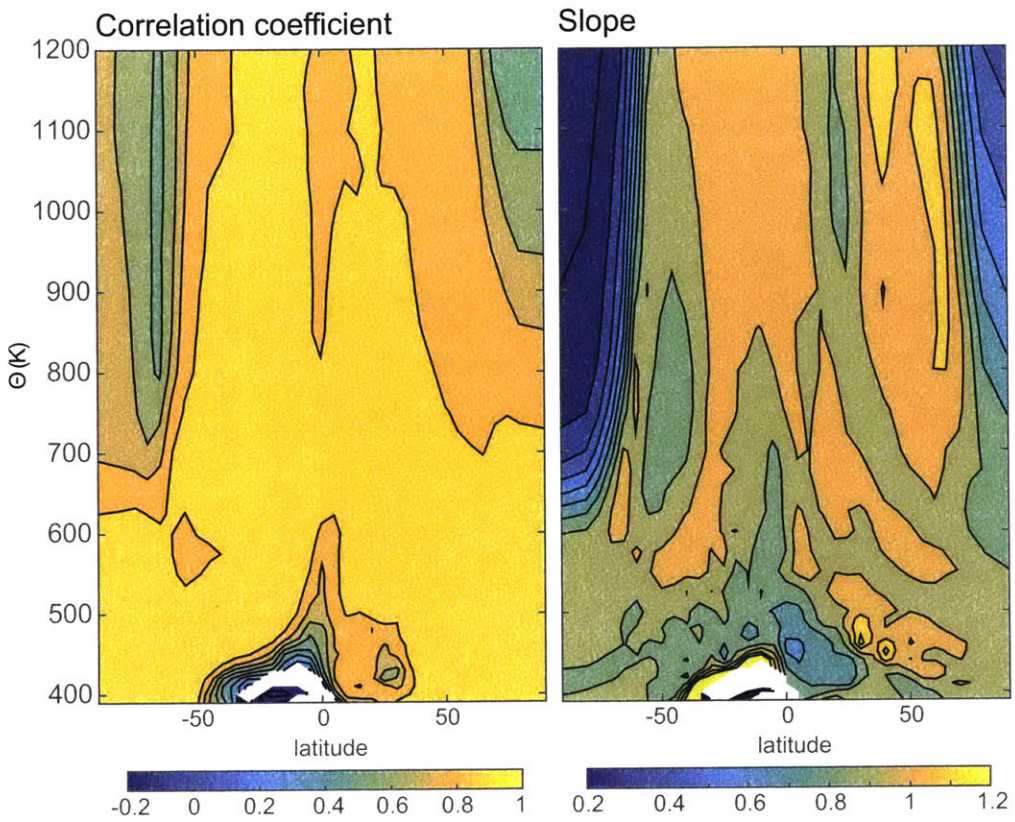


Figure 3-2: The zonal mean (a) correlation coefficient and (b) slope of correlation for the correlation between the time series of $SF_6$-age and ideal age at every grid point for WACCM from 1990–2014.

of the range of tracer values over which the empirical relationship holds, global coverage exists for a small range in potential temperature (about 450 K–500 K). Another empirical relationship between $N_2O$ and age was calculated more recently by Strahan et al. (2011), who found an approximately linear relationship between age and $N_2O$ based on balloon and satellite measurements of $CO_2$ and $SF_6$. This is discussed extensively in the Supplementary Information.

The age on the 500 K surface calculated from the empirical relationship of age with $N_2O$ from Andrews et al. (2001) is shown in Figure 3-1b. The Southern Hemisphere winter polar coverage is poor on this level because values of $N_2O$ are below 50 ppbv, the lower limit of the empirical fit. Age from the $N_2O$ data is generally younger than MIPAS $SF_6$-age, though somewhat older than ages from WACCM. The temporal correlation of MIPAS $SF_6$-age and $N_2O$-age at every latitude on the 500 K surface is around $r = 0.5$, except in the Northern Hemisphere midlatitudes, where the correlation is not significant.

## 3.3 Age difference and the diabatic circulation

Chapter 2 showed that, in steady state, the diabatic circulation ($\mathcal{M}$) through an isentropic surface wholly within the stratosphere can be calculated as the ratio of the mass above the surface ($M$) to the difference in the mass-flux-weighted age of downwelling and upwelling air on the surface ($\Delta\Gamma$, or age difference).

$$\mathcal{M} = M/\Delta\Gamma. \tag{3.1}$$

$\mathcal{M}$ is the total mass flux that is upwelling (or downwelling, as in steady-state these must be equal) through the isentropic surface. (See Figure 5-1 for a diagram.) Intuitively this reflects the idea of a residence time; the age difference is how long the air spent above the surface, and it is equal to the ratio of the mass above the surface to the mass flux passing through that surface.

The real world is not in steady-state, and so averaging is necessary for this theory to apply. In Chapter 2, I found that a minimum of one year of averaging was necessary for the theory to hold in an idealized model. As the MIPAS instrument has five years of continuous data, the longest average possible for this study is five years. To test the validity of applying this steady-state theory to five-year averages of age difference, we have calculated the 2007–2011 averages of ideal age difference and the ratio of the total mass above each isentrope to the mass flux through that isentrope from WACCM output. These are shown in the blue lines (solid and dotted respectively) in Figure 3-3. The total overturning strength is calculated from the potential temperature tendency, $\dot{\theta}$, which is the total all sky radiative heating rate interpolated onto isentropic surfaces. The upwelling and downwelling regions are defined where $\dot{\theta}$ is instantaneously positive or negative, and the mass fluxes through these regions are averaged to obtain the total overturning mass flux, $\mathcal{M}$. If the age difference theory held exactly, the two blue lines in Figure 3-3 would be identical. In the upper stratosphere, these two calculations agree closely; in the lower stratosphere, the ratio of the mass to the mass flux is greater than the ideal age $\Delta\Gamma$. This behavior is consistent with the neglect of diabatic diffusion, which is greater in the lower stratosphere (Sparling et al., 1997). Using area weighting of ideal age, since mass-flux weighting is not possible with data, results in about a 10% low bias of $\Delta\Gamma$ compared to the mass-flux weighting shown here.

We calculate the five year average (2007–2011) of the difference in area-weighted age of air in the regions poleward and equatorward of 35° from the $SF_6$-age from both MIPAS and WACCM, and from the $N_2O$-age. (See Supplementary Information for a discussion of this latitudinal extent.) The results of this are shown in Figure 3-3. The MIPAS $SF_6$-age $\Delta\Gamma$ is notably different from the other estimates except around 450 K. At 400 K, it is much smaller, in part because of older tropical air at that level (see Supplementary Information). Starting around 500 K, MIPAS $SF_6$ $\Delta\Gamma$ is much greater than the model $\Delta\Gamma$ using either ideal age or $SF_6$-age. Age difference for $N_2O$ is calculated only where there is data available over the entire surface at almost all times, 450–480 K. In this limited range, the age difference from $N_2O$-age is somewhat greater than the age difference from WACCM and agrees with the age difference calculated from MIPAS $SF_6$-age.

To gain insight into the role of the mesospheric sink, we compare the ideal age $\Delta\Gamma$ with $SF_6$-age $\Delta\Gamma$ in WACCM. The ideal age $\Delta\Gamma$ is the mass-flux-weighted age difference between upwelling and downwelling regions, and the $SF_6$-age $\Delta\Gamma$ from WACCM is calculated in the same way as the MIPAS $SF_6$-age $\Delta\Gamma$. Because of the area-weighting, we expect the $SF_6$-age $\Delta\Gamma$ to be 10% lower than the ideal age $\Delta\Gamma$. This is true from 450–550 K, but above that, the

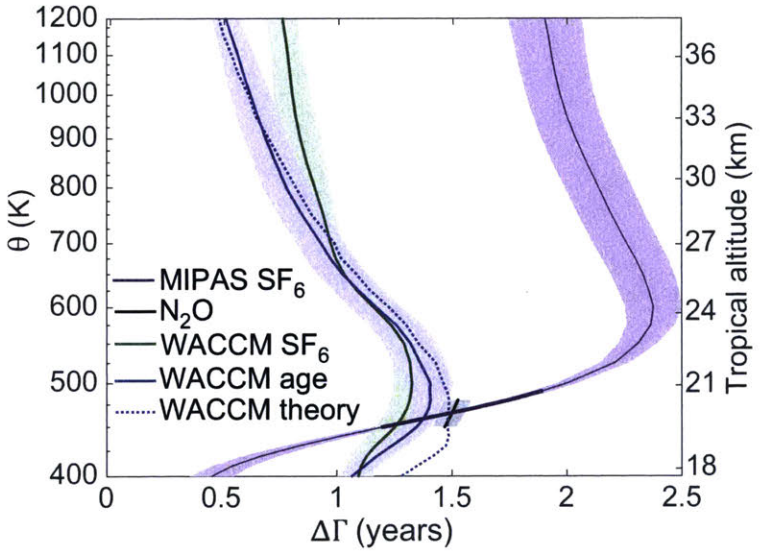


Figure 3-3: The average age difference between downwelling and upwelling age of air on each isentrope between 2007–2011. $\Delta\Gamma$ is plotted in solid lines: MIPAS $SF_6$-age in purple, GOZCARDS $N_2O$ age in black, WACCM $SF_6$-age in green, and WACCM ideal age of air in the blue. The blue dotted line shows the ratio of the total mass above each isentrope to the mass flux through the isentrope ($M/\mathcal{M}$) from WACCM. The shading shows one standard deviation of the five annual averages that are averaged to get the mean. The mean height of each isentrope in the tropics (calculated from MIPAS pressure and temperature) is on the right y-axis. Where the line for the MIPAS $SF_6$ calculation is thick, there is confidence in both the data and in its conversion to age. Where it is thin, there are reasons to believe bias in either the data or in the conversion that lend less credence to its age difference.

$SF_6$-age $\Delta\Gamma$ is either equal to or greater than the ideal age $\Delta\Gamma$, and at 1200 K $SF_6$-age $\Delta\Gamma$ is 50% greater. Since WACCM does not include the dominant sink of $SF_6$ for the mesosphere, the bias is certainly greater, and we cannot estimate an upper bound.

All three calculations of $\Delta\Gamma$ from the model as well as the $\Delta\Gamma$ from MIPAS $SF_6$-age show a peak somewhere in the middle stratosphere. This peak indicates a relative minimum of the diabatic velocity at that level, and so this provides evidence that there are indeed two branches of the circulation (Birner and Bönisch, 2011) and is a straightforward diagnostic for the separation level.

Although the focus of this chapter is on the mean strength of the circulation, much recent interest has been focused on the trends in the circulation strength. We therefore use WACCM to explore whether the age difference calculated using $SF_6$-age can be a reliable measure of circulation changes over a timescale of a decade. Figure 3-4 shows the time series of the age difference on the 500 K surface and on the 1200 K surface using mass-flux-weighted ideal age averaged over the true upwelling and downwelling regions and also using $SF_6$-age averaged between 35°S-35°N as the upwelling region and the region poleward of 35° as the downwelling region. At 500 K, the two time series appear to be highly correlated, with the ideal age $\Delta\Gamma$ showing a bit more variability than the $SF_6$-age $\Delta\Gamma$. At 1200 K, the two time

series are no longer as obviously correlated. Moreover, and more troublingly, the $SF_6$-age shows a statistically significant positive trend in age difference, while the ideal age does not. Over this same time period, there is no statistically significant trend in the diabatic circulation at that level. Thus, trends in $SF_6$-age $\Delta\Gamma$ may be unrelated to the trends in the diabatic circulation at upper levels. We hypothesize the trend in $SF_6$-age at upper levels is due to changes in the degree of coupling with the mesosphere, but have not yet confirmed this with examination of mesospheric tracers in the model.

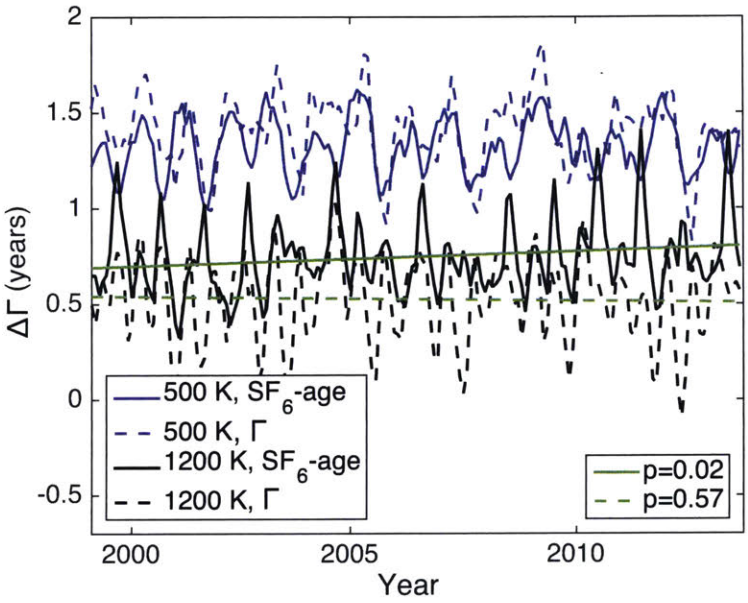


Figure 3-4: Time series of $\Delta\Gamma$ calculated using ideal age and $SF_6$-age from WACCM starting in 1999 for two different levels. The blue lines are the age difference on the 500 K surface and the black lines are the age difference on the 1200 K surface. The dashed lines are the ideal age $\Delta\Gamma$, averaged over the true upwelling and downwelling regions. The solid lines are the $SF_6$-age $\Delta\Gamma$ area weighted over the tropics and extratropics, with the dividing latitude at 35°. The bright green lines are the trends calculated for the 1200 K $\Delta\Gamma$, with the solid green line showing the trend for the $SF_6$-age $\Delta\Gamma$ and the dashed line showing the trend for the ideal age $\Delta\Gamma$, and their p values are reported in the bottom right legend.

## 3.4 Circulation from Reanalyses, Model, and Age

Figure 3-5 shows the total overturning circulation strength calculated using the ratio of the total mass above the isentrope to $\Delta\Gamma$ for the MIPAS $SF_6$-age and the $N_2O$-age. Total mass is determined from the simultaneously retrieved pressure in the former case and from pressure from the Modern Era Retrospective analysis for Research and Applications (MERRA, Rienecker et al. 2011) for $N_2O$. Also shown is the directly calculated overturning circulation strength from the three reanalysis products MERRA, Japanese 55-year Reanalysis (JRA 55, Kobayashi et al. 2015) and the ECMWF Reanalysis Interim (ERA-Interim,

Dee et al. 2011), and from WACCM. The total overturning strength is calculated from the potential temperature tendency, $\dot{\theta}$, from the total diabatic heating rates from JRA 55 and ERA-Interim forecast products and from total temperature tendency provided by MERRA, and then following the same procedure as above for WACCM.

These six estimates of the strength of the circulation are quite different, as can be seen clearly by examining the circulation at individual levels. At the lowermost levels, the reanalyses tend to agree, while the MIPAS $SF_6$-age circulation estimate is much greater because of its very low $\Delta\Gamma$. In the range where we have estimates from both observational data sets, they agree closely and are flanked by the reanalyses, which vary more widely (see Supplementary Information for more details). At 500 K and above, the MIPAS $SF_6$-age based circulation strength has the lowest value, and at 900 K and above, it is lower by a factor of three. The circulation strength from MIPAS $SF_6$-age $\Delta\Gamma$ is biased low consistent with the sink of $SF_6$ in the mesosphere (Kovács et al., 2017). The disagreement at 1200 K would require that the bias be nearly 300% for the model and reanalyses to be consistent. In addition to the disagreement of MIPAS $SF_6$-age circulation strength with the model and reanalyses, there is significant disagreement between different reanalyses. MERRA has a distinct vertical structure, with weaker circulation in the lower stratosphere and stronger circulation in the mid-stratosphere. JRA 55 and ERA Interim have a similar vertical structure; JRA 55 is stronger by around $3\times10^9$ kg $s^{-1}$, except above 800 K, where it decreases much more quickly with height than ERA-Interim so that they converge by 1200 K. The shading is the standard deviation of the annual averages that make up the five year average, and it shows the interannual variability, which is generally small.

## 3.5 Conclusions

The strength of the stratospheric circulation helps determine transport of stratospheric ozone, stratosphere-troposphere exchange, and the transport of water vapor into the stratosphere (Butchart, 2014). Stratospheric water vapor has been demonstrated using both data (Solomon et al., 2010) and a model (Dessler et al., 2013) to impact the tropospheric climate. The stratospheric ozone hole recovery is also influenced by the strength of the circulation (Solomon et al., 2016).

We have calculated the strength of the overturning circulation of the stratosphere from observations, reanalyses, and a model. We find that at 460 K (about 60 hPa or 20 km in the tropics), the total overturning circulation of the stratosphere is 7.3 $\pm$0.3 $\times10^9$ kg/s based on the agreement of two independent global satellite data products to within 4%. More details on these two different age products is in the Supplementary Information. Given the possibility that area weighting has created a high bias of up to 10%, any model or reanalysis product between 6.3–7.6 $\times10^9$ kg/s could be considered to agree with the observations at this level. Despite this wide range, two of the three state-of-the-art reanalysis products lie outside of this range, suggesting deficiencies in their lower stratospheric transport (see Supplementary Information). This can be used as a metric to determine the accuracy of the mean transport of climate models. Because the diabatic circulation and not the residual circulation is used in this case, the computational demands for this metric are minimal, requiring only monthly mean total diabatic heating and temperature on pressure levels.

The global $SF_6$ data have enabled this first quantitative calculation of the diabatic circulation in the middle and upper stratosphere. However, the interpretation of age from $SF_6$ is limited because we cannot quantify the impact of the mesospheric sink of $SF_6$, which

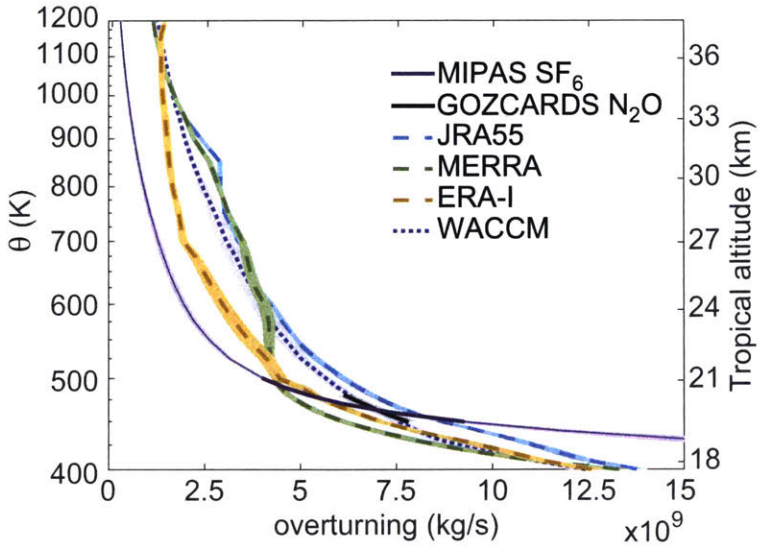


Figure 3-5: The strength of the total overturning circulation through each isentrope averaged between 2007–2011. The solid lines are for the data-based estimates MIPAS $SF_6$ is in purple and GOZCARDS $N_2O$ in black. Reanalyses are shown in dashed lines: JRA 55 in light blue, MERRA in green and ERA-Interim in gold. The dotted blue line is WACCM. The shading shows one standard deviation of the five annual averages. The details of the calculation for each data product, the model, and the reanalyses are described in the text. The mean height of each isentrope in the tropics (calculated from MIPAS pressure and temperature) is on the right y-axis.

we find to be important above 500 K. We estimate that this makes the age difference a minimum of 60% too high at 1200 K, which would imply a 35% low bias in the overturning strength at 1200 K, and we cannot estimate an upper bound on the bias. The reanalyses may correctly represent the true stratospheric circulation where they agree at the uppermost levels, although at those levels the data becomes more limited (e.g. Dee and Uppala 2009). Beneath 900 K, however, the reanalyses disagree with each other as well as with the circulation strength implied by the data; it is clear that the data assimilated into these reanalyses are not sufficient to constrain estimates of the circulation.

Climate models predict an increase in the strength of the Brewer–Dobson circulation of about 2% per decade (Butchart et al. 2006, Hardiman et al. 2014), and much effort has recently gone towards calculating trends in the stratospheric circulation based on observations and reanalyses to see if such a trend can be detected (Engel et al. 2009, Seviour et al. 2012, Diallo et al. 2012, Abalos et al. 2015). However, the mean diabatic circulation strength is not known except at one level. At upper levels, the circulation is uncertain to within at least 100%. We suggest cautious interpretation of trends that are much smaller than that uncertainty. More global age of air tracer data, in particular $CO_2$, is necessary to provide an independent estimate of age difference necessary to calculate the strength of the diabatic stratospheric circulation. High altitude balloon and aircraft measurements at high and low latitudes could be very useful; further characterization of compact relationships between age

and long-lived tracers, such as $N_2O$ or methane, would provide additional constraints on the circulation in the lower stratosphere, enabling more complete utilization of current global satellite data.

## Methods

**MIPAS $SF_6$** For more details on validation and methods, we refer the readers to the papers on this product (Stiller et al., 2008, 2012; Haenel et al., 2015). We note that the vertical resolution is 4 to 6 km at 20 km, 7 to 10 km at 30 km, and 12 to 18 km at 40 km altitude. Noise error on individual profiles is of the order 20%, but because of the many profiles, meaningful $SF_6$ has been obtained by using monthly and zonal mean averages in 10 degree bins.

**$N_2O$** Andrews et al. (2001) calculate an empirical fit between $N_2O$ and age from an extensive record of NASA ER-2 aircraft flights and high-altitude balloons from 1992–1998. Age is based on $CO_2$, and for details of the conversion from $CO_2$ to age, see Andrews et al. (2001). The fit holds well for 50 ppbv $< N_2O <$ 300 ppbv and is given by the equation $\Gamma(N_2O) = 0.0581(313 - N_2O) - 0.000254(313 - N_2O)^2 + 4.41 \times 10^{-7}(313 - N_2O)^3$, where 313 ppbv was the average tropospheric mixing ratio for 1992–1998. Although different tracer-tracer relationships are expected in the tropics and the extratropics (e.g. Strahan et al., 2011, Plumb, 2007), the limited tropical data used to calculate this relationship were not treated separately. In order to account for the increase in tropospheric $N_2O$, we calculate the trend from the data product provided by the EPA Climate Indicators (US Environmental Protection Agency, 2016), a combination of station measurements from Cape Grim, Australia, Mauna Loa, Hawaii, the South Pole, and Barrow, Alaska. The slope is 0.806±0.014 ppbv/yr. (One standard error on the slope is reported. Using only Mauna Loa, the tropical station, does not change the fit much, since $N_2O$ is quite well mixed in the troposphere.) We linearly adjust the GOZCARDS $N_2O$ data using this slope to account for the growth in tropospheric $N_2O$, although simply subtracting the mean difference in tropospheric $N_2O$ between 2009 and 1995 yielded very similar results. Then we apply the empirical relationship between 2004 and 2012 to obtain age estimates. Age difference is calculated only on those levels for which there are very few gaps in age. Only 460 and 470 K have no gaps at all. This method relies on several potentially problematic assumptions: the compact relationship from the 1990s is assumed to be applicable over a decade later; the tropics are assumed be represented by this relationship well enough to obtain unbiased estimates of age difference; and linearly adjusting the data is assumed to sufficiently account for the changing tropospheric source.

**WACCM $SF_6$** The method to calculate age from $SF_6$ in WACCM is as follows: The $SF_6$ on pressure levels is zonally averaged and then averaged in the same latitudinal bins that were used for MIPAS. That zonally averaged $SF_6$ is then converted to age following Stiller et al. (2012). The reference curve for $SF_6$ is the zonal mean value in the tropics at 100hPa just north of the equator (0.5° N) with a one year low-pass fourth order Butterworth filter applied to remove the weak seasonal cycle. Results are insensitive to the filtering provided the filter is sufficient to obtain a strictly increasing reference curve. We use the same method for correcting the age of air for the nonlinear tropospheric growth, with a Newtonian iteration (see Stiller et al. 2012 equation 3). The nonlinearity correction is insensitive to the choice of constant parameter used to describe the relationship of the width of the age spectrum with the age. Once the age is determined, it is interpolated to isentropic levels using zonal

mean temperatures that have also been binned by latitude according to the MIPAS grid. No attempt is made either by Haenel et al. (2015) or in this work to adjust the age for the mesospheric sink.

**Statistics for 460 K overturning** To calculate the average overturning circulation strength where the two data estimates agree most closely (within 5% at 460 K), we average them. The error estimate is based on the variability in the total overturning circulation strength from WACCM calculated using $SF_6$-age to infer the circulation ($M/SF_6$-age $\Delta\Gamma$). We take the average of five annual averages chosen randomly from the annual averages from 1999–2014 100,000 times. The standard deviation of the 100,000 resulting mean circulation strength estimates ($0.14 \times 10^9$ kg/s) is taken to be half of the error. We repeated this procedure using the true overturning circulation strength ($\mathcal{M}$) and found smaller variations in the standard deviation ($0.09 \times 10^9$ kg/s). This error estimate assumes that WACCM represents the variability of the true circulation. The standard deviations of the five annual averages that were averaged for each data estimate were considerably smaller than these reported error bars. We therefore believe this is a conservative representation of the uncertainty in the diabatic circulation strength.

## 3.6 Supplementary Information for "'The strength of the meridional overturning circulation of the stratosphere"

Included in this supplementary information is a more thorough examination of age and age difference from the two satellite data products, GOZCARDS $N_2O$ (Froidevaux et al., 2013) and MIPAS $SF_6$ (Haenel et al., 2015). It includes how we chose the upwelling and downwelling regions, use of a different empirical relationship to calculate age from $N_2O$, a comparison between $N_2O$-age and MIPAS $SF_6$-age, an extrapolated extension of the $N_2O$ age difference, and plots of age of air from MIPAS $SF_6$ on surfaces above and below 500 K.

### 3.6.1 Choosing the upwelling region

Because satellite data do not reveal where air is upwelling and where it is downwelling, we must choose the latitudinal extent of the upwelling region in some other way. For this paper, we have chosen 35° N and S. Linz et al. (2016) showed that using 40° in a simple atmospheric GCM was very close to using the actual upwelling and downwelling regions at all heights (their Figure 8). To determine whether these are characteristic turnaround latitudes for the real atmosphere, we have plotted the total diabatic vertical velocity climatology from MERRA at four different levels in Figure 3-S1. The lower levels have less seasonal variability, while at upper levels, upwelling extends poleward of 50° in some seasons, and downwelling reaches nearly to the equator. We are satisfied with using 35° as an approximate average of this strong variability over the course of the year for all levels. The coarse meridional resolution of the GOZCARDS $N_2O$ (10°) does not lend itself to more precision than this, and choosing 40° for the upper levels with MIPAS makes little difference as the meridional gradient of age in the midlatitudes is relatively weak.

These climatologies are also useful to visualize the difference between the diabatic vertical velocity on isentropes and the transformed Eulerian mean vertical velocity on pressure surfaces, which has a narrower extent in the lower stratosphere and a wider extent in the upper stratosphere. The upwelling associated with the motion of the isentropes during the final warming is evident at all levels, and is not seen in the transformed Eulerian mean vertical velocity in pressure coordinates. This polar upwelling does not strongly bias the area-weighted age differences as compared to the mass-flux-weighted age differences because it occurs for such a short period of time and at the pole, where there is much less area, . Note that the climatology at 1200 K is somewhat suspect because of sparseness of observations that are assimilated at that level. (See Abalos et al. 2015, Figure 1.)

### 3.6.2 Calculating age from GOZCARDS $N_2O$

For this study, we used the empirical relationship between $N_2O$ and age of air from Andrews et al. (2001); it is a cubic that was calculated from a large number of aircraft flights, and it has a relatively wide range of $N_2O$ values over which it is apparently valid. To explore the robustness of this result, we have used two different empirical relationships, both linear,

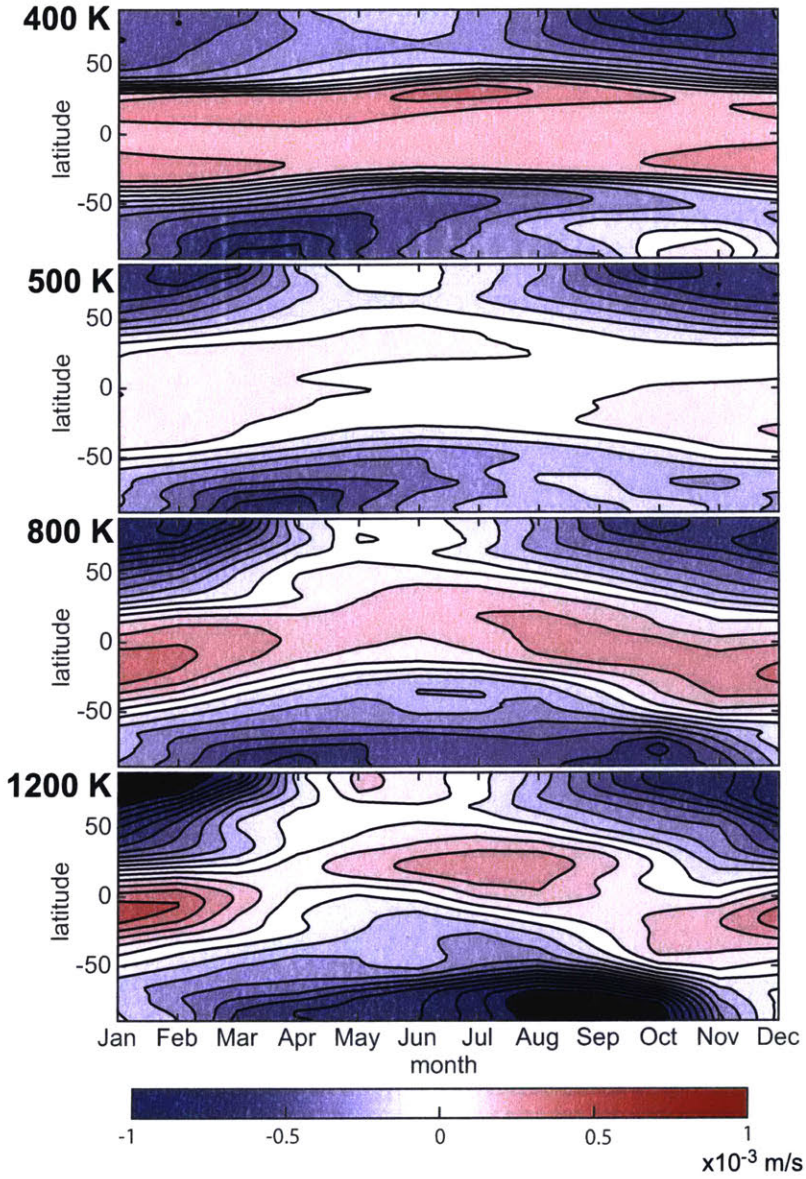


Figure 3-S1: Climatology of the zonal mean total diabatic vertical velocity, calculated as the total potential temperature tendency divided by the mean stratification ($\dot{\theta}/\Theta_z$), from MERRA monthly means from 1979–2013 on four different levels. At 1200 K, the vertical velocities at both poles in winter are larger than this color scale shows.

based on the data from Strahan et al. (2011) shown in Figure 3-S2 (courtesy of S. Strahan, personal correspondence).

The $N_2O$ data are six year means of observations from the Atmospheric Chemistry Experiment (ACE) instrument onboard SCISAT-1, 68°S-68°N from 150 hPa. The age data

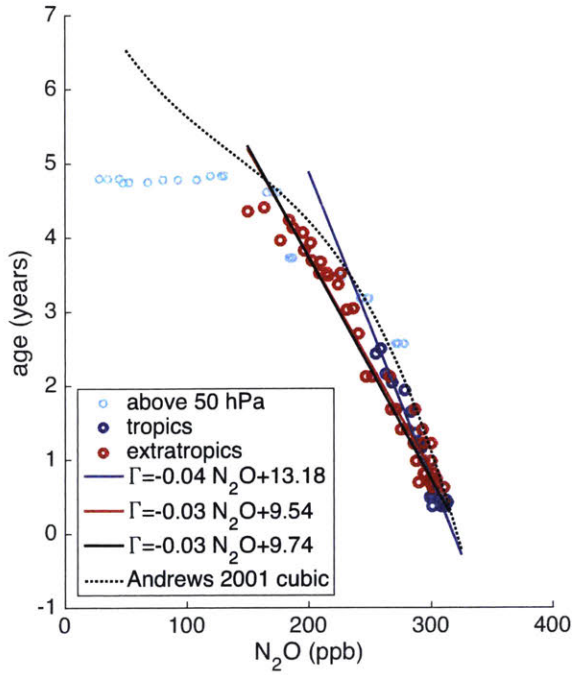


Figure 3-S2: Co-located age and $N_2O$ concentrations from balloons, ACE, and flights. Points above 50 hPa are in teal, tropical points below 50 hPa are in blue and extratropical points below 50 hPa are in red. Three different lines are shown. The black line is the overall fit to all points with $N_2O$ beneath 150 ppb. The red line is the fit to the extratropical points, and the blue line is the fit to the tropical points. The black dotted line shows the cubic relationship from Andrews et al. (2001), which has been adjusted for the trend in tropospheric $N_2O$ as described in the Methods.

are from balloon $CO_2$ profiles in the tropics and both $CO_2$ and $SF_6$ balloon measurements in the midlatitudes (Engel et al., 2009) and from the same aircraft flights used by Andrews et al. (2001) at 50 hPa. The points that overlap in altitude and latitude (regardless of timing) are shown in the scatter plot. This decision to look at colocated points without accounting for changes in timing neglects the considerable seasonal and interannual variability. The compact relationship appears to hold for values of $N_2O$ above 150 ppb and below 315 ppb. Although Strahan et al. chose to calculate the same fit including the tropical points and the midlatitude points together, there is reason to believe that the tropical and extratropical relationships should be different (Plumb and Ko, 1992), and so we have calculated the slopes separately for the tropical points and the extratropical points beneath 50 hPa (shown in blue and red lines) for comparison to the original fit (shown in the black line). The original fit, which was calculated from data up to 10 hPa in the tropics and up to 30 hPa in the extratropics, is dominated by the extratropical points, with the same slope and nearly the same intercept. When the tropics are treated separately, the relationship appears different. Both tropical and extratropical fits are performed using reduced major axis regression with each variable scaled by its standard deviation and are significant at the 95% level. To create

a smoother transition, the 35° points are the average of the age from the extratropical and the tropical fit ($\Gamma = -0.035 \times N_2O + 11.36$). However, there are still artefacts of using this relationship evident in the meridional gradient of the age, and so we do not calculate age difference using this. The original fit was used in Strahan et al. (2011). The cubic fit of Andrews et al. (2001) does not agree as well with these more recent data except in the tropics. In particular, the newer data never have an age above 5 years, whereas the measurements that went into the cubic fit included values of nearly six years. This difference could reflect a difference in the methods or a change in the $N_2O$ age relationship over the course of a decade.

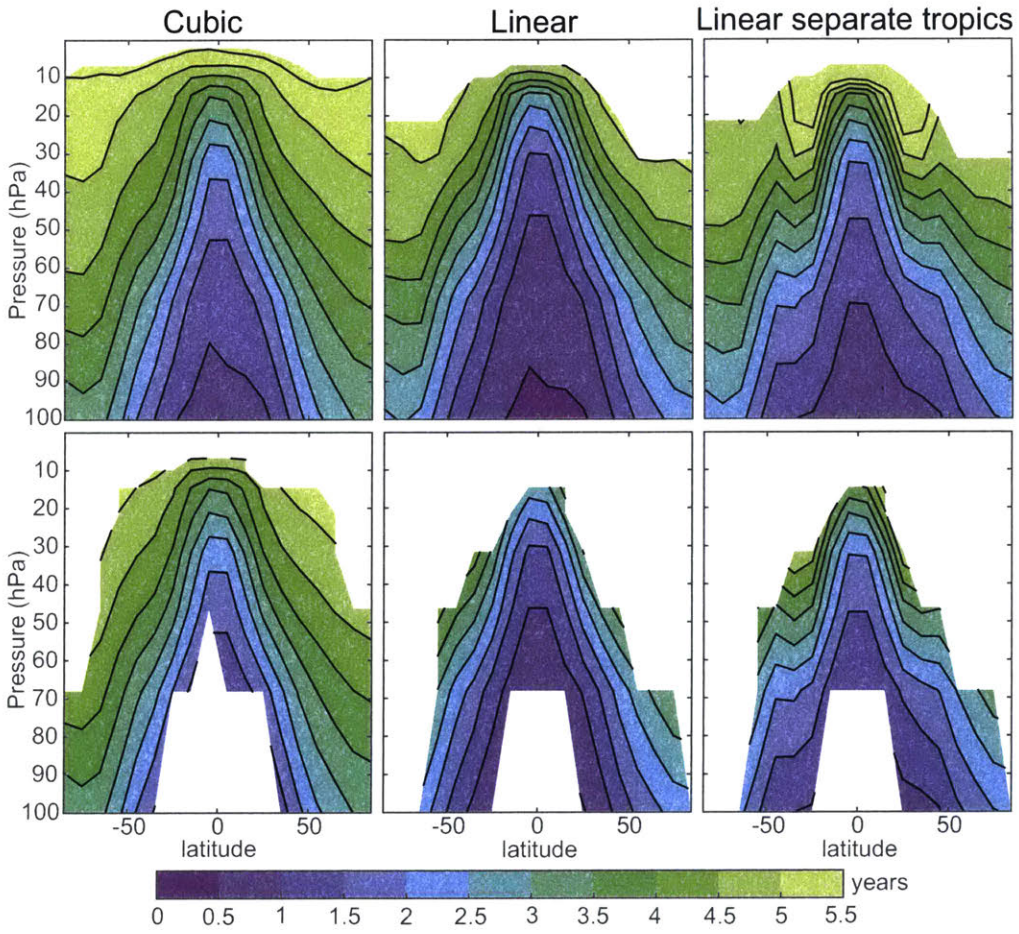


Figure 3-S3: The average age of air as a function of latitude and pressure based on GOZCARDS $N_2O$ data from 2007–2011 that has been converted to age of air using three different relationships: In the left column, the cubic relationship from Andrews et al. (2001) is used. In the middle column, the linear relationship determined by Strahan et al. (2011) is used. In the right column, the linear relationships shown above in Figure 3-S2 for the tropics and extratropics are used. The first row is the mean value neglecting any data gaps, and the second row is the mean value only where there are no data gaps for the five years. Contours are every half year.

Figure 3-S3 shows the zonal mean 2007–2011 mean age of air calculated using these three different empirical relationships. In the upper row, the mean values of the existing data are shown, neglecting data gaps. The bottom row shows only the points for which continuous data is available between 2007–2011. Ages are oldest using the cubic relationship (left), with the extratropics and tropics older than the age using the linear fit by about 0.5 yr for lower levels. The linear fit that does not treat the tropics separately (middle column) has the youngest tropical air, while fitting the tropics separately results in older air, though not as old as the cubic. Because the two linear fits were calculated with only data below 50 hPa, the relationship shown in the right column is only valid up to that level, and the transition between the two fits is very evident. The tropical data for the cubic relationship in the upper left panel is biased high because the only times the relationship holds at lower levels are when the tropical air has unusually low $N_2O$.

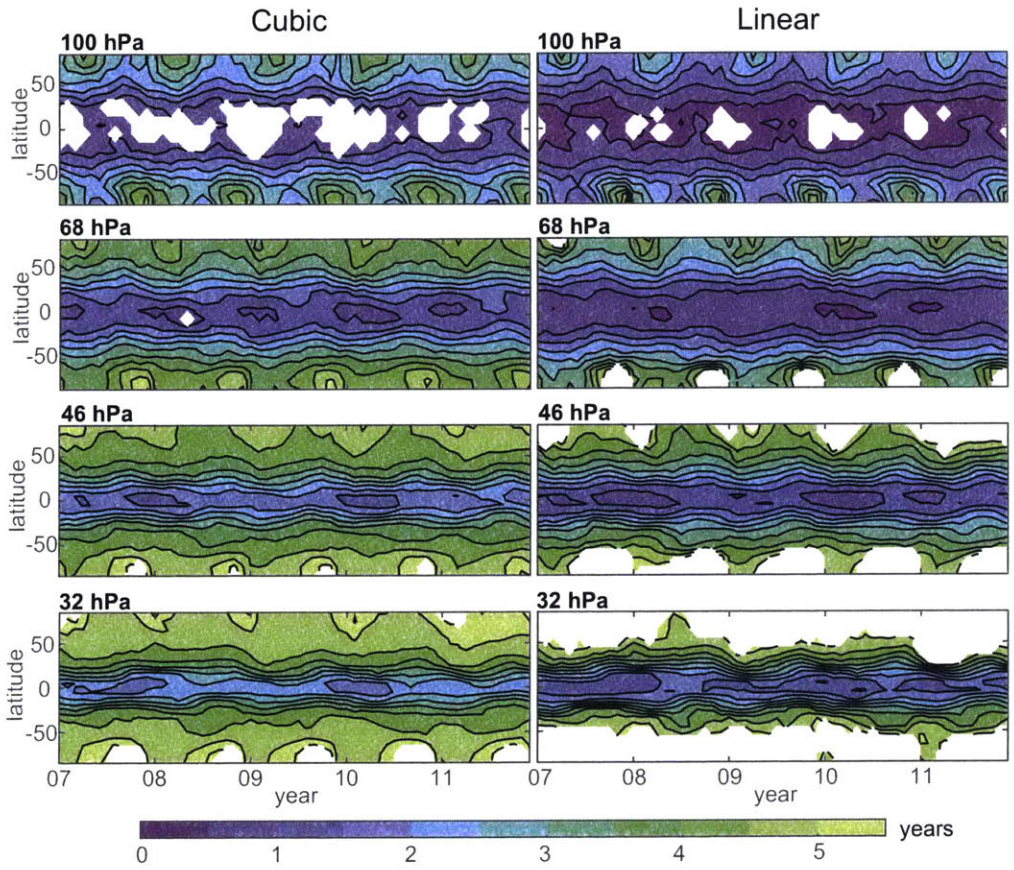


Figure 3-S4: 2007–2011 zonal mean age on four different pressure levels, calculated using the cubic empirical relationship between age of air and $N_2O$ (from GOZCARDS) based on Andrews et al. (2001) (left column) and using the linear empirical relationship between age of air and $N_2O$ based on Strahan et al. (2011). Contours are every half year.

We explore the data gaps and how they lead to biases by looking at the timeseries of the age determined using Andrews et al. (2001) and Strahan et al. (2011). These are shown at

five different pressure levels in Figure 3-S4. The ages calculated using the cubic relationship are older than those from the linear relationship. Because of the different ranges of $N_2O$ over which they are valid, the two relationships produce different data gaps. The cubic relationship does not hold above 300 ppb, making tropical coverage very limited at 100 hPa. At 68 hPa, there is only one gap in the data, and at 46 hPa, the data gaps are all now in the Southern Hemisphere winter pole, where the air is oldest. For the purposes of the paper, I have not used anything above 46 hPa , since the long data gaps in the Southern Hemisphere winter above that level will cause biases of unknown magnitude (there are no in situ measurements of South Pole $SF_6$ at these levels). Looking at Figure 3-S4, it is evident why this linear relationship was not appropriate for drawing conclusions about the strength of the circulation. The linear relationship holds only below 315 ppb, which adds some tropical coverage compared to the cubic relationship. However, already at 68 hPa, the polar air is getting below 150 ppb, the lower limit for this linear relationship, in Southern Hemisphere winter. By 46 hPa, the polar air is almost always out of the range of the empirical relationship. This relationship yields younger ages (about 0.5 yr) in the tropics and midlatitudes and similar ages at the poles. Because they are derived from the same data, the two different age relationships are highly correlated.

### 3.6.3 Comparison of GOZCARDS $N_2O$-age and MIPAS $SF_6$-age

This study benefits from having two completely independent global satellite data products that cover the same time period. This section presents a comparison of the age from these two different data products.

In Figure 3-S5, we show the monthly mean vertical profiles of age from MIPAS $SF_6$, and from the three different relationships between GOZCARDS $N_2O$ and age presented in Figure 3-S2. On the left is January 2007 in both a tropical and an extratropical Northern Hemisphere location. On the right is June 2011 for the same locations. The MIPAS $SF_6$ age is consistently older than the $N_2O$ age in the tropics, except at the lowest level in January of 2007. This is consistent with the high bias seen in Haenel et al. (2015). In the subpolar region, the cubic $N_2O$-age is closer to the MIPAS $SF_6$-age, and in June the $SF_6$-age is actually younger than the cubic $N_2O$-age. Both linear relationships produce ages from $N_2O$ that are younger than the MIPAS $SF_6$-age. Higher in the stratosphere, the difference between the extratropical $SF_6$-age and the cubic $N_2O$-age becomes more pronounced, with the $SF_6$-age being higher by at least two years at 20 hPa. It is possible that this is the influence of the mesospheric sink, though that would be more prominent at high latitudes only. The ages calculated using separate tropical and extratropical linear relationships agree more closely with the cubic relationship in the tropics and with the linear relationship in the extratropics. The seasonal difference is not large.

In order to calculate the age difference on an isentrope, both satellite data products are interpolated to isentropes on a finer grid than either are reported on. MIPAS $SF_6$-age is calculated at height levels, and both temperature and pressure are simultaneously retrieved. GOZCARDS $N_2O$ is reported on pressure levels. The interpolation method makes only a small difference. Nevertheless, it is important to recognize that the multiple isentropic levels reported here are, for $N_2O$, based on about three levels in the original data. Because of the seasonal motions of the isentropes in pressure, the data gaps look different from the gaps on pressure levels. Figure 3-S6 show timeseries of the zonal mean age of air from GOZCARDS $N_2O$ on isentropes using the cubic relationship and the linear relationship respectively. Figure 3-S7 shows the same for the MIPAS $SF_6$-age. The color bar is the same

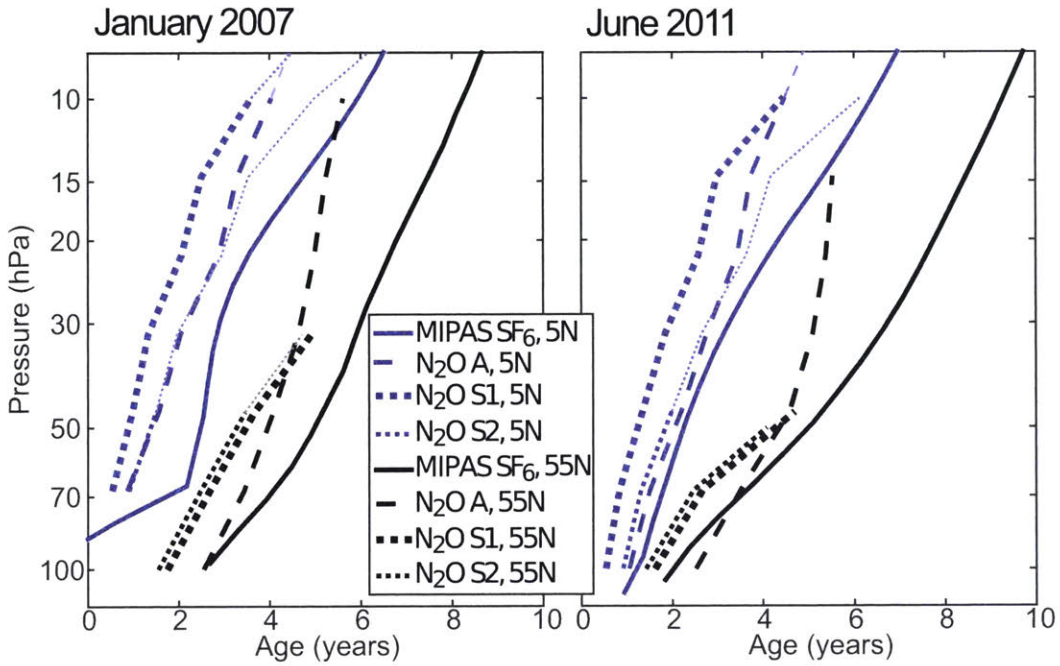


Figure 3-S5: Vertical profiles of age of air from MIPAS $SF_6$ and using three different empirical relationships for the relationship between $N_2O$ and age of air. The left panel is January 2007 and the right panel is June 2011. The blue lines show tropical profiles (5°N) and the black lines are extratropical or subpolar (55°N). Solid lines are MIPAS $SF_6$-age, long dashed lines are derived from the cubic relationship between $N_2O$ and age of air from Andrews et al. (2001), bold dotted lines are derived from the linear relationship between $N_2O$ and age of air from Strahan et al. (2011), and the thin dotted lines are derived from the different tropical and extratropical linear fits between $N_2O$ and age shown in Figure 3-S2. Where the profiles are based on extrapolation of the fit to levels for which there was no data informing the fit, they are shown in light blue and gray and are thin.

for all three figures, and has a maximum at 5.5 years, which is saturated for the $SF_6$-age. For the $N_2O$-age, the final warming period is associated with the 420 K surface dipping down below the measurement range of GOZCARDS, so the data gaps are the same for both top panels of Figure 3-S6. Other data gaps are different, based on where the two empirical relationships apply. Generally, again we can see that the cubic relationship results in older ages overall, except at the poles, where the linear relationship makes the air relatively older.

The MIPAS $SF_6$-age is noticably older than either of the $N_2O$-ages. Age on the 420 K surface is older than 5.5 years for the Southern Hemisphere wintertime vortex. This is surprisingly old, but there is no in situ data to compare with at those latitudes. The tropics do not show an obvious upwelling region, which can be inferred from the youngest ages being located at the equator for the $N_2O$-age at this level. At 450 K, the timeseries look more similar, with all three age estimates showing the disturbed Northern Hemisphere winters of 2009 and 2010, as can be seen from the younger air around the turn of the year in each case. The linear relationship between $N_2O$ and age produces the youngest tropical ages, the cubic somewhat older, and the MIPAS $SF_6$-age is clearly the oldest. This is consistent with the

old bias shown in validation papers on this product (Stiller et al., 2012; Haenel et al., 2015).

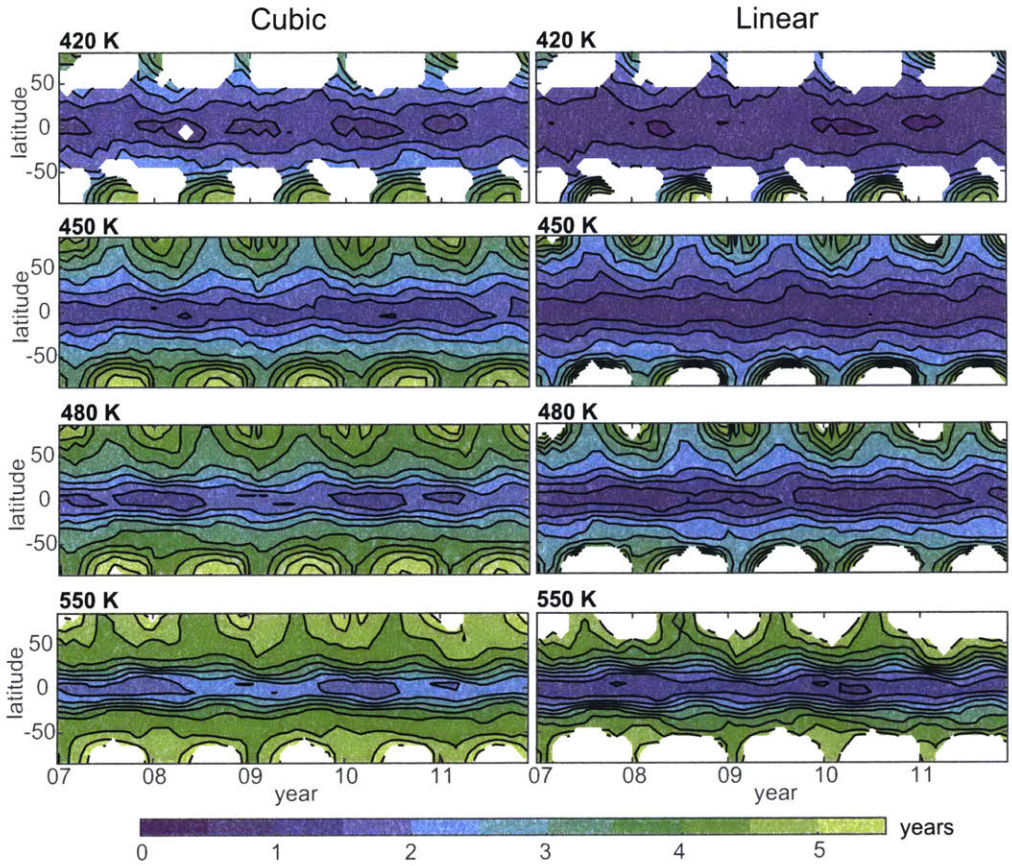


Figure 3-S6: 2007–2011 zonal mean age on four isentropic levels, calculated using the cubic empirical relationship between age of air and $N_2O$ (from GOZCARDS) based on Andrews et al. (2001) (left column) and the linear relationship between age of air and $N_2O$ based on Strahan et al. (2011). Contours are every half year.

### 3.6.4 Calculating age difference and circulation strength from GOZCARDS $N_2O$

Figure 3-S8 shows the 2007–2011 average zonal mean age calculated from $N_2O$ in three different ways (as in Figure 3-S5) interpolated to isentropes. At no level does the linear relationship have no gaps, and as these gaps are consistently of old polar air, this will create a systematic bias. Nevertheless, we have extended the age difference calculation using the available data. We have ignored the missing data and calculated the average upwelling age as the average age for the available data in the upwelling region, and the average downwelling age as the average age for the available data in the downwelling region. This will tend to lead to a low bias in age difference where the tropics are missing and a high bias in age difference where the poles are missing. The polar bias will be smaller because the poles represent such a small total area. We have extrapolated between 450 K and 550 K although

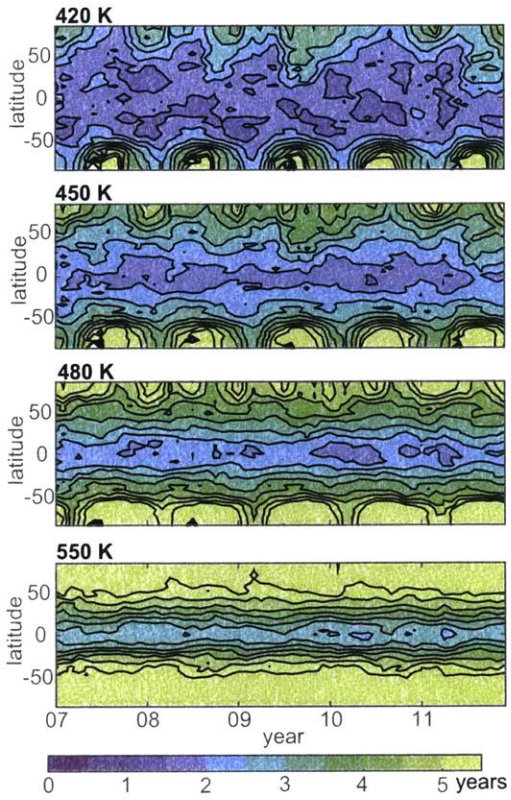


Figure 3-S7: 2007–2011 zonal mean age on four isentropic levels from MIPAS $SF_6$. Contours are every half year and the color bar is saturated at 5.5 years for comparison with Figure 3-S6. The Southern Hemisphere vortex gets much older than this, as can be seen in Figure 3-S10.

the only level for which the $N_2O$-age has no gaps is the 460 K surface, which is around 60 hPa in the tropics and close to the 68 hPa surface overall. This is for the cubic relationship only–the linear relationship still has gaps in the Southern Hemisphere vortex.

We have reported the value of the total overturning at 460 K in Table 3.1. The three data products are all within 5% of the mean value (where $N_2O$-age has been given equal weight as $SF_6$-age). WACCM is very close to the total overturning strength. The three reanalysis products, however, are a bit further away. The average value of the total overturning circulation $7.3\times10^9$ kg/s is derived from two completely independent satellite data products and is insensitive to the treatment of the $N_2O$-age. The only bias left then is that the age difference calculated using area-weighting rather than mass-flux-weighting is biased 10% or less low at that level. This means that our calculation is at most a 11% overestimate of the total overturning strength. Therefore, we can surmise that JRA 55 is too strong and MERRA is dramatically too weak at this level. ERA-Interim is barely within the tolerable error, assuming that the bias is indeed 10% high and accounting for the $\pm0.3 \times 10^9$ kg/s error bar.

We note, also, that MIPAS $SF_6$-age is evidently too old at the poles above 500 K due to

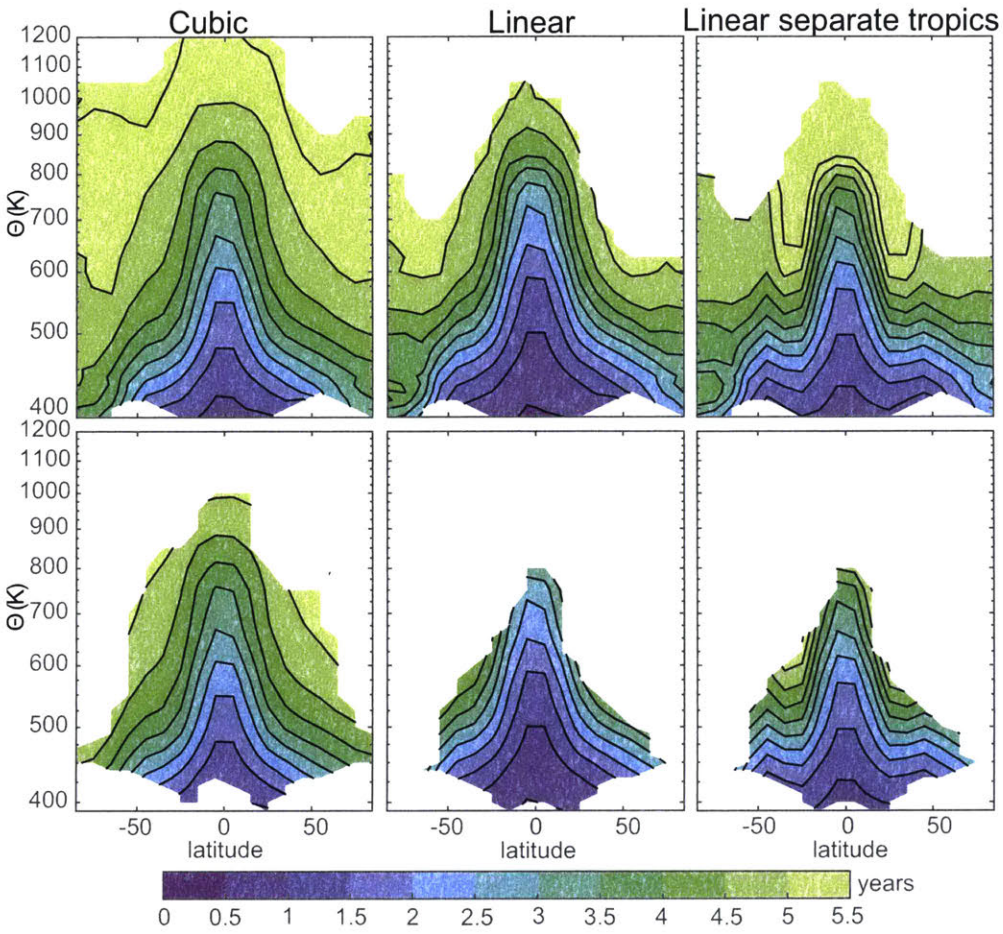


Figure 3-S8: The average age of air as a function of latitude and potential temperature based on GOZCARDS $N_2O$ data from 2007–2011 that has been converted to age of air using three different relationships: In the left column, the cubic relationship from Andrews et al. (2001) is used. In the middle column, the linear relationship determined by Strahan et al. (2011) is used. In the right column, the linear relationships shown above in Figure 3-S2 for the tropics and extratropics are used. MERRA pressure and temperature has been used to convert to isentropic surfaces. The first row is the mean value neglecting any data gaps, and the second row is the mean value only where there are no data gaps for the five years. Contours are every half year.

the influence of the mesosphere. However, based on the modeled $SF_6$-age in WACCM, this effect is not felt below 500 K. Furthermore, this level is considerably above the level where, based on Figure 3-S6, the upwelling signal is ambiguous. Both data products are reliable at this same level, and remarkably, they agree.

Figure 3-S9 shows the extended age difference calculated using the cubic and the linear relationship. Where there is not continuous data, we have little confidence in this result. The slopes of these two are distinctly different, with the cubic relationship aligning much

| Data set | 460 K overturning ($\times 10^9$ kg/s) |
|---|---|
| MIPAS $SF_6$-age | 7.43 |
| GOZCARDS $N_2O$ cubic | 7.17 |
| GOZCARDS $N_2O$ linear | 7.05 |
| WACCM | 7.11 |
| JRA 55 | 7.90 |
| MERRA | 5.52 |
| ERA-Interim | 6.48 |

Table 3-S1: Total overturning circulation strength at the level for which both satellite data sets exist.

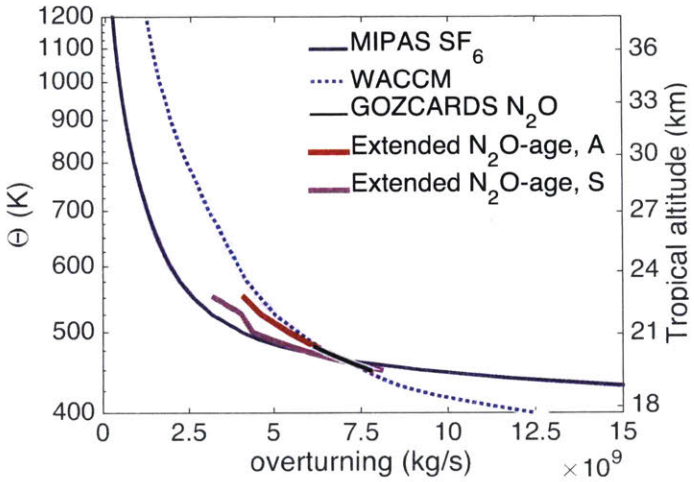


Figure 3-S9: Like Figure 3-5, the average total meridional overturning circulation strength for 2007–2011 as a function of potential temperature. The strength from MIPAS $SF_6$-age and the simultaneously retrieved temperature and pressure is shown in the navy solid line. The dotted blue line shows the total meridional overturning strength from the WACCM model. The bold red line is an extension of the cubic relationship between age of air and $N_2O$, ignoring data gaps. The bold magenta line is based on the linear relationship between age of air and $N_2O$, ignoring data gaps. The black line is from the cubic relationship, and spans the levels for which the data gaps are minimal, including 460 K where there are no gaps at all.

more closely with the model, and the linear relationship aligning with the MIPAS $SF_6$-age circulation strength. A more careful characterization of the compact relationship between age of air and $N_2O$ (or methane, which is closely related) could yield much more certainty for the overturning circulation strength at these low levels.

### 3.6.5 MIPAS age on isentropic surfaces

Finally, we show the MIPAS $SF_6$-age data on isentropic surfaces throughout the depth of the stratosphere.

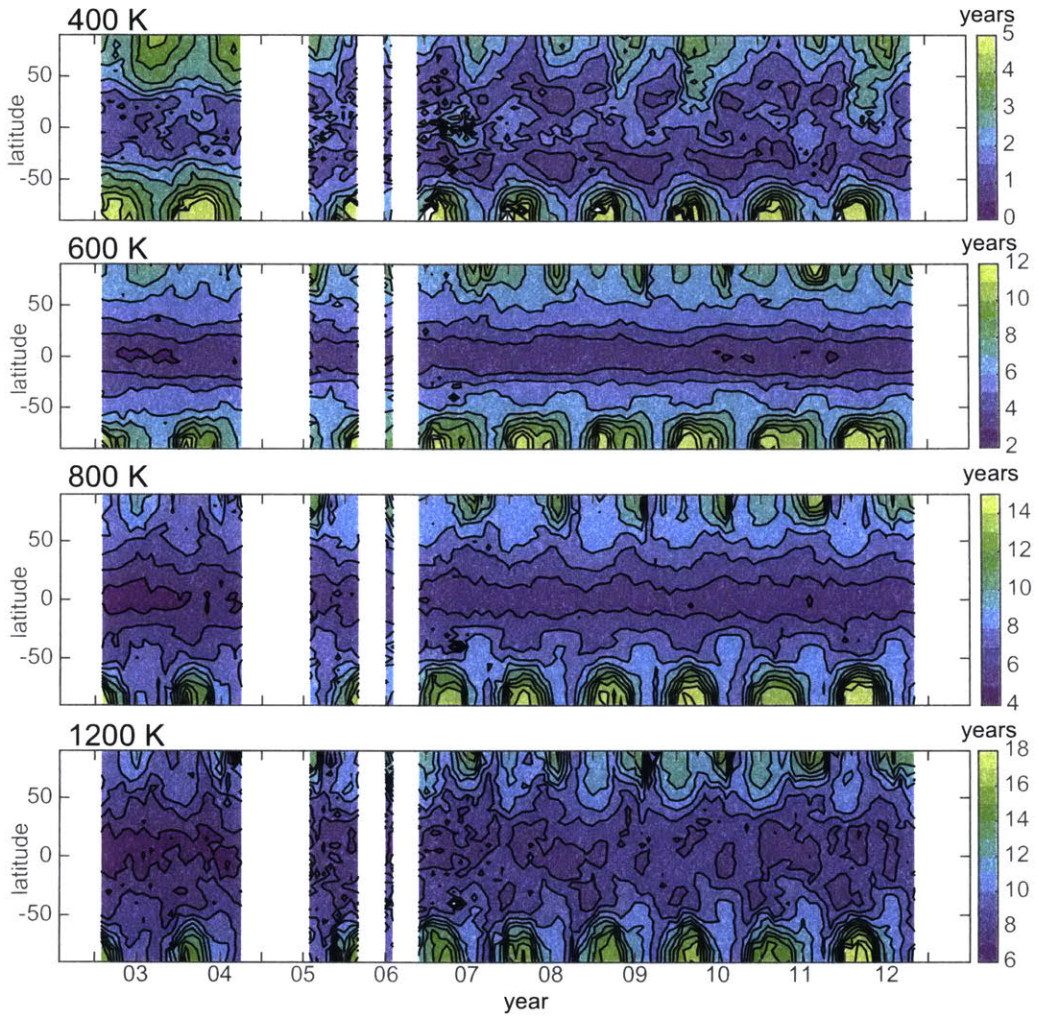


Figure 3-S10: Age of air from MIPAS $SF_6$ data on the 400 K, 600 K, 800 K and 1200 K surfaces. Note that the color scale is not the same for these four plots.

# Chapter 4

# Using the global overturning diabatic circulation of the stratosphere as a metric for Brewer Dobson Circulation

This chapter is a paper in preparation for Atmospheric Chemistry and Physics: Marianna Linz, R. Alan Plumb, Marta Abalos, Diane J. Ivy, Douglas E. Kinnison, and Alison Ming: Using the global overturning diabatic circulation of the stratosphere as a metric for Brewer Dobson Circulation. ML performed the research and wrote the manuscript, under the supervision of AP. MA provided the TEM timeseries. DI provided the SBUV data. DK ran the WACCM model. AM provided the diabatic heating rates from ERA-I.

## 4.1 Introduction

The Brewer–Dobson circulation (BDC), the meridional overturning of mass in the stratosphere, is important for the distribution of gases in the stratosphere (Butchart, 2014) including water vapor, the radiative effects of which have been shown to impact surface climate (Dessler et al., 2013), and ozone, which impacts surface circulation (e.g., Polvani et al., 2011). The BDC is frequently quantified by the vertical velocity in the Transformed Eulerian Mean (TEM) framework (Andrews et al., 1987), averaged over the tropics in models and reanalysis products (e.g. Butchart et al., 2006; Li et al., 2008; Seviour et al., 2012; Hardiman et al., 2017). In steady state, the total upwelling and downwelling mass fluxes must be equal, and so characterizing the tropics alone is considered sufficient. The TEM framework provides formalism that approximates the Lagrangian-mean mass transport, and in the limit of adiabatic, small-amplitude eddies, the TEM residual mean circulation is equivalent to the density-weighted isentropic mean circulation. The value and trends of the residual mean circulation average tropical vertical velocity through the 70 hPa level have been used in multimodel comparisons (Butchart et al., 2010) and in comparisons between different reanalysis products (Abalos et al., 2015; Kobayashi and Iwasaki, 2016). The 70 hPa level is consistently within the stratosphere even in climate models that have trouble with their tropopause. As it is in the lower stratosphere, it approximates the mass flux between the troposphere and stratosphere and is related to the water vapor flux and ozone transport.

The TEM vertical velocity is a useful metric for understanding stratospheric dynamics. However, apart from its the theoretical relationship with the Lagrangian-mean mass transport, it is not straightforward to relate the TEM vertical velocity to the tracer transport that is so important to climate. The theory presented in Chapter 2 to directly relate the idealized tracer age of air to the global average diabatic overturning circulation through isentropes and the subsequent application of the theory to observations in Chapter 3 has provided motivation to use the global mean overturning diabatic circulation through isentropes as a metric for the BDC strength in place of or at least in addition to the TEM vertical velocity. Other metrics are more familiar, but the diabatic mass flux through isentropes can be—and has been— observationally constrained (see Table 3-S1).

This chapter serves to explore the diabatic circulation on isentropic levels as a new metric for the circulation strength. We begin in Section 4.2 with a clear explanation of the steps for calculating this metric, the necessary model output, and its advantages from that perspective. This will include some repetition from Sections 3.3 and 3.4 and expand upon these, which necessarily described the calculation in extreme brevity. In Section 4.3, we first examine three different calculations for the TEM vertical velocity, including the underlying assumptions. Then we compare the total global diabatic circulation on isentropes to the more traditionally used TEM vertical velocity calculated in these three different ways (Abalos et al., 2015) for the same three different reanalysis products used in Chapter 3. Thus we determine how the information provided by this new metric compares to the information more traditionally used, and we find close agreement between the diabatic circulation strength and one of the three calculation methods for the TEM vertical velocity. We evaluate the trends in the diabatic circulation from these three reanalysis data products and demonstrate that although there are trends in upwelling through pressure surfaces, the diabatic overturning through isentropes does not have the same clear trends. This result implies that much of the trend in the BDC might be attributable to changes in the thermal structure, supporting the conclusions of Oberländer-Hayn et al. (2016). Finally, in this section we examine the upper and lower branches of the circulation in the diabatic circulation. In

Section 4.4, we examine the relationship between the diabatic overturning circulation and stratospheric ozone, using data, reanalyses, and the Whole Atmosphere Community Climate Model (see 3.2 for the model description). One motivation frequently cited for studying the BDC is that it impacts ozone and could impact the ozone hole recovery. We find that the lower branch of the circulation is important for the polar ozone, while the upper branch is the most important for subtropical ozone. The latter relationship is driven by the temperature dependence of the photochemistry. Section 4.5 summarizes the results and discusses implications and future work.

## 4.2 Calculating the diabatic overturning circulation on isentropes

Why would we need a different metric for the BDC? The residual mean tropical upwelling at 70 hPa has been used for at least a decade (Butchart et al., 2006). However, this is neither directly observable nor is it easily relatable to observations. A metric for models and reanalyses needs to be able to be constrained by data. In a reworking of the Tropical Leaky Pipe (Neu and Plumb, 1999), Linz et al. (2016) (Chapter 2) showed a direct relationship between age of air and the diabatic circulation through an isentropic surface. We demonstrated that the difference between the age of air that is downwelling and the age of air that is upwelling through each isentrope is inversely proportional to the diabatic mass flux through that surface, in steady state and neglecting diabatic diffusion. Thus, the global mean overturning diabatic circulation through isentropes reflects the total Lagrangian mean mass or tracer flux. In Chapter 3, this theory was applied to two different satellite data products to calculate a robust observationally-based constraint on the stratospheric circulation, and the overturning circulation strength of two of the three reanalysis products that we examined (and use here) were shown to disagree with the observations at 460 K. This is can be used as a constraint for climate models as well, and we showed that WACCM agrees with the circulation strength based on the satellite data.

We calculate the diabatic overturning as in Chapter 2. We define the total upwelling mass flux and the total downwelling mass flux through an isentropic surface:

$$\mathcal{M}_u = \int_{up} \sigma \dot{\theta} dA, \text{ and} \tag{4.1}$$

$$\mathcal{M}_d = -\int_{down} \sigma \dot{\theta} dA. \tag{4.2}$$

$\dot{\theta}$ is the total diabatic heating rate, and $\sigma = -g^{-1}\partial p/\partial\theta$ is the isentropic density. The limits of integration are the regions of the isentrope through which air is upwelling ($\dot{\theta} >= 0$) and downwelling ($\dot{\theta} < 0$) instantaneously. Since the monthly mean is not in equilibrium, some amount of storage may take place, and these two will not necessarily be equal. We therefore define the total overturning circulation following the time-dependent formulation of Section 2.2.3, (2.21): $\mathcal{M}(\theta) = 1/2\,(\mathcal{M}_u - \mathcal{M}_d)$. This is an arbitrary but sensible definition; it accounts for simultaneous variability in the extratropics and in the tropics, thus providing and instantaneous global average overturning circulation strength.

To calculate the diabatic circulation from model output or reanalysis, one thus needs the total diabatic heating rate, the isentropic density, the temperature, and the pressure. The diabatic heating rate is output differently in different models, but it is fundamentally

straightforward. In the atmosphere the diabatic heating rate consists predominantly of two terms, the latent heat fluxes from phase changes of water and the radiative heating and cooling (Fueglistaler et al., 2009). For levels wholly within the stratosphere, water vapor concentrations are so low that the former is negligible. Models may output other diabatic terms, such as mixing from parameterized gravity waves; alternatively, they may output a total temperature tendency, which contains all of the necessary information in just one term. Almost all models will output these terms on either pressure or model levels. The diabatic heating rate on those levels must then be interpolated to isentropic levels, for which the temperature and pressure fields are necessary. The isentropic density can be calculated by finite difference in pressure and then interpolated to isentropes as well.

Since eddies serve to predominantly mix adiabatically, they are less important for the diabatic circulation through isentropes. In the conversion from the diabatic vertical velocity on pressure surfaces to the diabatic vertical velocity on isentropes, the covariance of the diabatic vertical velocity and the isentropic levels could nevertheless be important. Fortunately this covariance is small enough that monthly mean temporal resolution is sufficient to accurately calculate the circulation; specifically, in ERA-Interim using monthly means instead of 6 hourly means results in no bias throughout most of the stratosphere and up to a 10% bias at the poles in wintertime, which, as the pole is a small area of the globe, is a much smaller bias on the total overturning mass flux. While many models do output monthly mean eddy fluxes to calculate the residual circulation, others, especially older model runs, do not. Almost all models output shortwave and longwave radiation, and as these are by far the dominant terms in the total diabatic heating rate, this metric can be calculated using models that did not report the necessary terms or have the necessary temporal resolution for the residual circulation vertical velocity calculation. The comparatively minimal data requirements for this metric recommend it.

We note that the diabatic circulation strength is a good indication of the integrated eddy forcing on the circulation, but it does not diagnose which eddies are responsible. Thus, models could get the right circulation from the wrong waves.

The constraint provided by Chapter 3 only applies to the long-time mean of the circulation strength; at least 5 years of averaging are required. However, in Chapter 2, we showed the potential for the time-varying theory to calculate the seasonal cycle of the diabatic circulation strength through isentropes as well. Provided long records of accurate age data, that theory holds promise for constraining both the magnitude and timing of the seasonal cycle in models by using age of air data.

## 4.3 The diabatic circulation and TEM vertical mass flux in three reanalyses

The BDC was originally hypothesized to explain tracer measurements (Dobson et al., 1929; Brewer, 1949), and therefore the Lagrangian mean transport is, in some sense, the appropriate formalism to study. The TEM residual circulation is not the same as the Lagrangian mean mass transport, as noted explicitly in Andrews and McIntyre (1976). However, under certain conditions (small amplitude, adiabatic eddies), the Lagrangian mean circulation and the TEM residual circulation are identical. The TEM equations also provide unique insight into the forcing of the mean flow by eddies; when the quasigeostrophic approximation holds, the only internal forcing of the mean state by the eddies is encompassed by the divergence of the Eliassen-Palm flux (Edmon et al., 1980). Thus, because of the ready interpretation of

the wave-mean flow interactions, the TEM residual mean circulation has been the primary diagnostic for models and observations of the stratosphere. In the following section, we try to understand differences in the common methods for calculating this diagnostic, and the relationship of the TEM residual circulation vertical velocity with the global diabatic circulation strength.

### 4.3.1 Comparison of TEM vertical velocity calculation methods

Abalos et al. (2015) performed an extensive reanalysis intercomparison of the trends in the TEM vertical mass flux calculated in multiple ways from ERA-Interim, MERRA, and JRA-55. The three different methods for calculating the mass flux are summarized as follows, and for more details see their original paper. The first method is the residual circulation (Andrews et al., 1987), $\bar{w}^*$, in which the residual vertical velocity is calculated based on the Eulerian mean vertical velocity and the meridional eddy heat flux.

$$\bar{w}^* = \bar{w} + \frac{1}{a\cos\phi}\left(\cos\phi\frac{\overline{v'T'}}{S}\right)_\phi, \tag{4.3}$$

where S is the static stability. This method, which we will refer to as the "direct" method relies on the vertical velocity field from the reanalyses, which is often noisy. The second calculation of the BDC, $\bar{w}^*_M$, is based on the "downward control" principle (Haynes et al., 1991), and is calculated using momentum balance equation, integrating the difference of the divergence of the Eliassen-Palm Flux and the zonal mean zonal wind tendencies on surfaces of constant "angular" momentum (in this case, constant latitude) to derive a streamfunction (Randel et al., 2002). The assumption of isolines of angular momentum being equivalent to latitude lines could lead to errors in this estimate. Both of these methods fundamentally assume quasigeostrophic motion. The final estimate, $\bar{w}^*_Q$, is calculated by iterating the thermodynamic balance and the continuity equation with no net mass flux across a pressure surface (Murgatroyd and Singleton, 1961; Rosenlof, 1995). Any errors in the heating rates will be reflected in this calculation. Because this estimate is also derived from the heating rates, this should be the most closely related to the diabatic overturning circulation.

The first two of these methods both require at least 4 times daily data, while the thermodynamic $\bar{w}^*_Q$ requires monthly data (Lin et al., 2015). Both the direct method and the downward control method require an assumption of quasigeostrophy, whereas the thermodynamic method does not (although for the purposes of the $\bar{w}^*_Q$ in this study, the same frequency of data was used for all three). Thus, we might expect that the two quasigeostrophic, high-frequency data derived estimates would be very similar. Butchart et al. (2006) calculated the mean and the trend in the residual vertical velocity using both methods in a variety of models and found that they were generally similar in magnitude and structure, though differences between the two calculations varied more than differences in the interannual variability of each individual calculation. Rosenlof (1995) compared the thermodynamically calculated streamfunction to the downward-control streamfunction and found them to be similar, but with the strongest differences in the lower stratosphere. Abalos et al. (2015) also performed a qualitative comparison between the mean streamfunction for these three estimates, noting that the thermodynamic calculation is larger in the lower stratosphere and with more differences between the downward-control calculation and the other two estimates higher up in the stratosphere at the poles.

For this paper, we use the deseasonalized timeseries of these nine estimates of the BDC

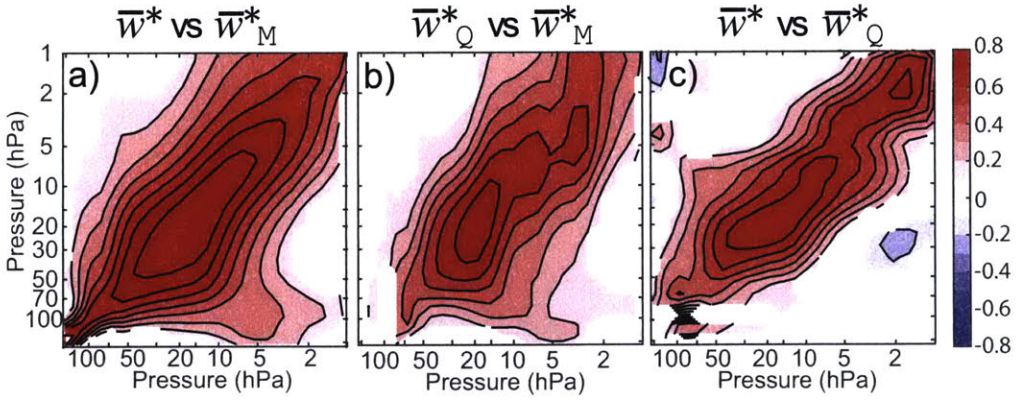


Figure 4-1: correlation coefficients for the deseasonalized time series of the three different TEM vertical velocities calculated from ERA-Interim (a) $\bar{w}^*$ with $\bar{w}^*_M$, (b) $\bar{w}^*_Q$ with $\bar{w}^*_M$, and (c) $\bar{w}^*$ with $\bar{w}^*_Q$.

strength integrated over the tropics (Abalos et al. 2015, Figure 8) at levels throughout the depth of the stratosphere. In Figure 4-1, we show the matrix of correlation coefficients ($r$) for each estimate with each other estimate from just one of the reanalyses, ERA-Interim. Behavior is similar for the other two, and so we do not include them here. Temporal correlations were performed using reduced major axis regression, scaling each of the timeseries by its variability. These coefficients therefore represent the correlation of the deseasonalized variability of the different TEM calculations. The first panel shows the correlation between the direct calculation on the y-axis with the downward-control calculation on the x-axis. As expected, the correlation of these two calculations at the same level is very high between these two estimates ($r > 0.9$ along the diagonal between 50 and 10 hPa). We see the evidence of the impact of the downward-control calculation, as the correlations of the lower level $\bar{w}^*$ with the upper levels of $\bar{w}^*_M$ are much higher than the opposite. The downward-control theory means that the lower levels are highly correlated with the upper levels, since the upper levels control them, and so the spatial autocorrelation of $\bar{w}^*_M$ is very broad. The spatial correlation is relatively broad between these two estimates. The second panel shows the correlation of the thermodynamic TEM vertical velocity with the downward-control calculation. Again, we see evidence of the downward control effect, with the correlations spanning much deeper along one axis than the other. The correlation beneath 70 hPa is not significant, consistent with the substantial differences at low levels seen in the mean by both Rosenlof (1995) and Abalos et al. (2015). Rosenlof speculated that this was because of the relatively simple way the radiative heating was calculated, but the true reasons are not clear, since in the much more complicated reanalyses of Abalos et al., the same result is seen. At upper levels, the correlation breaks down, consistent with the discontinuities in the heating rates above 5 hPa noted by Abalos et al. (2015). Specifically, in all three reanalyses there are jumps in the heating rates above 5 hPa that are associated with changes to the data that is being assimilated rather than to true circulation changes, since the reanalyses adjust in different directions. The third panel shows $\bar{w}^*$ on the y-axis and $\bar{w}^*_Q$ on the x-axis. The correlation of these is a bit higher in the lower most stratosphere, and spans a narrower range. The thermodynamic calculation thus has more vertical variation than either of the other two calculations. These three calculations, often treated as the same, are actually

somewhat different, especially with respect to the vertical structure of their interannual variability.

### 4.3.2 TEM vertical velocity compared to the global diabatic circulation strength

We calculate the correlation of the three different calculations of the TEM vertical velocities with the deseasonalized diabatic circulation strength on each isentrope (as defined above) for each of the three reanalysis data products. This results in a matrix of correlation coefficients that reveals the relationship between these different metrics. These nine correlation coefficient matrices are shown in Figure 4-2. The tightest and highest correlation ($r > 0.8$) is found between the diabatic circulation on isentropes and the $\bar{w}^*_Q$, as expected, because these are both calculated from the heating rates. The 70 hPa $\bar{w}^*_Q$ variability is captured in all three reanalyses by the 400–420 K diabatic overturning. The 10 hPa $\bar{w}^*_Q$ variability is captured in all three reanalyses by the diabatic overturning between 800–900 K. The relationship with the other TEM vertical velocities is less clear. $\bar{w}^*$ at 70 hPa is not strongly correlated with the diabatic circulation strength at any level, with the correlation coefficient only reaching up to $r = 0.5$ (at 550 K for both JRA55 and MERRA and between 550 and 650 K for ERA-Interim). The 10 hPa correlation is stronger and consistently located amongst the reanalyses, although the vertical structure of the correlations between the two levels varies. The momentum derived vertical velocity is the least well correlated, with the lower level diabatic circulation strength having almost no covariability with $\bar{w}^*_M$ at any level. We conclude from this comparison that the diabatic circulation through isentropes is very closely related to the TEM vertical velocity calculated using heating rates with less covariation with $\bar{w}^*$ and even less with the momentum derived vertical velocity, $\bar{w}^*_M$. Similar to Abalos et al. (2015), we generally see as much difference amongst the different estimates of the vertical velocity as between the three reanalyses.

We calculate the trends from the three different reanalyses and also from the WACCM model run over the same time period, and the results of this are shown in Figure 4-3. These results are similar to those found by Abalos et al. (2015) for ERA-I, but the trends for JRA 55 and MERRA are much less statistically significant. ERA-I shows an acceleration of the lower branch of the circulation and a deceleration of the upper branch. MERRA shows an acceleration around the midstratosphere, where the upper branch begins, and in the uppermost stratosphere. JRA 55, meanwhile, only has a small region in the midstratosphere where it shows a statistically significant trend. This is also an acceleration. WACCM meanwhile, has no statistically significant trend at any level. Note that because of the heating rates being somewhat questionable above 800 K, the trends there are to be treated with caution.

### 4.3.3 The anticorrelation of the upper and lower branches of the circulation

In Figure 4-2, all of the correlations shown in colors are significant at the 95% confidence level, and so the consistent pattern of blue in the upper left corner of six out of the nine panels is conspicuous. This implies that the upper level circulation is anticorrelated with the lower level circulation. To explore this in more detail, we calculate the spatial autocorrelation function at zero lag for the different estimates of the circulation strength. In the three TEM metrics, there are at most weak anticorrelations between the lower level circu-

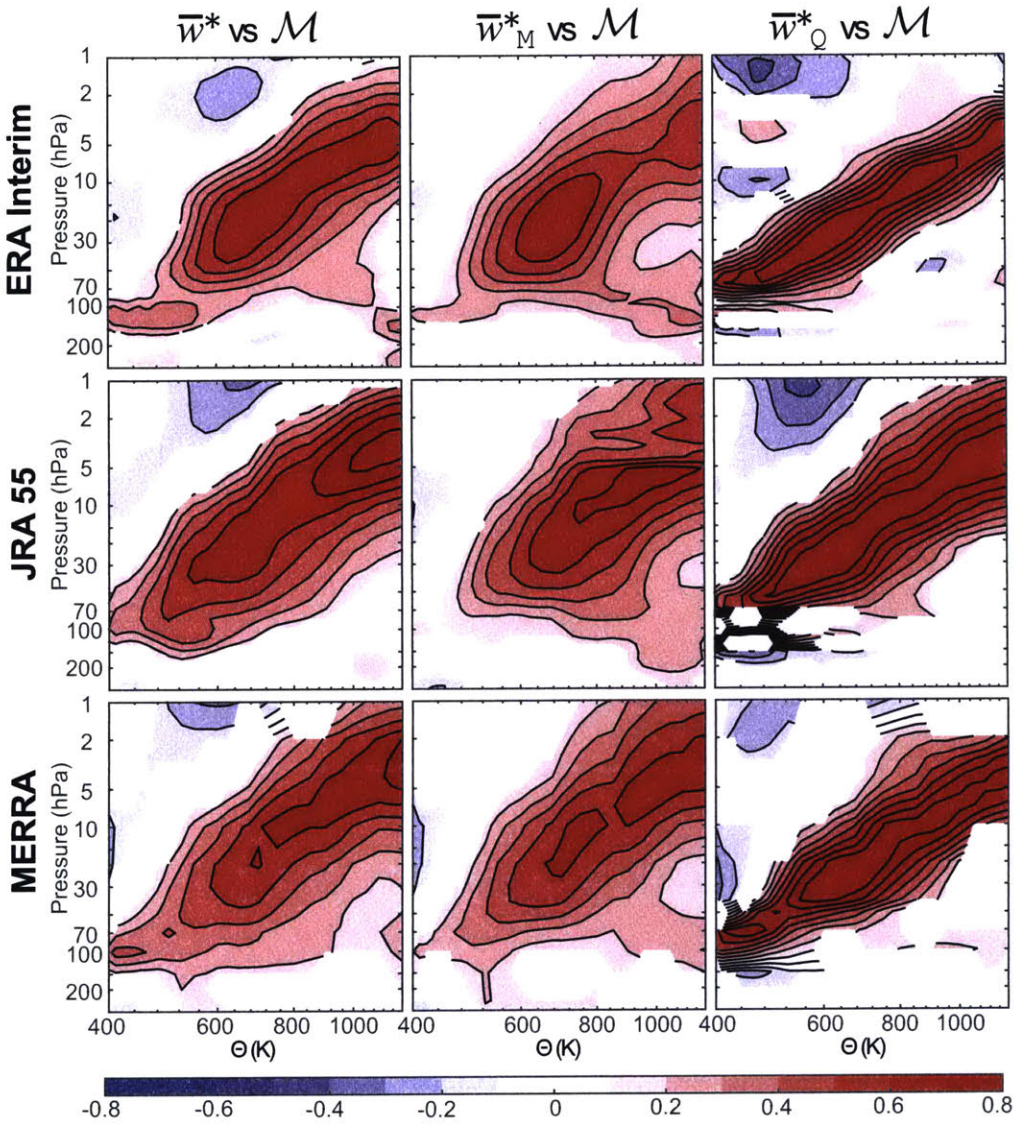


Figure 4-2: The correlation of the interannual variability of three different estimates of the TEM vertical velocity with the interannual variability of the diabatic circulation $\mathcal{M}$. The first row is ERA-Interim, the second row is JRA55 and the third row is MERRA. The first column is the correlation with $\bar{w}^*$, the second is the correlation with $\bar{w}^*_M$, and the third is the correlation with $\bar{w}^*_Q$. Correlations are shown only where they are significant at the 95% confidence level. Contours are spaced every 0.1.

lation and the upper level circulation. They appear most prominently in $\bar{w}^*_Q$ (not shown). However, calculating the autocorrelation function of the diabatic circulation strength on isentropes, the anticorrelation of the lower and upper branches of the circulation becomes evident, and this is shown in Figure 4-4. In all three reanalysis products as well as in a

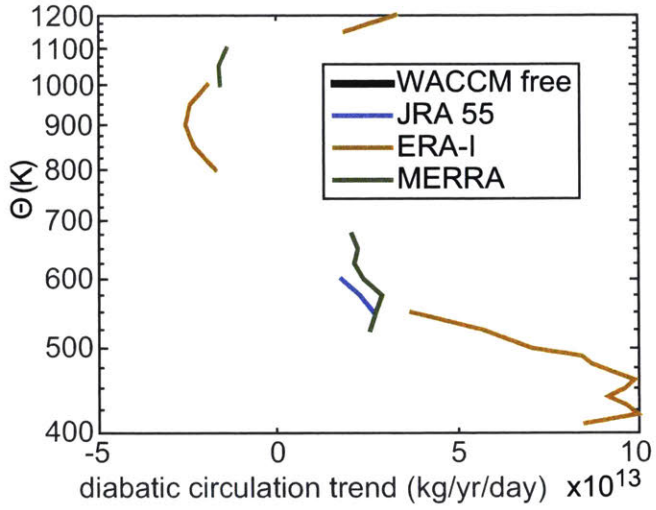


Figure 4-3: Trends in diabatic circulation strength at each level calculated from the three reanalysis data products and from the WACCM model. Trends are only shown where they are significant at the 95% confidence level, which means that there are no trends in the WACCM model run.

free running model, the variations in the lower branch of the circulation and in the upper branch are anticorrelated. Based on intuition about the residual circulation, it seemed that this correlation could be associated with the quasibiennial oscillation (QBO). Figure 4-5 shows the deseasonalized time series of the overturning circulation strength at 500 K and the negative of the deseasonalized time series of overturning circulation strength at 900 K, where the anticorrelation is strongest. The visual correlation between the two is indeed dominated by longer timescales, but the shorter term variability is correlated as well. When we calculate a frequency dependent correlation, there is a statistically significant correlation at all frequencies (not shown).

We have not yet fully explored the reasons for this anticorrelation. One explanation would be the following: if the lower stratospheric circulation is stronger, that implies more wave activity from below, and if the planetary scale waves are larger in amplitude they will break lower down. Thus, when there is more total wave activity, less of it reaches the altitudes at which it would drive the upper branch of the circulation. We will test this mechanism by performing a wavenumber decomposition and determining whether higher total wave activity especially in the higher wavenumbers is correlated with larger magnitudes of the lowest wavenumbers and lower breaking levels for these.

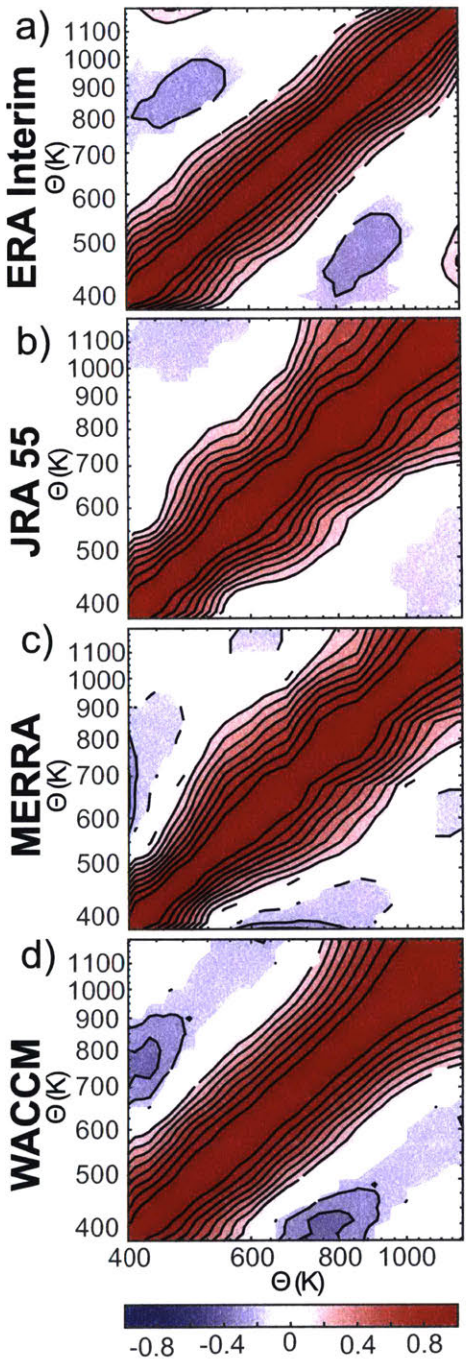


Figure 4-4: The spatial autocorrelation of the total diabatic overturning circulation strength from (a) ERA-Interim, (b) JRA55, (c) MERRA, and (d) WACCM. Correlations are only plotted where they are significant at the 95% confidence level, and the contour intervals are 0.1.

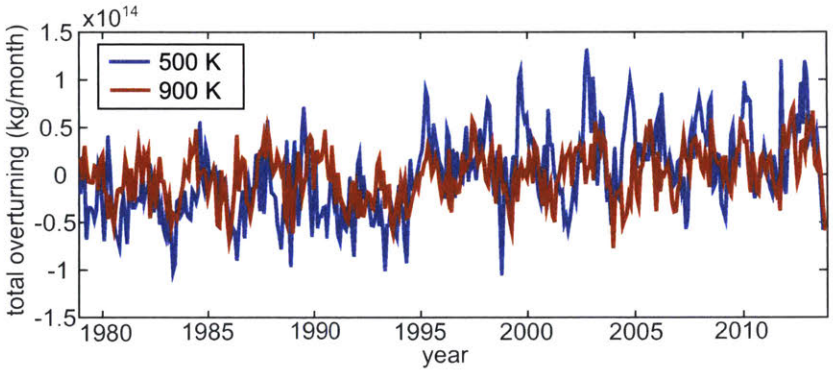


Figure 4-5: Time series of the deseasonalized overturning circulation strength from ERA-Interim at 500 K in blue and the negative of the overturning circulation strength from ERA-Interim at 900 K in orange.

## 4.4 The diabatic circulation's relationship with ozone

One of the primary motivations for studying the BDC and its variability is its influence on stratospheric ozone. The circulation is known to transport ozone—this is why Dobson proposed it in the first place (Dobson et al., 1929), even if he concluded that this circulation was far-fetched. While the qualitative description of the influence of the circulation on ozone is well established, with it transporting ozone from its primary production location in the middle stratosphere in the tropics to the midlatitudes and poles at lower altitudes, quantifying this effect is not simple. We know from observational studies that changes to the dynamics impact polar ozone (Hassler et al., 2011), and that the ozone hole recovery is currently being modulated by the dynamics (Solomon et al., 2016). In the Northern hemisphere, the variability in hemispherically averaged upward Eliassen-Palm (EP) flux at 100 hPa from a reanalysis data product has been shown to explain about 50% of the interannual variability of total column ozone in wintertime (Fusco and Salby, 1999) with the influence of the wave driving dependent on the latitude (Reinsel et al., 2005). These strong relationships are a motivating factor in using the TEM residual mean vertical velocity, which is directly related to the EP flux, as a metric for the BDC strength. The global diabatic overturning circulation on isentropes has been demonstrated to be related to tracer transport when considering the ideal tracer age of air. Now we want to assess the extent to which the diabatic circulation strength is related to stratospheric ozone variability.

The ideal age tracer is much simpler than ozone because it is conserved within the stratosphere and has a uniform source at the tropopause. Ozone, in contrast, is both produced and destroyed in the stratosphere in chemical processes that are photochemically and temperature dependent. The ozone maximum is around 7 hPa or 800 K in the tropics (e.g. Paul et al., 1998), where photolysis by wavelengths less than 240 nm dissociates molecular oxygen (Chapman, 1930; Seinfeld and Pandis, 2006). Stratospheric ozone absorbs ultraviolet radiation, creating heat, and thus it influences the thermal structure of the stratosphere (e.g. Andrews et al., 1987). The chemistry is temperature dependent, and therefore ozone, temperature and the circulation are closely connected.

With this interconnectivity in mind, we examine the total column ozone correlation at every latitude with the the global overturning circulation strength at each level within the stratosphere. The correlation of the deseasonalized timeseries of the monthly mean total column ozone data from the Solar Backscater Ultraviolet Instrument (SBUV) from 1980–2013 and the global diabatic circulation strength from the three different reanalyses is shown in Figure 4-6. Also shown is the correlation of the total column ozone and global diabatic circulation strength from the WACCM model. Generally, there is a consistent pattern across all three reanalyses and the model. The ERA-Interim correlation with the SBUV data is much stronger than the correlations of the other two reanalyses with the SBUV data. ERA-Interim assimilates the SBUV data, where MERRA and JRA55 do not, and this is a likely explanation for the increased correlation. Nevertheless, as the same spatial patterns are visible in the correlations with all three reanalyses, we consider the pattern to be robust. We will focus on the ERA-Interim and WACCM plots, as these two should have dynamics that are more consistent with the ozone.

We see that the high latitude total column ozone is correlated with the circulation in the lowermost stratosphere, with the correlation explaining up to 25% of the deseasonalized total column ozone variability in the Northern hemisphere polar region. The total column ozone in the tropics is strongly anticorrelated with the diabatic circulation at the level of the relative minimum in the circulation strength, 500 K. Both of these are qualitatively

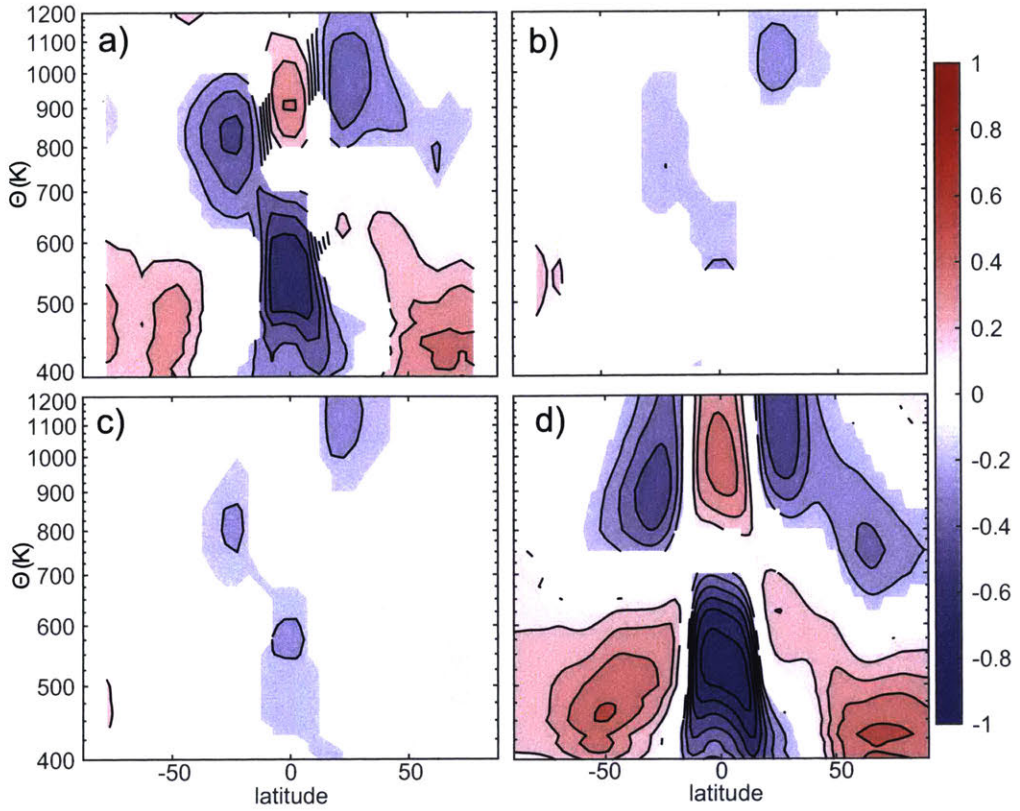


Figure 4-6: Correlation coefficient ($r$) of the interannual variability of total column ozone at every latitude to the total diabatic overturning circulation strength at every level for (a) ERA-Interim $\mathcal{M}$ and SBUV total column ozone, (b) JRA 55 $\mathcal{M}$ and SBUV total column ozone, (C) MERRA $\mathcal{M}$ and SBUV total column ozone and (d) ozone and $\mathcal{M}$ from WACCM.

consistent with transport being the dominant factor driving the relationship between the ozone and the circulation at these levels. The strong upwelling in the tropics brings up low ozone tropospheric air and is associated with strong downwelling in the extratropics, where the ozone is being transported from the tropics. The SBUV data do not exist at the poles, and so in order to understand the relationship between ozone and the diabatic circulation at the highest latitudes we look at WACCM. The correlation is strongest in the Southern hemisphere in the collar region of the polar vortex, around 55°S, and is weaker at the pole, while in the Northern hemisphere, the correlation is stronger poleward of that, around 70°N. This behavior is consistent with the diabatic circulation driving the correlation, as the polar vortex in the Southern hemisphere is stronger and creates stronger mixing barriers than the more disturbed Northern hemisphere vortex. The tropical total column ozone is also correlated with the circulation at upper levels, above the ozone maximum. Some of this correlation can be explained through the anticorrelation of the upper and lower branches of the circulation that we already identified. This is not enough to entirely explain the correlation, however. The subtropical total column ozone is anticorrelated with the upper level circulation strength, with hemispheric asymmetry in which levels relate to the

subtropical ozone in the different hemispheres. This pattern of the total column ozone correlation with the upper level circulation is not obviously transport related. Although upwelling through the ozone maximum is no longer drawing up low ozone air, stronger circulation still exports ozone to the poles.

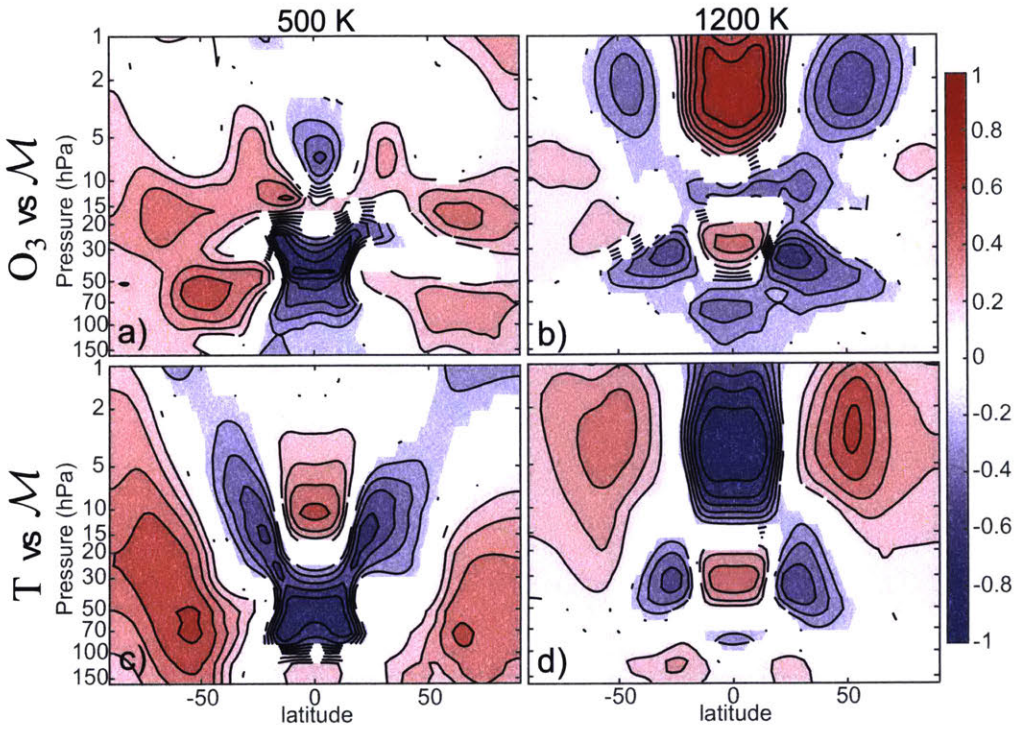


Figure 4-7: Correlation coefficient ($r$) of the interannual variability of local ozone concentration at every latitude and pressure to the total diabatic overturning circulation strength at (a) 500 K and (b) 1200 K from WACCM. Correlation coefficient ($r$) of the interannual variability of local temperatures at every latitude and pressure to the total diabatic overturning circulation strength at (a) 500 K and (b) 1200 K from WACCM. Contours are every 0.1, and correlations are only plotted where they are significant at the 95% confidence level.

To examine these correlations further, we plot the correlations of the deseasonalized ozone concentrations from WACCM and the deseasonalized total overturning circulation strength at a couple levels in Figure 4-7. In this way, we try to understand where in the stratosphere the total column ozone correlation patterns are determined. The top left panel shows the correlation of the deseasonalized local ozone concentration with the deseasonalized global overturning circulation strength at 500 K. The strong signal below the ozone maximum is consistent with the transport driving the ozone—upwelling ozone poor air from the troposphere and exporting the high ozone tropical air to the midlatitudes and poles in both hemispheres. The top right panel shows the correlation of the deseasonalized local ozone concentration with the global overturning circulation strength at 1200 K. At the equator at upper levels, the correlation is high, and the strong subtropical signal we see in Figure 4-6 is related to the variability of ozone at the uppermost levels and the local ozone concentration

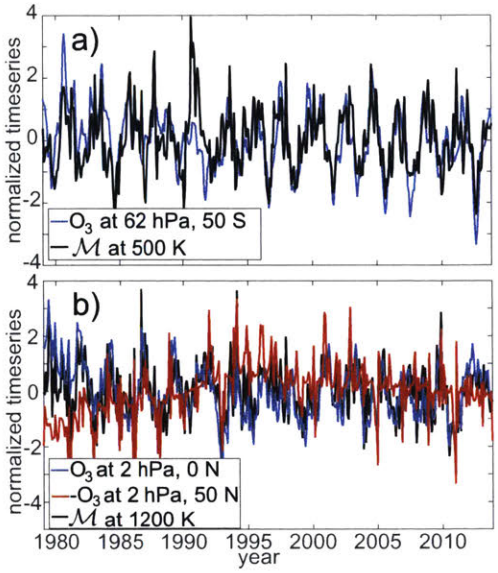


Figure 4-8: Timeseries of monthly mean local ozone concentration and the total overturning circulation strength from WACCM for (a) 62 hPa, 50° $O_3$ in blue and $\mathcal{M}$ at 500 K in black and (b) 2 hPa equatorial $O_3$ in blue, 2 hPa, 50° $O_3$ in red (multiplied by -1), and $\mathcal{M}$ in black.

on the edge of the tropics in the lower branch. We suggest that two different processes are responsible for these differing behaviors: The upper level local correlations are related to the temperature dependence of the ozone chemistry, and the middle stratosphere local correlations are related to the partitioning of the flow between the upper and lower branches of the circulation. At and above the ozone maximum, the ozone distribution is determined by chemistry, while at the lower levels the ozone distribution is determined by transport.

The correlation of the upper level circulation with the lower level ozone concentrations on the edges of the tropics is consistent with the anticorrelation of the upper and lower branches of the circulation and different characteristics of the transport. In the lower branch, the stratospheric entry levels are close to the poleward flanks of the tropics (Birner and Bönisch, 2011), and so if the anticorrelation of the upper and lower branches of the circulation is indeed a partitioning between the deep tropical entry latitudes and the more subtropical entry latitudes, the strong upper branch is associated with less upwelling in these flanks and thus less ozone around these turnaround latitudes.

Figure 4-8 shows time series of the local ozone concentrations and total overturning strength based on the maximum correlations shown in Figure 4-7. (a) shows the tight coupling between the ozone in the Southern hemisphere midlatitudes with the global overturning strength at 500 K. (b) shows the very close correlation of the upper level circulation and the upper level equatorial ozone and the weaker relationship with the upper level midlatitude ozone. The two timeseries in (a) and the equatorial ozone and global overturning in (b) are correlated at all timescales, while the anticorrelation is stronger at short timescales. Ozone variability at this level is dominated by photochemical processes (Perliski et al., 1989), and so we hypothesize that this close correlation is due to the relationship of temperature with

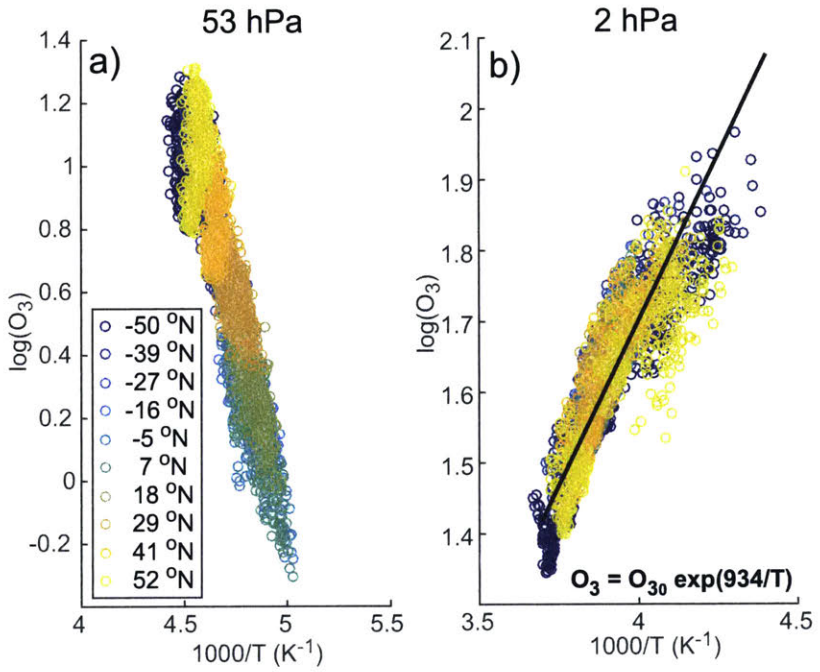


Figure 4-9: The natural log of the ozone concentrations (in ppm) and the colocated values of 1000/T for two different levels in the WACCM model including all of the years. a) is at 53 hPa and b) is at 2 hPa. Different colored circles are different latitudes, with the Northern Hemisphere being yellow and the Southern Hemisphere blue. In b), the best fit line is also plotted in black. The correlation coefficient for this fit was $r = 0.87$.

both ozone and the circulation strength. When the circulation is stronger in the tropics at these levels, that is associated with cooling and consequently more ozone production. We have therefore plotted the correlation of the temperature with the diabatic circulation at 500 K and 1200 K in Figure 4-7 (c) and (d). In both (c) and (d), it is evident that at low levels the temperature and ozone respond to the circulation similarly. In (d) in particular, the opposite relationship between the circulation and the temperature is observed to the circulation and the ozone, which indicates that the temperature is driving the chemistry. To test this mechanism, we have plotted the natural log of the ozone concentrations against the inverse of temperature at these upper levels and at lower levels. These results are shown in Figure 4-9. Clearly, the upper level and lower level are behaving differently: The lower level depends as much on latitude as on the inverse of temperature, with a negative slope, while the upper level has little latitudinal dependence and a positive slope that is therefore consistent with the form for many of the reaction rate coefficients for ozone loss processes (Stolarski et al., 2012). When the fit is calculated for the tropics separately, the slope is steeper and comparable to the Aura MLS data from Stolarski et al. (2012).

Stratospheric transport timescales for even the lower branch are around half a year to a year (Orbe et al., 2014), and so these instantaneous correlation plots might seem to be potentially less relevant. The integrated global overturning mass flux necessarily integrates over that transit time, however, as it accounts both for variability in the upwelling region and

in the downwelling region simultaneously. Therefore we do not perform lagged regressions to attempt to understand causality. Rather we suggest that the use of frequency dependent correlations, which will have a corresponding phase lag, will be necessary to look at the causal relationships (e.g. Swanson, 2000). However, as we can see from Figure 4-8, the correlations are in phase at monthly timescales, and so higher frequency records (minimum daily) will be necessary to diagnose the phase and the implied causality in these relationships.

Although the mechanistic relationship between ozone and the diabatic circulation requires more exploration, especially in the middle stratosphere, we have demonstrated the close dependence of ozone variability on the global diabatic circulation variability with data and with a model. The total column ozone at the poles and in the tropics is correlated with transport by the diabatic circulation in the lower stratosphere. The total column ozone in the subtropics is more tightly linked to the upper level circulation because of the temperature dependence of local photochemistry at upper levels and the partitioning of upwelling between the upper and lower branches.

## 4.5 Discussion and Conclusions

In this chapter, we have compared the diabatic overturning circulation strength through isentropic levels to the more traditionally used metrics for the strength of the BDC. We find that the three common methods for quantifying the BDC strength from models and reanalysis data products behave quite differently from each other for their deseasonalized variability, more differently than amongst the reanalyses. These three methods for calculating the TEM $\bar{w}^*$ are quite distinct, especially at lower levels where they are often analyzed. We suggest that using the diabatic overturning circulation strength through isentropic levels is an improvement over these, because it can be and has been constrained using tracer data. We find a very tight relationship between the tropical average TEM $\bar{w}^*_Q$ that is calculated using the total diabatic heating rates and the global overturning circulation strength on isentropes.

Like the thermodynamically constrained $\bar{w}^*$, which the global diabatic circulation so closely resembles, the global diabatic circulation strength is straightforward to calculate, requiring monthly mean heating rates, temperatures, and pressures. It also has an interesting property that the lower and upper branches of the circulation are anticorrelated, so that when the lower branch is stronger, less air is flowing through the upper branch. This is even more curious when one takes into account that the vertical velocity in the lower stratosphere is the sum of both branches. One explanation is that this could be due to higher amplitude planetary scale waves breaking lower in the stratosphere when there is more wave activity propagating upwards, but have yet to test this mechanism. Another possibility is that the meridional location of the wave breaking changes such that when the lower branch is stronger, less wave activity can propagate up into the upper stratosphere. Alternatively, there may be an interaction bewteen planetary and gravity waves. The anticorrelation is consistent with the conclusions of both Ray et al. (2010) and Stiller et al. (2012), who concluded based on observations that the trends in data were best explained by a strengthening in the lower branch of the circulation and a weakening in the middle and upper stratosphere.

We analyze the impact of the global diabatic circulation strength on total column ozone using satellite data and the three reanalyses, including examining the dependence of the total column ozone on different vertical levels of the circulation. When we find consistent behavior amongst the three reanalyses, we explore the mechanism using a model which

shows the same behavior. We examine the model in more detail, finding that the tropical ozone is most correlated with the overturning at 500–550 K, the Southern hemisphere ozone is sensitive to the overturning at around 480 K, and the Northern hemisphere ozone is most sensitive to the overturning at 400–450 K. The subtropics are most sensitive to the midlevel circulation at 800–1000 K, related to dominant role of chemistry at upper levels.

Based on its close relationship with one of the common metrics for the BDC, the ease of calculation, the demonstrated impact on ozone, and most importantly, the constraints provided by tracer observations, we present the global diabatic overturning circulation strength as a metric for the BDC that should be newly considered. Before the community settled on $\bar{w}^*$, the diabatic circulation was considered (Pyle and Rogers, 1980; Rosenfield et al., 1987). Although the community has developed some intuition for the behavior of $\bar{w}^*$, both Abalos et al. (2015) and this work have demonstrated that the variety of ways in which that is calculated are not equivalent. Thus, although some variety of TEM $\bar{w}^*$ is the most common metric at present, its calculation is not held in common amongst different studies. In order to understand models and reanalyses, consistency is critical. For the purposes of reanalysis evaluation, therefore, we advocate using the diabatic circulation along with a version of the quasigeostrophic TEM $\bar{w}^*$, since these rely on different assumptions, and the heating rates from reanalysis might be suspect. For the purposes of model evaluation, the global diabatic circulation should be sufficient.

Work is currently being done to understand the relationship of the global diabatic overturning strength on isentropes with the water vapor tape recorder, which will also then reveal how well this metric coincides with stratospheric water vapor.

# Chapter 5

# Stratospheric adiabatic mixing rates derived from the vertical age gradient

This chapter is a paper in preparation for Journal of Atmospheric Sciences: Marianna Linz, R. Alan Plumb, Edwin P. Gerber, and Douglas E. Kinnison: Stratospheric adiabatic mixing rates derived from the vertical age gradient. ML performed the research and wrote the manuscript, under the supervision of AP. EG provided the perpetual solstice model output. DK provided the WACCM output.

## 5.1 Introduction

The global stratospheric circulation is driven by breaking waves, which deposit momentum and drive circulation across surfaces of constant entropy and angular momentum. This circulation consists of two "branches", a deep branch associated with breaking of planetary scale waves in the middle and upper stratosphere, and a shallow branch associated with breaking waves just above the subtropical jet (Birner and Bönisch, 2011; McLandress and Shepherd, 2009). This wave breaking creates a net transport of air from the equator to the pole in the winter hemisphere, and from the equator to the midlatitudes in the summer hemisphere. It also causes turbulent, irreversible mixing (McIntyre and Palmer, 1984), sometimes referred to as "two-way mixing" because of the two-way mass exchange (Garny et al., 2014). In this study, we will work in isentropic coordinates, so the diabatic circulation will comprise our net meridional overturning circulation, and the "two-way mixing" will be the along-isentropic, quasi-horizontal mixing. The Brewer–Dobson circulation (BDC) is commonly used to refer to all of the above, that is, the mean mass transport within the stratosphere (Butchart, 2014). However, of late, generally focus has been on the zonal mean mass transport (e.g., Butchart et al., 2006; Garcia and Randel, 2008, and notably, Chapter 2). Mixing has been studied previously, primarily as a diffusivity: in a two-dimensional model by Newman et al. (1986), using effective diffusivity of Nakamura (1996) with observed winds by Haynes and Shuckburgh (2000) and by Allen and Nakamura (2001), and more recently in baroclinic flows by Leibensperger and Plumb (2014).

A number of recent studies have addressed the mixing from the perspective of tracer transport, almost all employing the ideal tracer age of air. Age of air is a measure of how long a parcel of air has been in the stratosphere (Hall and Plumb, 1994) and contains the average history of the trajectories of the bits of air that make up the parcel. Thus, it is extremely useful for quantifying transport and particularly mixing.

One method for understanding mixing that was developed recently is the calculation of "Aging by Mixing" (Garny et al., 2014; Ploeger et al., 2015a,b). This method is applicable to model studies in which the full residual circulation can be calculated and age of air has been modeled. The age of air output by the model is compared to the age that air would be if it were to simply follow the Tranformed Eulerian Mean residual circulation streamfunction, and the difference is surmised to be due to mixing. This approach yields a zonal mean structure of the "Aging by Mixing" as a function of latitude and vertical coordinate (pressure and potential temperature have both been used), which can be difficult to interpret, but clearly demonstrates that age of air is not a straightforward measure of the residual circulation (Garny et al., 2014). This method provides useful characterizations of model mixing. However, it relies on model calculations both for the age of air and for the trajectory analysis, and so it has little applicability to observations of trace gases. It also calculates the time-dependent residual circulation trajectories, which, while effectively eliminating the effects of zonal mixing, nevertheless will not necessarily remove effects of meridional mixing, and so the separation of the two components of the circulation is imperfect.

The other technique recently used to examine mixing adapts the Tropical Leaky Pipe (TLP) of Neu and Plumb (1999) (which served as the conceptual inspiration for Chapter 2) to look at mixing efficiency and recently to understand the impact of mixing on age (Ray et al., 2010, 2014, 2016; Moore et al., 2014). That model envisions a well-mixed tropical pipe and well-mixed extratropics with a constant vertical velocity in the tropics and a constant mixing efficiency between the two regions. It is formulated in height coordinates, which have the advantage of being physically intuitive. The adaptations of it have relaxed some of the

assumptions, allowing for vertical variations in the vertical velocity, and have incorporated multiple trace gases. The recent papers by Ray et al. (2014) and Ray et al. (2016) include running the TLP with Lagrangian forward particle trajectories to be able to examine the full age spectra and mixing. By using the TLP model to interpret both observational data and model results, these studies have made progress in understanding the mean mixing in the stratosphere.

This chapter serves to complete the reworking of the TLP model for age in isentropic coordinates in order to explicitly derive the relationship between age and adiabatic mixing. We develop a theory to calculate the mean adiabatic mixing at every level using the vertical gradient of age, thus improving upon the TLP model by considering vertical variations in mixing and in vertical velocity. We also look at differences between hemispheres, examining the assumptions necessary for the theory to apply. In Section 5.2, we develop the theoretical relationship between this vertical gradient of age and the mixing between the tropics and extratropics. We look at both symmetric and hemispherically asymmetric formulations and isolate the mean adiabatic age transport from the eddy adiabatic mixing. In Section 5.3 we apply the theory to a range of simulations with an idealized atmospheric model, demonstrating how the vertical age gradient relates to the the differing transport behaviors of these simulations. Section 5.3 also includes the exploration of changing amounts of hemispheric asymmetry and when the steady state theory for the vertical age gradient can be applied. Applications and limitations of the theory are discussed in Section 5.5.

## 5.2 Theory

In Chapter 2 Section 2.2.1, we demonstrated that the horizontal gradient of age on an isentrope is related to the diabatic circulation in steady state and neglecting diabatic diffusion. We refer the reader to 2.2.1 to review this derivation, which will not be repeated here. In what follows, we demonstrate that that the vertical (cross-isentropic) gradient of age is related to the adiabatic circulation under the same conditions.

### 5.2.1 Vertical tropical age gradient

The derivation for the relationship between the diabatic circulation and the age of air was performed by considering the global integration of the ideal age equation above an isentrope. Now we consider the tropical region only in order to gain insight into the mixing between the tropics and extratropics. Age is considered to be well-mixed in tropics and in the extratropics, and diabatic diffusion is neglected. The "tropics" will be used to refer to the region where air is upwelling through an isentrope, and the "extratropics" where air is downwelling.

Start once more, as in Chapter 2, with the ideal age equation (Waugh and Hall, 2002), which states that the total derivative of age is equal to a source of 1 (year/year):

$$\frac{\partial \Gamma}{\partial t} + \mathscr{L}(\Gamma) = 1, \tag{5.1}$$

where $\Gamma$ is the age and $\mathscr{L}$ is the advection–diffusion operator, with a boundary condition of zero at the tropopause.

We neglect diabatic diffusion and assume steady state. Then we integrate this equation over the volume above only the upwelling region on an isentrope, as opposed to the whole

surface, using the divergence theorem to take into account not only the bottom boundary, but also the boundaries with the extratropics:

$$\int_{up} \mathbf{n} \cdot \mathbf{F}^{\Gamma} dA - \int \oint \sigma V_{in} \Gamma dl d\theta + \int \oint \sigma V_{out} \Gamma dl d\theta = \int_{\mathcal{V}_{up}} \sigma dA d\theta = \int_{\mathcal{V}_{up}} \rho dV. \tag{5.2}$$

Then take the vertical derivative in entropy to obtain

$$\frac{\partial}{\partial \theta} \int_{up} \sigma \dot{\theta} \Gamma dA - \oint \sigma V_{in} \Gamma dl + \oint \sigma V_{out} \Gamma dl = \int_{up} \sigma dA. \tag{5.3}$$

Like Neu and Plumb (1999), we make the simplifying assumption that the air coming into the tropics has the average age of the extratropical region ($\Gamma_d$), and likewise the air leaving the tropics has the average age of the tropical region ($\Gamma_u$), although the definitions here are mass-flux-weighted. Hemispheric symmetry is implied because both tropical boundaries are treated together, although we will relax that assumption. Define the entrainment and detrainment mass fluxes $\mu_{in}$ and $\mu_{out}$ (units of mass per unit theta per unit time) as follows:

$$\mu_{in} = \oint \sigma V_{in} dl, \tag{5.4}$$

and

$$\mu_{out} = \oint \sigma V_{out} dl. \tag{5.5}$$

Then rewrite the integral of the density as $\Sigma_u = \int_{up} \sigma dA$. With these notation changes and simplifications, we can rewrite (5.3) as:

$$\frac{\partial}{\partial \theta} \int_{up} \sigma \dot{\theta} \Gamma dA + \mu_{out} \Gamma_u - \mu_{in} \Gamma_d = \Sigma_u. \tag{5.6}$$

Then, the change in the diabatic circulation with entropy is due to the difference between the entrainment and detrainment mass fluxes:

$$\frac{\partial \mathcal{M}}{\partial \theta} = \mu_{in} - \mu_{out} = \frac{\partial}{\partial \theta} \int_{up} \sigma \dot{\theta} dA. \tag{5.7}$$

We rewrite (5.6) in terms of $\mathcal{M}$ and $\Gamma_u$:

$$\frac{\partial}{\partial \theta} \mathcal{M} \Gamma_u + \mu_{out} \Gamma_u - \mu_{in} \Gamma_d = \Sigma_u, \tag{5.8}$$

and with (5.7), this becomes

$$\mathcal{M} \frac{\partial \Gamma_u}{\partial \theta} = \Sigma_u + \mu_{in} \Delta \Gamma. \tag{5.9}$$

The right hand side of this equation includes the two different terms that cause an increase in age in the vertical: $\Sigma_u$, which is the mass-weighted rate at which the air ages along the diabatic circulation, and $\mu_{in} \Delta \Gamma$, which is the rate at which adiabatic mixing between the tropics and extratropics increases the age of air. The mixing rate thus defined is $\mu_{in} / \Sigma_u$. Apart from $\mu_{in}$, all of the terms in (5.9) can be easily diagnosed.

The mixing timescale derived in this way is closely related to previous work, such as that by Garny et al. (2014) or Neu and Plumb (1999). With the formulation of this theory

in isentropic coordinates, the mean entrainment mass flux, $\mu_{in}$ is necessarily the adiabatic contribution, and our treatment has avoided the assumptions of constant mixing efficiency and vertical velocity with height. Furthermore, subject to caveats about mass-flux-weighting as opposed to area-weighting, this enables a direct estimation of the adiabatic mixing from age of air data. The steady-state assumption is necessary for this result to apply, however, and so long data records will be required to perform this calculation.

### 5.2.2 Separation of mean advective and eddy components

The mean detrainment mass flux out of the tropics is proportional the eddy component of the mixing as we will now demonstrate.

Start with the zonal mean, steady-state, isentropic flux form of the tracer continuity equation, with age as the tracer:

$$\overline{(\sigma v \Gamma)_y} + \overline{(\sigma \dot{\theta} \Gamma)_\theta} = \overline{\sigma}, \tag{5.10}$$

where $v$ is the meridional velocity, and the bar indicates a zonal mean. Integrate this over the extratropics from each pole to the latitudes where $\bar{\dot{\theta}} = 0$, which will be called $TL$. Then the first term is the amount of age leaving/entering through the meridional boundary, and can be written as:

$$\left[\overline{\sigma v \Gamma}\right]_{TL} = \mu_{out}\Gamma_u - \mu_{in}\Gamma_d. \tag{5.11}$$

There is some subtlety in this equation, as the boundary $TL$ is approached from opposite sides when performing the integral in the different hemispheres. $v$, is therefore defined to be positive if if is going away from the equator, rather than the typical positive northwards treatment. This will be true throughout this section. Additionally, because of the zonal mean, $\mu_{in}$ and $\mu_{out}$ are slightly different from those in (5.4) and (5.5) since in that derivation they are defined with a meridionally-varying turnaround latitude. However, since the meridional variations in turnaround latitude are small (primarily associated with the location of the asian monsoon), this should be largely equivalent.

We can divide this advection into the mean and the eddy component:

$$\left[\overline{\sigma v \Gamma}\right]_{TL} = \left[\bar{\sigma}\overline{v\Gamma}^*\right]_{TL} = \left[\bar{\sigma}\bar{v}^*\bar{\Gamma}^*\right]_{TL} + \left[\bar{\sigma}\overline{\hat{v}\hat{\Gamma}}^*\right]_{TL}, \tag{5.12}$$

where the mass-weighted zonal mean of a field $A$ is defined

$$\bar{A}^* \equiv \frac{\overline{(\sigma A)}}{\bar{\sigma}}, \tag{5.13}$$

and the deviation from that mass-weighted zonal mean is designated by the hat: $v = \bar{v}^* + \hat{v}$. Using the zonal mean steady-state conservation of mass, we have:

$$\frac{\partial \overline{(\sigma\dot{\theta})}}{\partial \theta} + \frac{\partial \overline{(\sigma v)}}{\partial y} = 0, \tag{5.14}$$

which we can integrate over the global downwelling region to get

$$-\frac{\partial \mathcal{M}}{\partial \theta} + \overline{\sigma v}|_{TL} = 0. \tag{5.15}$$

We use (5.7) to relate this to the entrainment and detrainment mass fluxes:

$$\overline{\sigma v}|_{TL} = \mu_{in} - \mu_{out}. \tag{5.16}$$

Then we can rewrite the terms in (5.12) and (5.11), assuming the age is uniform over the extratropics:

$$\Gamma_d \left(\mu_{out} - \mu_{in}\right) + \left[\bar{\sigma}\overline{\hat{v}\hat{\Gamma}^*}\right]_{TL} = \mu_{out}\Gamma_u - \mu_{in}\Gamma_d \tag{5.17}$$

Define the "eddy" contribution

$$\mathcal{E}_d = \left[\bar{\sigma}\overline{\hat{v}\hat{\Gamma}^*}\right]_{TL}. \tag{5.18}$$

Then we have

$$\mathcal{E}_d = -\mu_{out}\Delta\Gamma. \tag{5.19}$$

Thus the eddy flux of age into the global extratropics is equal to the product of the mean detrainment mass flux and the age difference. The result from (5.9) can be used to calculate the global eddy contribution of the age flux. If other tracers can be assumed to mix proportionally to their gradients, this could be used to calculate the eddy flux of any sufficiently long-lived stratospheric tracer.

This separation between the eddy and the advective flux, while treating the problem globally, does not make the same assumption about hemispheric symmetry, as the meridional velocities are evaluated separately on each edge of the tropics. The resulting eddy mixing is an average over the entire tropical edge, both the north and south, and how this is different between the two hemispheres is of interest. The derivation in the previous section makes the assumption that the mixing is symmetric and that the extratropical age is also symmetric. We will now relax those assumptions and treat the two hemispheres separately.

### 5.2.3 Diabatic circulation in each hemisphere

Figure 5-1 shows schematically the separation of the two hemispheres with the adiabatic mixing in orange and the diabatic circulation shown in the purple and green arrows. The hemispheres are separated by a dynamical equator, which is the zero streamline of the steady state flow and does not need to be constant in the vertical. Using this zero streamline will ensure that the two hemispheres are closed systems. Two levels are shown, with the upwelling regions in purple and the downwelling regions in green. The dash-dot lines show the separation between the upwelling and downwelling regions, corresponding to the zero of the diabatic velocity. These also can vary in the vertical. The assumption about hemispheric symmetry that is necessary is that the mass-flux-weighted age of upwelling air in the two different hemispheres is equal, or close enough so that mixing across the zero streamline is negligible for the total age budget. This assumption is naturally met by the prior assumption of well-mixed tropics and means that any adiabatic mixing within the tropics has no impact on the assumption of two separate closed hemispheres.

If the hemispheres are closed systems, the theory described in Chapter 2 can be applied to each hemisphere. We briefly go through some consequences of this application. The total diabatic mass flux through an isentrope is now separated into Northern Hemisphere mass flux, $\mathcal{M}_\mathcal{N}$, and Southern Hemisphere mass flux, $\mathcal{M}_\mathcal{S}$:

$$\mathcal{M} = \mathcal{M}_\mathcal{N} + \mathcal{M}_\mathcal{S}. \tag{5.20}$$

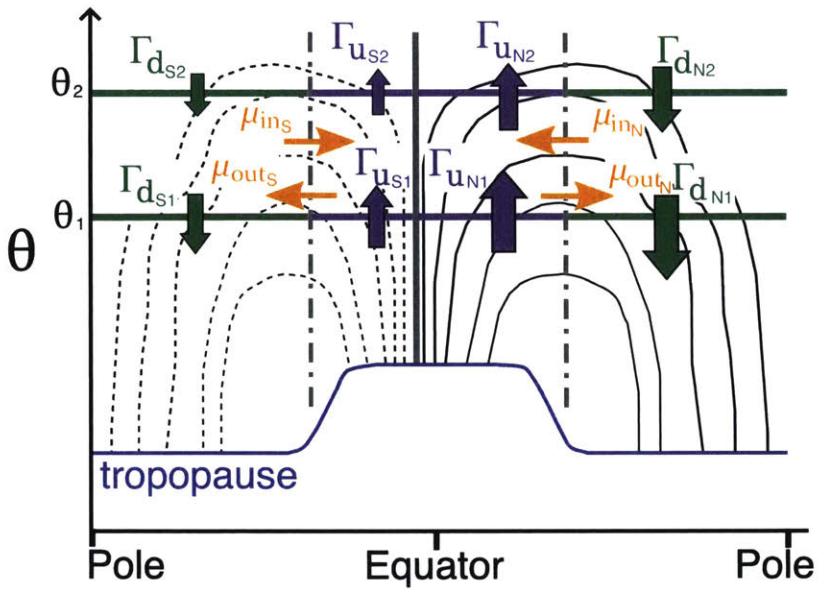


Figure 5-1: Schematic of the stratospheric circulation split into two "hemispheres" by a dynamical equator (dark gray solid line) corresponding to the zero streamline in the time mean of the circulation. Here the Northern Hemisphere is shown as having a greater meridional extent, consistent with reanalyses. Although this diagram shows the dynamical equator as vertical, in reality, it is tilted. Two separate isentropic levels are shown, with upwelling fluxes in purple and downwelling fluxes in green. The orange arrows are the mean entrainment and detrainment adiabatic mass fluxes between the extratropics and the tropics in each hemisphere. The black dotted and solid lines show the residual circulation streamlines. The dark gray dash-dot lines are the zero lines in the diabatic vertical velocity, $\dot{\theta}$, and like the dynamical equator, can have a varying latitude with height.

Similarly, the total mass above the isentropic surface in each hemisphere ($M_{\mathcal{N}}$ and $M_{\mathcal{S}}$) will be the total mass above the surface within the hemisphere, such that

$$M = M_{\mathcal{N}} + M_{\mathcal{S}}. \tag{5.21}$$

The age difference in each hemisphere is the difference between the mass-flux-weighted age of air downwelling through the isentrope in that hemisphere and the mass-flux-weighted age of upwelling air averaged between the $\dot{\theta} = 0$ line and the dynamic equator. Assuming no exchange between the two hemispheres or that the air exchanged in the tropics is of the same age, we have

$$\Delta\Gamma_{\mathcal{S}}\mathcal{M}_{\mathcal{S}} = M_{\mathcal{S}} \tag{5.22}$$

and

$$\Delta\Gamma_{\mathcal{N}}\mathcal{M}_{\mathcal{N}} = M_{\mathcal{N}}. \tag{5.23}$$

### 5.2.4 Southern Hemisphere extratropical age budget

This derivation is nearly identical to the global tropical case, but derived for the Southern Hemisphere extratropics. Qualitatively, consider that the downwelling and upwelling age of air in the Southern Hemisphere on the surface $\theta_2$ are known, along with the total mass above that surface. Then, using (5.22) we know the mass flux through the surface. In the absence of any advection into or out of the region, we can predict how old the air would be when it would arrive at the surface $\theta_1$, since we know the vertical velocity. This would imply a strictly decreasing vertical gradient of age with increasing $\theta$ in the extratropics. The difference between the age we predict and the true age will be due to the mean advection, which causes the mass flux through $\theta_1$ to be greater than that through $\theta_2$, and due to the mixing of young tropical air into the extratropics. Both of these processes contribute to $\mu_{in_S}$ and $\mu_{out_S}$.

For the derivation, start again with the ideal age equation (Waugh and Hall, 2002):

$$\frac{\partial \Gamma}{\partial t} + \mathscr{L}(\Gamma) = 1. \tag{5.24}$$

As before, we assume that diabatic diffusion is negligible and make the assumption of steady-state flow. Then we integrate this equation over the volume above the Southern Hemisphere downwelling region on an isentrope:

$$\int_{\mathcal{S}_{down}} \mathbf{n} \cdot \mathbf{F}^{\Gamma} dA - \int \oint \sigma V_{in} \Gamma dl d\theta + \int \oint \sigma V_{out} \Gamma dl d\theta = \int_{\mathcal{S}_{\mathcal{V}_{down}}} \sigma dA d\theta. \tag{5.25}$$

$dl$ is now only over the one surface that divides the Southern extratropics from the tropics, the Southern $\dot{\theta} = 0$ line. Then take the vertical derivative in entropy to obtain

$$\frac{\partial}{\partial \theta} \int_{\mathcal{S}_{down}} \sigma \dot{\theta} \Gamma dA - \oint \sigma V_{in} \Gamma dl + \oint \sigma V_{out} \Gamma dl = \int_{\mathcal{S}_{\mathcal{V}_{down}}} \sigma dA. \tag{5.26}$$

c.f. (5.3). The air coming into the extratropics is assumed to have the mass-flux-weighted average age of the tropical region ($\Gamma_{u_S}$), and likewise the air leaving the extratropics has the mass-flux-weighted average age of the Southern extratropical region ($\Gamma_{d_S}$). Define the entrainment and detrainment mass fluxes $\mu_{in_S}$ and $\mu_{out_S}$:

$$\mu_{in_S} = \oint \sigma V_{in} dl, \tag{5.27}$$

and

$$\mu_{out_S} = \oint \sigma V_{out} dl, \tag{5.28}$$

recalling that the line integral is now only across the Southern Hemisphere surface between the tropics and extratropics. Then rewrite the integral of the density as $\Sigma_{d_S} = \int_{S_{down}} \sigma dA$. With these notation changes and simplifications, we can rewrite (5.26) as:

$$\frac{\partial}{\partial \theta} \int_{\mathcal{S}_{up}} \sigma \dot{\theta} \Gamma dA - \mu_{out_S} \Gamma_{u_S} + \mu_{in_S} \Gamma_{d_S} = \Sigma_{d_S}. \tag{5.29}$$

As globally, the change in the Southern Hemisphere diabatic circulation with entropy is due

to the difference between the entrainment and detrainment mass fluxes:

$$\frac{\partial \mathcal{M}_\mathcal{S}}{\partial \theta} = \mu_{in_\mathcal{S}} - \mu_{out_\mathcal{S}} = \frac{\partial}{\partial \theta} \int_{\mathcal{S}_{up}} \sigma \dot{\theta} dA = -\frac{\partial}{\partial \theta} \int_{\mathcal{S}_{down}} \sigma \dot{\theta}. \tag{5.30}$$

We rewrite (5.29) in terms of $\mathcal{M}_\mathcal{S}$ and $\Gamma_{d_\mathcal{S}}$:

$$-\frac{\partial}{\partial \theta} \mathcal{M}_\mathcal{S} \Gamma_{d_\mathcal{S}} - \mu_{out_\mathcal{S}} \Gamma_{u_\mathcal{S}} + \mu_{in_\mathcal{S}} \Gamma_{d_\mathcal{S}} = \Sigma_{d_\mathcal{S}}, \tag{5.31}$$

and expanding the integral, this becomes

$$-\mathcal{M}_\mathcal{S} \frac{\partial \Gamma_{d_\mathcal{S}}}{\partial \theta} = \Sigma_{d_\mathcal{S}} - \mu_{out_\mathcal{S}} \Delta\Gamma_\mathcal{S}. \tag{5.32}$$

This states that as the air travels along the diabatic circulation downwelling in the extratropics, it is aging according to the mass-flux-weighted source, $\Sigma_{d_\mathcal{S}}$, and getting younger by the advection of young air from the tropics, $\mu_{out_\mathcal{S}} \Delta\Gamma_\mathcal{S}$. This result is equivalent to (5.9), except that it only considers the Southern Hemisphere.

The result for the Southern Hemisphere tropics is

$$\mathcal{M}_\mathcal{S} \frac{\partial \Gamma_{u_\mathcal{S}}}{\partial \theta} = \Sigma_{u_\mathcal{S}} + \mu_{in_\mathcal{S}} \Delta\Gamma_\mathcal{S}, \tag{5.33}$$

and both of these hold for the Northern Hemisphere as well. Thus, using only the age distribution, the mean entrainment and detrainment mass fluxes can be determined for both hemispheres.

## 5.3 Application in an idealized model

### 5.3.1 Model setup

To examine the utility of the theory, we calculate the mixing rates and diabatic circulation for the global mean and both hemispheres in a simple atmospheric GCM with a seasonal cycle and in perpetual Northern Hemisphere winter scenarios. We refer the reader to Section 2.3.1 for a description of the model set up.

We use wave–2 gaussian topography in the Northern Hemisphere as a wave–driver to mimic the planetary scale waves that are generated by flow over topography, land–sea contrast, and nonlinear interactions of synopic eddies. This topography is varied as specified in Table 5-1. The adiabatic lapse rate that sets the vortex strength, $\gamma$, also varies amongst the runs. The age tracer is specified as in Gerber (2012) and Chapter 2. The mean age and streamfunction for the idealized model runs are shown in Figure 5-2. The perpetually forced runs are an average over 1400 days after 10000 days of spin up. The seasonally-varying run is an average over 45 years after 20 years of spin up. The streamfunction is calculated by integrating the density weighted, area-weighted, diabatic vertical velocity from the south pole to the north pole and vice versa. Because the streamfunction is not exactly zero at the upper limit of integration for either integration (although close), a linear weighting is used to combine the two streamfunction integrations, such that at the poles, the streamfunction is forced to be zero. As age is zero at 700 hPa rather than at the tropopause and the tropospheric circulation is weak, the ages are about a year old at 400 K in the tropics.

The age is youngest in the two runs with strong forcing and strong vortices, (1 and 2),

| | time variation | $\gamma$ (K/km) | h (km) |
|---|---|---|---|
| 1 | perpetual solstice | 4 | 4 |
| 2 | perpetual solstice | 5 | 3 |
| 3 | perpetual solstice | 4 | 0 |
| 4 | perpetual solstice | 1.5 | 3 |
| 5 | seasonal | 4 | 4 |

Table 5-1: Summary of setup for the five idealized model runs. One run has a seasonal cycle as described in the text and the others have equilibrium temperature profiles that are constant in time. Four runs are perpetual–solstice with varying stratospheric lapse rates ($\gamma$, in K/km) and wavenumber–2 topographic forcing (h in km) in the Northern Hemisphere only. The winter hemisphere in these perpetual–solstice runs is the same as the hemisphere with topography.

and the Northern Hemisphere circulation is strongest in Run 2. The Southern Hemisphere circulation is strongest in the seasonally-varying run, consistent with the fact that there is a Southern Hemisphere winter circulation in that model. Of the perpetual solstice runs, the one with the weakest vortex has the strongest Southern Hemisphere circulation, representing an approach towards the equinox compared with Run 2 (which has the same topographical forcing). In runs with any topographical forcing, the air is oldest in the Southern Hemisphere. Where there is no topographic forcing (Run 3), however, the polar vortex in the Northern Hemisphere is isolated, as indicated by the extraordinarily large ages (up to 14 years) there.

Figure 5-3 shows the difference of each different run from Run 1, the climatology of which is shown in the upper left panel. In order to demonstrate the utility of our theory, we want to be able to explain the differences between the runs in terms of their overturning circulation strengths and mixing strengths. The difference between Run 1 and Run 2 is small, but changes character around 500 K. The lower stratosphere has a weaker Northern Hemispheric circulation and a stronger Southern Hemisphere circulation. The opposite is true higher up. The increased lapse rate means that it gets colder faster, driving stronger westerlies higher up. The decreased amount of wave driving means that this is not the only difference. The differences in age are small, with the upper branch showing a correspondingly younger extratropical air in the Northern Hemisphere and older air in the lower branch. These differences can be understood primarily in terms of changes to the diabatic circulation and the extratropical mixing to a lesser extent.

The difference between Run 3 and Run 1 is striking. The age in the polar vortex is much older in the run with no wave driving (Run 3), while there is also a much weaker circulation over all, except in the lower Southern Hemisphere. We will examine these differences in detail. The differences between Run 4 and Run 1 in the Northern Hemisphere and Run 5 and Run 1 are quite similar, as the weaker Northern Hemisphere vortex is closer to the seasonally averaged vortex strength.

### 5.3.2 Global mean diabatic circulation and adiabatic mixing

Having established the two dimensional picture of the climatology of these runs, we now try to understand their differences in diabatic circulation and adiabatic mixing and the corresponding age distributions. We use the global mean theory from Section 5.2.1, with

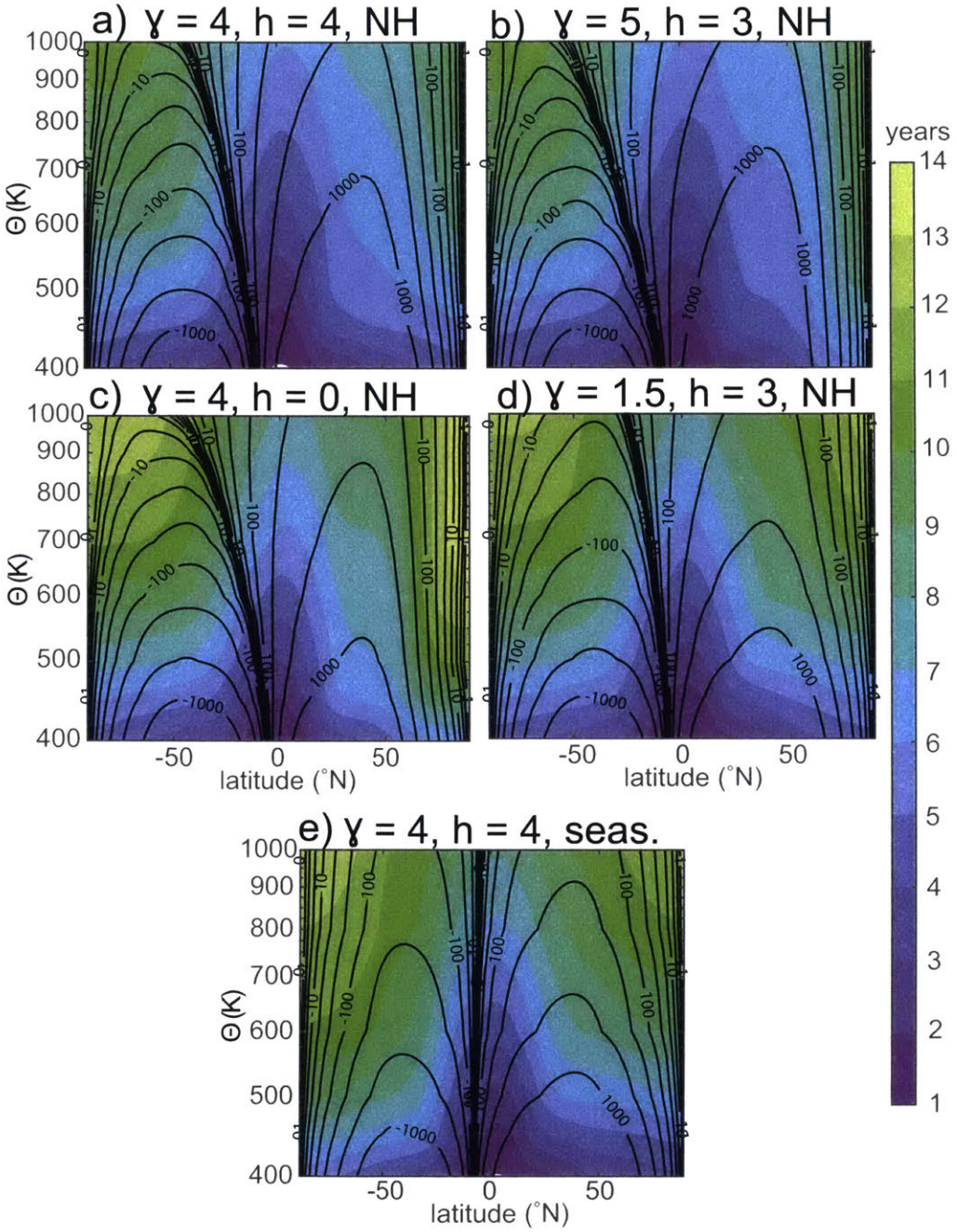


Figure 5-2: The mean age and mean streamfunctions in the idealized model used in this study. Contours are spaced logarithmically and have units of kg $m^{-1}$ $s^{-1}$. Age contours are spaced every year.

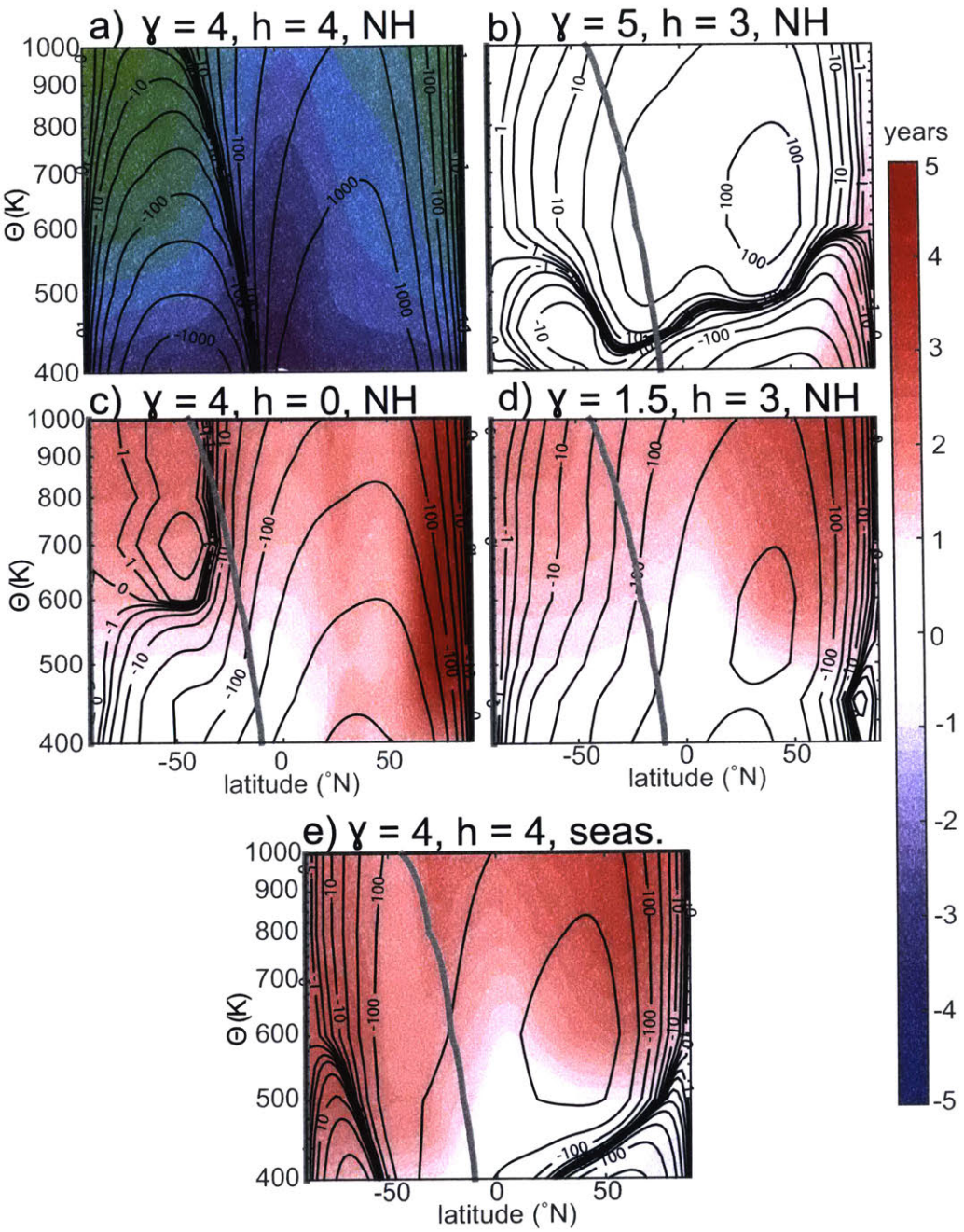


Figure 5-3: a) The mean age and mean streamfunction from Run 1 (identical to Figure 5-2 a, and with the same contours and age color bar). b)–e) The difference of the mean age and mean streamfunctions from Run 1 and the other four runs of the idealized model used in this study. Contours are spaced logarithmically and have units of kg $m^{-1}$ $s^{-1}$. Age contours are spaced every 0.25 years. The dark gray line is the mean dividing streamline in Run 1 for reference.

(5.9) and the equivalent extratropical expression:

$$-\mathcal{M}\frac{\partial \Gamma_d}{\partial \theta} = \Sigma_d - \mu_{out}\Delta\Gamma, \tag{5.34}$$

which can be derived in the same way as (5.32) except using global integrals.

Figure 5-4 shows the global mean $\Delta\Gamma$ and the gradients of age in the upwelling and downwelling regions, thus reflecting a large scale average description of the age field and, as we will show, the circulation. $\Delta\Gamma$ is overall lower for Runs 1 and 2, although all but Run 3 have similar age gradients at the lowermost levels. Generally, one can compare Figure 5-3 with Figure 5-4 a) to see that most variations in age gradients between the runs are reflected in the global mean metric, $\Delta\Gamma$. The exception is the behavior in the Northern Hemisphere midlatitudes, where visually the largest difference between Runs 1 and 2 exists at upper levels. Because of the mass-flux-weighting and the proximity of this to the turnaround latitudes, this difference appears dramatic in the 2-D picture but is small for the global mean age difference.

The vertical gradients of the mass-flux-weighted age in the upwelling and in the downwelling region are shown in Figure 5-4 b) and c). The tropical gradients are quite similar overall amongst the models, with the two "younger" runs (1 and 2) appearing nearly identical, and the two "older" runs and the seasonally-varying also agreeing rather closely. We will see that apart from the lowermost stratosphere, where there is more variation amongst the tropical age gradients for these runs, the tropical age gradient is driven by the diabatic component of the circulation. The extratropical age gradients vary more substantially between the model runs. The integrated extratropical age gradient is influenced almost entirely by the Northern Hemisphere, again because of the mass-flux-weighting. This can be seen in the close agreement of Runs 4 and 5 at the upper levels, even though Run 5 has considerably older air in the Southern Hemisphere polar region and therefore also a steeper gradient that is not reflected in this extratropical mean.

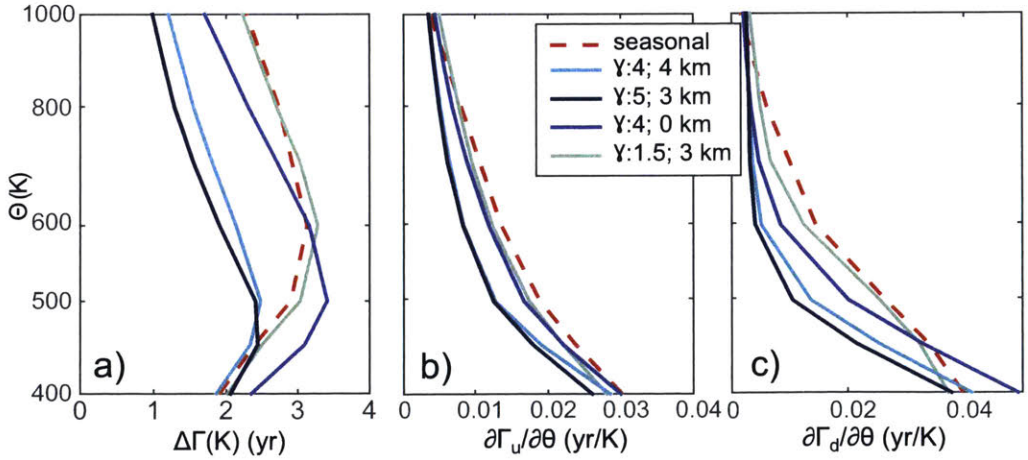


Figure 5-4: (a) The difference between the mass-flux-weighted age of downwelling air and upwelling air through each isentrope and (b) the vertical gradient in the mass-flux-weighted age of upwelling air and (c) downwelling air for the five model runs.

This qualitative comparison provides confidence that these large-scale averages of the

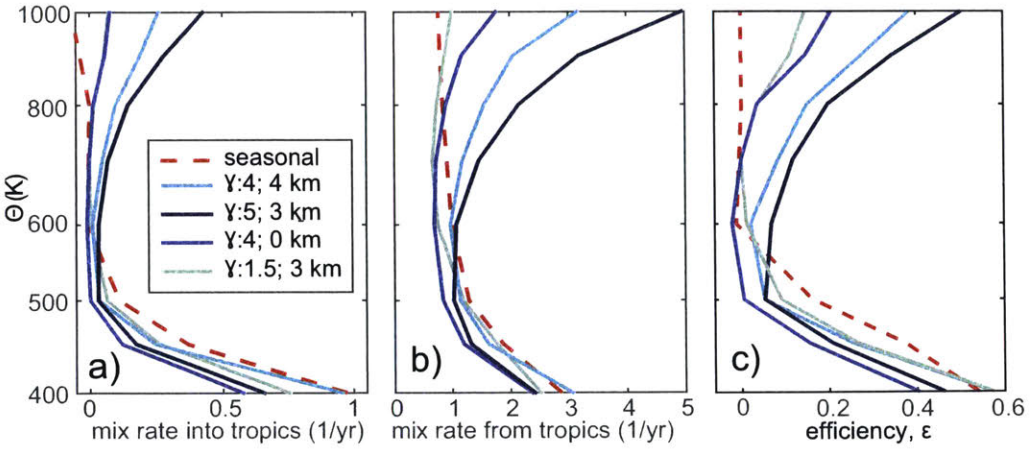


Figure 5-5: (a) Global average mixing rate into the tropics and (b) into the extratropics and (c) mixing efficiency from five different model runs.

mass-flux-weighted age of air largely capture the variation in age between these runs, and we now consider the circulation as revealed by these. To understand the diabatic circulation, consider (2.11) and Figure 5-4 a). The overturning strength is inversely proportional to the age difference, and so where the age difference is larger, the circulation is weaker. We see the strong circulation in Runs 1 and 2, and the weaker circulation in the other three runs. The local maximum in the profile towards the middle of the stratosphere is a local minimum in the velocity and can be thought of as a separation between the upper and lower branches of the circulation. The stronger lapse rates tend to drive this transition lower.

Without any mixing, the vertical gradient of age in the extratropics would be reversed from what we observe, as the air would follow the diabatic circulation pathway from aloft, continually getting older along that path. Thus, it is clear that adiabatic mixing is significant in setting the age distribution in the extratropics. Its role in the tropics is less clear. We solve equation 5.34 for the adiabatic rate of entrainment into the downwelling region:

$$\frac{\mu_{out}}{\Sigma_d} = \frac{\mathcal{M}}{\Sigma_d \Delta\Gamma}\frac{\partial \Gamma_d}{\partial \theta} + \frac{1}{\Delta\Gamma}, \tag{5.35}$$

and similarly express the adiabatic rate of entrainment into the upwelling region

$$\frac{\mu_{in}}{\Sigma_u} = \frac{\mathcal{M}}{\Sigma_u \Delta\Gamma}\frac{\partial \Gamma_u}{\partial \theta} - \frac{1}{\Delta\Gamma}. \tag{5.36}$$

These mixing rates are shown in Figure 5-5 a) and b).

The vertical gradient of downwelling age is nearly identical for the three runs with stronger lapse rates, Runs 1, 2, and 3, above 700 K. However, the diabatic circulation strength is not the same, as can be seen in Figure 5-3. The stronger diabatic circulation in Run 1 compared to Run 3 demonstrates the effect of the comparatively higher mixing rate. Although the strong diabatic circulation would cause the vertical gradient to weaken substantially, the strong mixing compensates, bringing in younger air from lower latitudes and making the vertical age gradients closer. This picture is consistent with the idea that wave breaking drives both the diabatic circulation and adiabatic mixing. They do not

necessarily wholly compensate, as evidenced by the fact that the age distributions are not identical for these different runs. The relationship is nonlinear, as can be seen by substituting (2.11) into (5.35):

$$\frac{\mu_{out}}{\Sigma_d} = \frac{\mathcal{M}^2}{\Sigma_d M}\frac{\partial \Gamma_d}{\partial \theta} + \frac{\mathcal{M}}{M}. \tag{5.37}$$

The quadratic relationship between the mixing rate and the circulation strength is a natural consequence of dependence of the the meridional age difference on the diabatic circulation strength. This relationship is evident when we examine both the tropics and extratropics for Runs 1 and 2 in Figure 5-5 in light of the gradients shown in Figure 5-4. The vertical gradients of these two runs do not differ much. However, the diabatic circulation strength (as implied by the inverse of $\Delta\Gamma$) is stronger in Run 2 in the upper stratosphere and weaker in Run 2 in the lower stratosphere. Correspondingly, the mixing rates are much larger for Run 2 than Run 1 in the upper stratosphere where the diabatic circulation of Run 2 is stronger. Conversely, in the lower stratosphere where the diabatic circulation of Run 2 is weaker, the mixing rates are smaller for Run 2 than for Run 1. In the Tropical Leaky Pipe (Neu and Plumb, 1999), the mixing efficiency, $\epsilon$, is used instead of the mixing rate. This is defined as the ratio of the entrainment mass flux into the tropics to the net detrainment into the extratropics. In our model, then, this is

$$\epsilon = \frac{\mu_{in}}{\mu_{out} - \mu_{in}} = \frac{\mu_{in}}{\partial \mathcal{M}/\partial \theta}. \tag{5.38}$$

The mixing efficiency, defined in this way, is shown in the third panel of Figure 5-5. With this definition, the dependence on $\mathcal{M}$ is muted, though the qualitative information from the mixing rates is the same. In particular, the tropics are quite isolated between 500-600 K, with stronger mixing lower down and higher up.

In the original TLP paper, both the vertical velocity and the mixing efficiency were treated as constant with height. Since then, the model has been used extensively and modified in various ways, but no formulation explicitly expresses the mixing efficiency or rate with height. The work by Ray et al. (2016) came the closest by iterating the TLP model and allowing the mixing timescale to vary with height in the iterations, fitting to data and a model to derive a profile of mixing timescales. The results are comparable to our idealized model timescales, though the minimum in mixing in the middle stratosphere is not nearly as weak in their results as here. However, the idealized model used in this study could certainly have too little variability and thus too little mixing, so the qualitative agreement between the two studies is encouraging. Our new treatment enables calculation of the adiabatic mixing and the diabatic circulation strength, including their vertical structures, from mean age alone. This is in constrast to the perceptions that age is insufficient to determine the stratospheric circulation (Ray et al., 2016; Moore et al., 2014).

### 5.3.3 Circulation in separate hemispheres

The Northern and Southern Hemispheres have very different behaviors in these runs, and it would be useful to be able to examine them separately. In particular, the Southern Hemisphere has no topography in any of these runs, so how much does the mixing rate vary amongst them? We will try to apply the theory from Section 5.2.4 to understand the differences.

In order to separate the two hemispheres, they must behave as two independent closed systems. Obviously, we expect there to be some amount of mixing within the tropics, and

so the assumption that is made to separate the two hemispheres is that the age of upwelling air is close enough in the two hemispheres that mixing across the zero streamfunction line is unimportant for the age budget. We can see from Figure 5-2 that this is unlikely to be the case for many of the runs here. Because of the asymmetry between the Northern and Southern Hemispheres, the age of air in the Southern Hemisphere upwelling region is considerably older than the age of air in the Northern Hemisphere upwelling region, especially as the Southern Hemisphere region extends further and further beyond the tropics, for example at upper levels in Runs 1 and 2. The circulation strength in the Southern Hemisphere is up to two orders of magnitude less than that in the Northern Hemisphere, and since the age difference is of mass-flux-weighted age, this leads to absurd apparent age differences for such small values of the circulation strength. For the more symmetric model configurations, we might expect this assumption to hold more reasonably. We can test how good this assumption is by calculating the relationship between the mass, age difference and mass flux, equations 5.22 and 5.23.

Figure 5-6 shows the mass to mass flux ratio versus the age difference calculated for the Northern Hemisphere, Southern Hemisphere and globally. The hemispheres are again defined by the dividing streamline. The theory is shown in the black line, and points that fall slightly above and along the line are those that are consistent with the theory given the neglect of diabatic diffusion (see Figure 2-6). It is evident that while the global theory holds very well, the hemispheric separation does not hold well in any of the simulations, with the exception perhaps of the seasonally-varying model run. In the Northern Hemisphere, the points fall well below the line at most levels, indicating that the age difference calculated by this method is greater than the age difference predicted for a truly closed system. As the Southern Hemisphere upwelling age of air is significantly older and is in fact mixing with the Northern Hemisphere air, this result is consistent with significant mixing across the zero streamline. Correspondingly, the points should fall above the line for the Southern Hemisphere plot, which they do. They are far above the line, in fact, because the circulation is so weak that the mass to mass flux ratio involves dividing by a very small number. By 1200 K in Run 2, there is no Southern Hemisphere circulation at all (not shown).

Because the separation of the hemispheres is perhaps valid for the seasonally-varying model run, we calculate the mixing rates based on (5.36) and (5.35) with the appropriate averaging regions for this run only. These results are shown in Figure 5-7. The Northern Hemisphere has stronger mixing, especially into the extratropics. The mixing into the tropics is more similar between the two hemispheres. Comparing the two dotted lines, the Northern Hemisphere behaves more like one of the strongly forced runs, while the Southern Hemisphere has weaker mixing, like Run 3, which has no topography. The mixing rates are overall weaker than the global mixng rates for the perpetual-solstice runs.

Thus we see that in the model run where the hemispheres can be approximately treated as individual closed systems, the mixing rate calculation yields reasonable results. It is not appropriate to apply the theory to the perpetual-solstice runs because the hemispheres clearly cannot be separated. We are in the process of exploring the degree of asymmetry that can be supported by the theory. It is possible that in the real world, the steady-state circulation is symmetric enough for the theory to apply. However, we cannot conclude that the hemispheric separation can be realistically applied without further study.

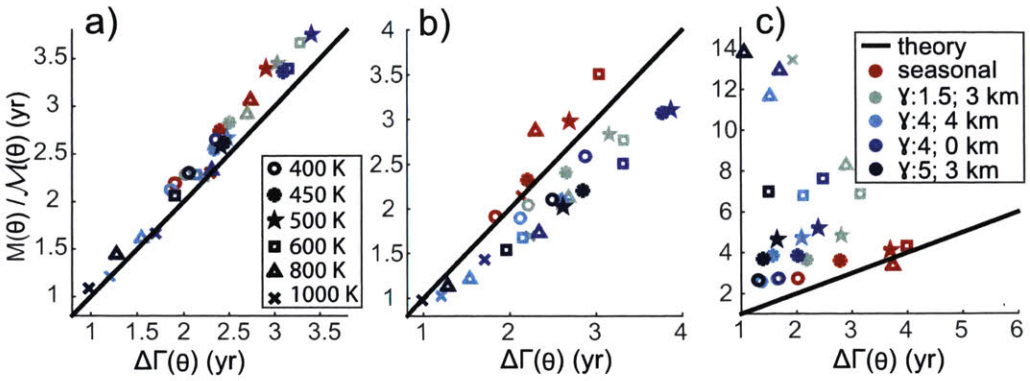


Figure 5-6: Scatter plots of the ratio mass above each isentrope to the mass flux through the isentrope against the difference in mass-flux-weighted age of downwelling and upwelling air. The relationship predicted by the theory is shown in the black one-to-one line. Different symbols show different isentropic levels, and different colors are the different model runs. The three panels show averaging over the following regions: (a) shows the global relationship, (b) shows the Northern Hemisphere only and (c) shows the Southern Hemisphere only. (a) and (b) are scaled to be square, while (c) is not.

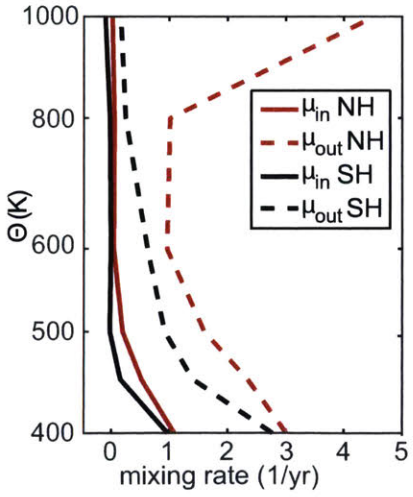


Figure 5-7: Mixing rates for Run 5, separated by hemisphere. The red lines are Northern Hemisphere and black lines are Southern Hemisphere. The dotted lines are the mixing into the extratropics, and the solid lines are the mixing into the tropics.

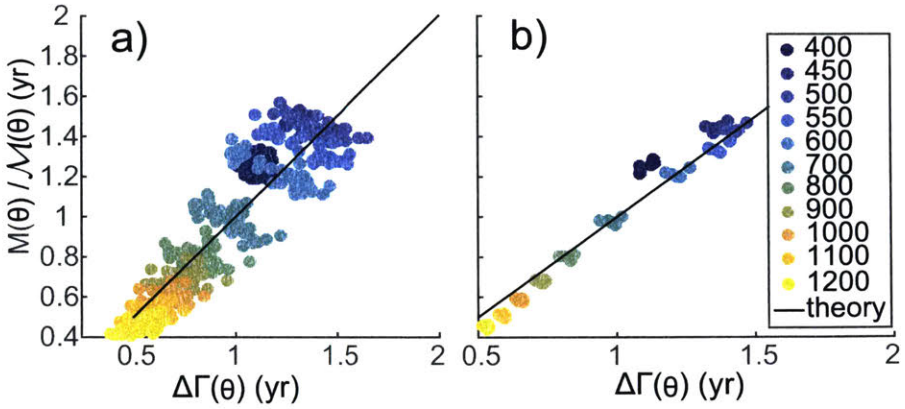


Figure 5-8: Scatter plots of the ratio mass above each isentrope to the mass flux through the isentrope against the difference in mass-flux-weighted age of downwelling and upwelling air for the WACCM model with (a) one year averages and (b) five year averages. The relationship predicted by the theory of Chapter 2 is shown in the black one-to-one line. Different colors show different isentropic levels.

## 5.4 Application in a realistic model

In order to get a better understanding of whether the hemispheric separation can be applied to the real atmosphere, we use the Whole Atmosphere Community Climate Model (WACCM). We apply the theory, both the global mean and the hemispherically separated, to the same model run of WACCM used in Chapters 3 and 4. First, we test (2.11) to see how well the steady-state age difference theory holds in this realistic model with different lengths of averaging. The results of this are shown in Figure 5-8, which shows scatter plots of the mass above each isentropic surface versus the difference between the mass flux weighted age of downwelling and upwelling air through each isentrope for one year averaging in the left panel and five year averaging in the right panel. For the idealized model, one year averaging was sufficient for the steady-state theory to apply (recall Figure 2-6). With a model that has more realistic interannual variability, five year averages reduce the spread so that the theory holds quite well. At the lower levels, the points fall above the one-to-one line predicted by the theory, which is again consistent with stronger diabatic diffusion in the lowermost stratosphere. At the upper levels, the points fall below the line, which we cannot explain currently. We are exploring whether this is related to model resolution or the interpolation from pressure to isentropes—otherwise, this is likely an indication of numerical diffusion.

When we separate the two hemispheres according to the theory in Section 5.2.4, we find that in this more realistic model, the theory holds much better than it did even in the seasonally varying idealized model, as can be seen in Figure 5-9, which is the same type of scatter plot as in Figure 5-8 but now colored by hemisphere rather than by isentropic level. Both the Northern and Southern Hemispheres have the same pattern of a local maximum in age difference in the middle stratosphere, and the points fall nearly along the line. The Southern Hemisphere is somewhat below the line, suggesting that the mixing of younger air from the Northern Hemisphere within the tropics might contribute to the age budget in a minor way, but the agreement with the theory is very good.

We calculate the horizontal age difference and cross-isentropic age gradients within the

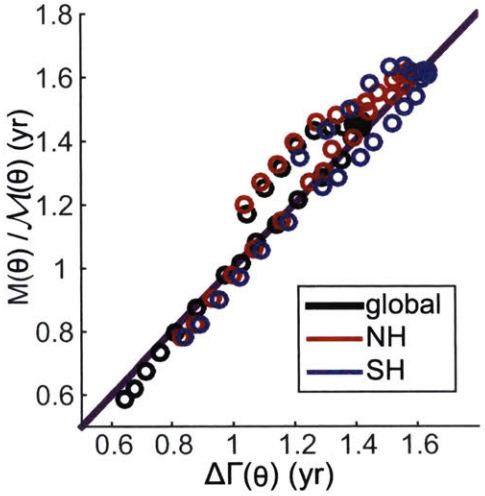


Figure 5-9: As in Figure 5-8, except now the global means are shown in the black circles, and the Northern Hemisphere and Southern Hemisphere, separated according to the theory in Section 5.2.4, in red and blue, respectively. The one-to-one line of the theory is in purple.

tropics and extratropics in order to calculate the mixing diagnostics for both hemispheres. The results are shown in 5-10. Examining first the age difference, shown in the left panel, we see that the Northern Hemisphere has a higher local maximum than the Southern Hemisphere, implying that the shallow branch of the Northern Hemisphere circulation has a larger vertical extent than the Southern Hemisphere. The age difference is also smaller in the lowermost stratosphere for the Northern Hemisphere, which suggests that the lower branch is relatively stronger compared to the upper branch in the Northern Hemisphere than in the Southern Hemisphere. The center and right panels show the vertical gradient of upwelling age of air and downwelling age of air. These are remarkably similar in the two hemispheres, and they thus match the global age gradient quite closely.

In order for the Northern Hemisphere downwelling age gradient to be the same as the Southern Hemisphere despite a stronger circulation, the mixing out of the tropics must also be greater, especially in the lower stratosphere. When we look at the mixing rates into and out of the tropics, shown in Figure 5-11, we see that this is indeed the case. All of these behaviors are consistent. Furthermore, we expect greater mixing in the lower stratosphere in the Northern Hemisphere than in the Southern Hemisphere because the Asian monsoon drives substantial mixing there.

We see that in the Southern Hemisphere, almost no air is mixed into the tropics above 600 K, and in the Northern Hemisphere, this isolation is a bit higher, about 650 K. Mixing into the extratropics has a local minimum at 600 K, which is above the local minimum in the diabatic velocities. The noise in the profiles is in large part due to the imperfect separation. The separation latitude was determined for each level separately, and so the coarse horizontal resolution means that there are jumps. To somewhat minimize these, we determine the "best" dynamical equator latitude by integrating from the North pole to the equator until and from the South pole to the equator until the latitude we come as close to zero as possible. Where the two integrations overlap, that latititude is assigned to be half in the Northern and half in the Southern hemisphere. A more rigorous treatment or a finer

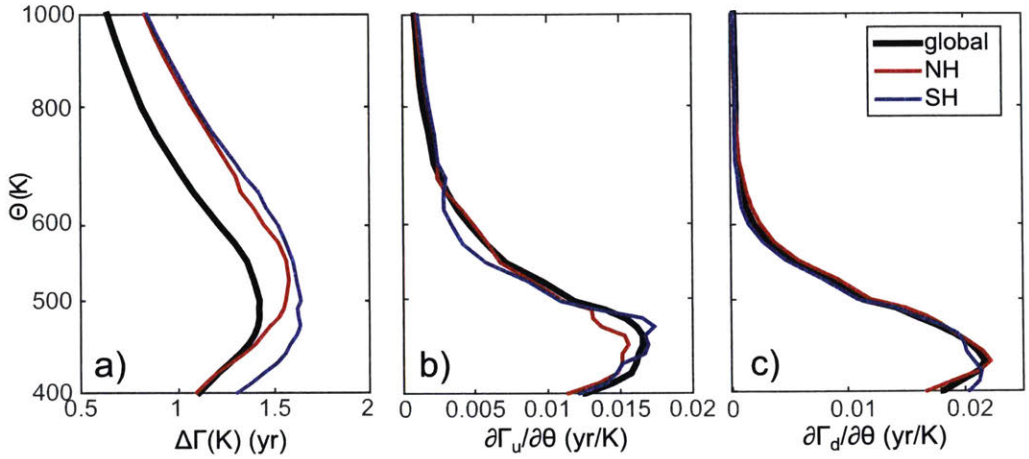


Figure 5-10: Relevant age gradients for calculating the mixing rates: a) The difference between mass-flux-weighted upwelling and downwelling age of air, b) the vertical gradient of mass-flux-weighted upwelling age of air, and c) the vertical gradient of mass-flux-weighted downwelling age of air. The global calculation is shown in the black, the Northern Hemisphere in the red, and the Southern Hemisphere in the blue.

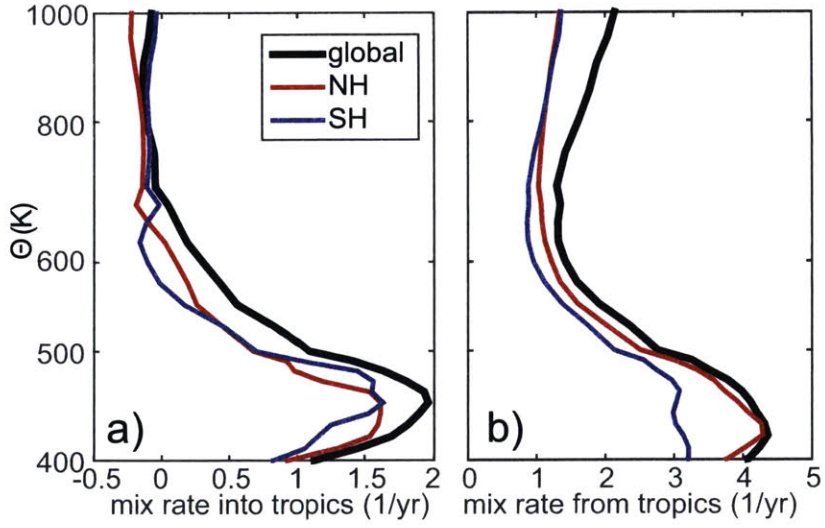


Figure 5-11: Mixing rate into and out of the tropics for the two hemispheres and the global average for WACCM.

resolution would likely smooth out the profiles further. The global results are qualitatively similar to the global results from Ray et al. (2016) for the Canadian Middle Atmosphere Model, although quantitative comparisons are difficult because of the different coordinate system and assumptions in that study.

## 5.5 Discussion and Conclusions

We have derived a method to determine the mixing rate between the tropics and extratropics from the age of air distribution, in steady state and assuming diabatic diffusion is small. We have transformed the Tropical Leaky Pipe framework of Neu and Plumb (1999) into isentropic coordinates. By formulating the theory on isentropic levels, we allow for both the diabatic velocities and the mixing efficiency to vary in the vertical. The vertical gradient of age of air in the extratropics informs of the mean detrainment rate out of the tropics, and the vertical gradient of age of air in the tropics informs the mean entrainment rate into the tropics. Taking advantage of the theory in Chapter 2, we can use the quasihorizontal gradients of age to calculate the diabatic circulation strength. With observations of age, temperature and pressure, we can calculate both a tropical entrainment and detrainment rate. Stratospheric age of air alone is sufficient to quantitatively determine the circulation as defined by these global or hemispheric averages and in steady-state. We note that unlike the theory of Chapter 2, this age metric is a diagnostic tool that reflects the assumptions we have made about the system (for example, that the average age of air that mixes from the extratropics into the tropics is the mass-flux-weighted mean age of downwelling air). However, these assumptions are necessary to develop the theory to relate mixing to age observations, and we believe this will be useful.

In applying this theory to an idealized model, we have seen the relationship between the adiabatic mixing and the diabatic circulation in setting the overall age distribution in the stratosphere. In order to maintain a positive vertical gradient of age in the extratropics, when the circulation is stronger, the mixing is also stronger. This relationship makes sense; increased wave breaking causes both stronger diabatic overturning and more adiabatic mixing, and we showed that the mixing rate has a quadratic dependence on the diabatic overturning strength.

This method is limited because of the steady-state assumption. In Chapter 2, we showed that in an idealized model, annual averages were generally sufficient for the steady-state assumption to hold for the relationship bewteen the diabatic circulation strength and the age difference between downwelling and upwelling air. In a more realistic model, five years is better, and is what we used in Chapter 3. Because mixing timescales tend to be shorter than the diabatic circulation timescales, it seems likely that the minimum period of averaging for the steady-state assumption to apply would be limited by the diabatic component. However, this is not straightforward to test—a comparison to the more traditional effective diffusivity analysis in a realistic model would be a first step. The steady-state assumption also necessarily makes this theory inappropriate for examining short term changes to the circulation. Instead, it is more appropriate for characterizing and comparing model mean circulation to the mean circulation of the true atmosphere and the decadal variations in these.

Many stratospheric processes, such as ozone depletion and recovery, affect the hemispheres asymmetrically, and so the global-average picture presented by this framework is lacking. We derived the relationships for the hemispheres separately; however, to do so,

we assumed that the two hemispheres act as independent closed systems, which we demonstrated is not the case for the perpetual solstice idealized model runs. In the idealized run with a seasonal cycle, this assumption is better, and we calculated the mixing rates for the hemispheres separately. These mixing rates were consistent with what could be expected based on the different forcing in the Northern and Southern Hemispheres, and so we conclude that this approach might be viable, though more work is necessary to understand the limitations.

When we apply the theory to a realistic model, we see that treating the hemispheres separately leads to little error, and so we can calculate the circulation strength and the mixing rates for each hemisphere. We find that the lower branch of the circulation in the Northern Hemisphere is relatively stronger as compared to the upper branch than in the Southern Hemisphere. We also see that the Northern Hemisphere extratropical mixing is greater than the Southern Hemisphere extratropical mixing in the lower stratosphere. Globally we find a relative minimum in mixing around 600 K, indicating complete isolation of the tropics above this level.

This theory holds potential to enable calculations of the mean adiabatic mixing of the real stratosphere from age of air observations. Unfortunately, because it relies on the vertical gradients of age, observations of sulfur hexafluoride ($SF_6$) and other trace gases from satellites will be difficult to use. The geometry of satellite measurements results in horizontal and vertical smoothing. While the limb viewing instruments that are used to calculate the abundances of trace gases that can be converted to age have less vertical smoothing than nadir viewing instruments, they currently can obtain only about 3–4 independent pieces of information between 18 and 40 km (Stiller et al., 2008; Livesey et al., 2011). This could provide, at best, a gross picture of the vertical gradients. In order to validate models using this theory, then, it is necessary to apply the retrival algorithms to model output so as to compare like to like (e.g., Zhang et al., 2010). The vertical information provided by balloon measurements is better than that from satellites, but balloons have no horizontal information. Thus the application of this theory to observations in order to quantify the adiabatic mixing in the stratosphere will require a concerted effort to combine a wide variety of observational data products.

# Chapter 6

# Summary and Outlook

The circulation of the stratosphere came into focus as interest in the ozone hole prompted more detailed study of both the chemistry and physics of the stratosphere. The chemistry is largely considered a solved problem now, about 40 years after the original concern about anthropogenic emissions causing ozone depletion (Seinfeld and Pandis, 2006). The interaction of the chemistry and the transport is far from solved, however (Solomon et al., 2016), and the state-of-the-art products that attempt to represent the reality of the stratospheric circulation differ substantially from each other (Abalos et al., 2015). The circulation is important not only for ozone, but also for water vapor, which has significant climate effects (Dessler et al., 2013; Solomon et al., 2010).

Recent work on the stratospheric circulation has included the development of stratosphere-resolving global climate models, especially as the high-top models lead to improved weather prediction (Gerber et al., 2012). These stratosphere-resolving models have universally predicted an increase in the strength of the stratospheric circulation (Butchart et al., 2010), but observations of trace gas distributions have not revealed such a trend (Engel et al., 2009; Stiller et al., 2012). The comparison of model output and data has been limited by the uncertainties associated with using tracer data to constrain the state variables of the model output.

This thesis has contributed to addressing the limitations of comparing model output to tracer observations by deriving relationships that enable calculation of the stratospheric circulation strength, both the diabatic circulation and the adiabatic mixing, from observations of trace gases. Building upon the foundational work by Neu and Plumb (1999) and Plumb (1996), the theoretical advances in this thesis (Chapters 2 and 5) consider the tropics and the extratropics as separate, well-mixed boxes. There is diabatic upwelling in the tropics and downwelling in the extratropics, and the tropical box and extratropical box exchange mass through two-way mixing across the tropical barrier. In the new formulation presented here, we have used potential temperature as the vertical coordinate, which naturally separates the adiabatic and diabatic motions.

We demonstrated that the diabatic component of the circulation through an isentrope, the total overturning circulation that enters in the tropics and exits in the extratropics, is

proportional to the difference in the age of air in the downwelling region and the age of air in the upwelling region. This result is very similar to that shown by Neu and Plumb (1999), except for the natural isolation of the diabatic component by using isentropic coordinates. The result is also physically intuitive: the difference between the age of air that is upwelling an isentropic surface and the air that is downwelling through an isentropic surface is how long the air spent above the surface, or its residence time. That residence time is proportional to the mass flux through the surface. Then we derived a time-dependent version of this theory that accounts for changes in the circulation strength, and we showed that for an idealized model, annual averages are sufficient to neglect the time-dependent terms. The horizontal gradient of age thus informs us about the vertical motions; in Chapter 5, we derive a relationship between the vertical gradient of age and the horizontal motions, demonstrating that the mixing rate depends nonlinearly on the diabatic circulation strength. Both theoretical developments were accompanied by exploration in an idealized atmospheric model.

The theories developed in this thesis have provided the framework to quantify the mean global stratopsheric circulation, both diabatic and adiabatic, and its vertical structure from observations of age of air tracers. We have verified the diabatic circulation theory and applied the adiabatic mixing theory in models.

In addition to these theoretical advances, I have also applied the theory that relates age of air observations and the diabatic circulation strength to trace gas observations from two independent satellite data products in order to provide quantitative, observationally-based constraints on the strength of the stratospheric diabatic circulation. In applying this theory, I discovered problems with the current suite of reanalysis data products, revealing large differences in their mean diabatic circulation strength and showing that two of the three are inconsistent with observations. The application of the theory to satellite data revealed the woeful inadequacies of the satellite data record to track changes to the circulation strength, and even to calculate the mean of the circulation strength for the upper stratosphere. This demonstration of the utility of global measurements will help to quantify what is necessary for future earth-observing missions to measure trace gases to determine the stratospheric circulation strength.

The application of the diabatic circulation theory to data has provided the first constraint on the global stratospheric diabatic circulation and demonstrated the acute need for new trace gas data for quantification of the mean circulation strength at upper levels.

In Chapter 4, I explored the global diabatic circulation as a new metric for the Brewer Dobson Circulation by comparing it to other common metrics and explicitly calculating its relationship with ozone variability. I showed that it holds a very close correspondence with one of the common Transformed Eulerian Mean vertical velocity calculations, and that the three different methods for calculating the TEM vertical velocities are quite different. The correlation of the low level stratospheric circulation with the total column ozone in the midlatitudes is relatively high, with the variability in the circulation strength explaining over 10% of the variability in total column ozone. At upper levels, there is an interplay between transport and chemistry that is reflected in the relationship between the ozone

and the circulation. The upper and lower branches of the circulation are also shown to be anticorrelated.

The global diabatic circulation of the stratosphere is a superior metric for models and reanalyses to those currently used because it contains the same variability as one of the current metrics, is strongly correlated with ozone variability, and it has been constrained by data.

All together, this thesis suggests an alternative framework for thinking about the stratospheric circulation when considering tracers. Unlike the Transformed Eulerian Mean circulation, which is excellent for considering the dynamics of the system, the global circulation in isentropic coordinates is directly related to the distributions of long-lived trace gases. This enables novel contraints on the circulation using satellite observations of these trace gases, including $N_2O$ and $SF_6$. Not only do the current observations provide quantitative constraints on the circulation, the theoretical framework provides new science goals to inform future earth-observing missions, whether satellite, aircraft, balloon or otherwise.

In order to calculate the strength of the circulation, global data over at least five years is necessary. With the failure of the MIPAS instrument in 2012 and the fact that the ACE satellite is running long past its expected lifetime, the prospect for continuous limb measurements of $SF_6$ is poor. $N_2O$ will presumably continue to be observed, and so further characterizing the relationship between the two is essential for the continuity of the record. To my knowledge, no replacement for MIPAS or ACE is currently being built, and this means that our stratospheric age coverage will be very limited in the near future.

Ideally, a continuous record from satellites with infrared sensors in limb-viewing geometry would measure $SF_6$ and methane for the next several decades. This, combined with additional in situ measurements of $CO_2$, $N_2O$ and methane, would provide a quantitative record of how the circulation is changing in response to greenhouse gas forcing, utilizing the methods developed in this thesis. The in situ characterizations of the tracer-tracer relationships would serve to extend the record further back, enabling conversion of methane and $N_2O$ to age for the currently available satellite observations. In situ measurements, specifically profiles, will be necessary to accurately measure the vertical gradients of age. The relatively new AirCore technology (Karion et al., 2010), which samples the atmosphere in a way that is similar to a Niskin bottle in the ocean, could prove to be an unprecedented source of data if their launches become more common. The small volume of the samples has meant that the measurements are very noisy compared to whole air sampling, but with sufficient coverage, that noise would average out.

Because of the difficulty in interpreting trace gas observations, much of our current knowledge of the circulation of the stratosphere is based on atmospheric models. The models have predicted an increase in the strength of the BDC with global warming, but their mean states differ substantially, as we demonstrated for the reanalyses in Chapter 3. Our quantitative framework with which to validate models with data can provide confidence in stratospheric models and their predictions. It cannot be directly related to the specifics of the wave-driving however, and more work is necessary to understand the role of different wave forcing (gravity and planetary scale) in driving the circulation and changes to it. The trace gas diagnostics are not an appropriate tool for addressing this problem. The Google Loon project, which could be an Argo float equivalent, holds potential to give novel data if we can get the right instruments on the balloons. The semi-Lagrangian motion and high

density of local measurements could be useful for investigating the waves, as these balloons will have an algorithm to try to keep them as close to evenly separated as possible.

While the focus of the community has been on the trends in the circulation associated with greenhouse gases and the corresponding tropospheric warming and stratospheric cooling, the mean state of the stratospheric circulation is comparatively unknown. What is the mean state of the stratospheric circulation, and how is it dynamically determined, are questions to which there currently exist only qualitative answers. In conjunction with the existing stratospheric models, and our new theoretical framework, new trace gas data are essential to measure and monitor the stratospheric circulation and to answer these fundamental questions.

The theoretical framework developed in this thesis could have additional applications. The deviations from the one-to-one line could be related to numerical or real diffusion in a stratospheric model, and this is being worked on by my collaborator, Edwin Gerber. In the troposphere, the theory could be revised to be on moist isentropes; convection would make the assumption of no diabatic diffusion laughable, but perhaps as a gross measure of the effect of convection, the theory might be useful—the deviation from the one-to-one line would be an integrated measure of the diffusion across moist isentropes. In the ocean, another highly stratified fluid, the application of the theory could lead to new insights about the strength of the globally averaged diapycnal diffusion. In ocean models, diapycnal diffusion is typically imposed. The theory would need to be revised, however, to account for the lack of ideal age tracers available in the ocean. The long time scales of ocean circulation mean that there is no "clock" tracer; ratios of tracers would need to be explored. The idea of age difference as a residence time is universal; the complexity lies in determining the system, the coordinates, and the timescales for which examining the age difference is useful.

Because tracers can be measured directly, they provide a valuable resource for understanding geophysical fluid dynamics. This work is a transformative development for quantitatively relating measurements of tracers to the dynamical system.

# Bibliography


Abalos, M., B. Legras, F. Ploeger, and W. J. Randel, 2015: Evaluating the advective Brewer–Dobson circulation in three reanalyses for the period 1979–2012. *J. Geophys. Res.*, **120**, 7534–7554, doi:10.1002/2015JD023182.

Allen, D. R., and N. Nakamura, 2001: A seasonal climatology of effective diffusivity in the stratosphere. *J. Geophys. Res.: Atmos.*, **106 (D8)**, 7917–7935, doi:10.1029/2000JD900717.

Andrews, A. E., and Coauthors, 2001: Mean ages of stratospheric air derived from in situ observations of CO, CH4, and N2O. *J. Geophys. Res.*, **106**.

Andrews, D. G., J. R. Holton, and C. B. Leovy, 1987: *Middle Atmosphere Dynamics*. 2nd ed., Academic Press, San Diego, California.

Andrews, D. G., and M. E. McIntyre, 1976: Planetary Waves in Horizontal and Vertical Shear: The Generalized Eliassen-Palm Relation and the Mean Zonal Acceleration. *Journal of the Atmospheric Sciences*.

Austin, J., and F. Li, 2006: On the relationship between the strength of the Brewer-Dobson circulation and the age of stratospheric air. *Geophys. Res. Lett.*, **33 (17)**, L17 807, doi:10.1029/2006GL026867.

Baldwin, M. P., and T. J. Dunkerton, 1999: Propagation of the Arctic Oscillation from the stratosphere to the troposphere. *J. Geophys. Res.*, **104**, 937–946.

Birner, T., and H. Bönisch, 2011: Residual circulation trajectories and transit times into the extratropical lowermost stratosphere. *Atmos. Chem. Phys.*, **11 (2)**, 817–827, doi:10.5194/acp-11-817-2011.

Boering, K. A., S. C. Wofsy, B. C. Daube, H. R. Schneider, M. Loewenstein, J. R. Podolske, and T. J. Conway, 1996: Stratospheric Mean Ages and Transport Rates from Observations of Carbon Dioxide and Nitrous Oxide. *Science*.

Brewer, A. W., 1949: Evidence for a world circulation provided by measurements of helium and water vapour distribution in the stratosphere. *Q. J. R. Meteorol. Soc.*, **75**, 351–363, doi:10.1002/qj.49707532603.

Butchart, N., 2014: The Brewer-Dobson circulation. *Rev. Geophys.*, **52**, 157–184, doi:10.1002/2013RG000448.

Butchart, N., and Coauthors, 2006: Simulations of anthropogenic change in the strength of the Brewer–Dobson circulation. *Clim. Dyn.*, **27**, 727–741, doi:10.1007/s00382-006-0162-4.

Butchart, N., and Coauthors, 2010: Chemistry-Climate Model Simulations of Twenty-First Century Stratospheric Climate and Circulation Changes. *J. Climate*, **23 (20)**, 5349–5374, doi:10.1175/2010JCLI3404.1.

Butchart, N., and Coauthors, 2011: Multimodel climate and variability of the stratosphere. *J. Geophys. Res.*, **116 (D5)**, D05 102, doi:10.1029/2010JD014995.

Carlotti, M., B. M. Dinelli, G. Innocenti, and L. Palchetti, 2016: A strategy for the measurement of $CO_2$ distribution in the stratosphere. *Atmos. Meas.Tech.*, **9 (12)**, 5853–5867, doi:10.5194/amt-9-5853-2016.

Chapman, S., 1930: On ozone and atomic oxygen in the upper atmosphere. *Philos. Mag.*, **10**, 369–383.

Dee, D. P., and S. Uppala, 2009: Variational bias correction of satellite radiance data in the era-interim reanalysis. *Q. J. R. Meteorol. Soc.*, **135 (644)**, 1830–1841, doi:10.1002/qj.493.

Dee, D. P., and Coauthors, 2011: The era-interim reanalysis: configuration and performance of the data assimilation system. *Q. J. R. Meteorol. Soc.*, **137 (656)**, 553–597, doi:10.1002/qj.828.

Dessler, A. E., M. R. Schoeberl, T. Wang, S. M. Davis, and K. H. Rosenlof, 2013: Stratospheric water vapor feedback. *Proc. Nat. Acad. Sci.*, **110 (45)**, 18 087–18 091, doi: 10.1073/pnas.1310344110.

Diallo, M., B. Legras, and a. Chédin, 2012: Age of stratospheric air in the ERA-Interim. *Atmos. Chem. Phys.*, **12 (24)**, 12 133–12 154, doi:10.5194/acp-12-12133-2012.

Dobson, G. M. B., D. N. Harrison, and J. Lawrence, 1929: Measurements of the amount of ozone in the Earth's atmosphere and its relation to other geophysical conditions. *Proc. R. Soc., A*, **122**, 456–486.

Donner, L. J., and Coauthors, 2011: The Dynamical Core, Physical Parameterizations, and Basic Simulation Characteristics of the Atmospheric Component AM3 of the GFDL Global Coupled Model CM3. *J. Climate*, **24 (13)**, 3484–3519, doi:10.1175/2011JCLI3955.1.

Edmon, H. J., B. J. Hoskins, and M. E. McIntyre, 1980: Eliassen-palm cross sections for the troposphere. *J. Atmos. Sci.*, **37 (12)**, 2600–2616, doi:10.1175/1520-0469(1980)037<2600:EPCSFT>2.0.CO;2.

Engel, A., and Coauthors, 2009: Age of stratospheric air unchanged within uncertainties over the past 30 years. *Nature Geosci.*, **2**, 28–31, doi:10.1038/ngeo388.

Flury, T., D. L. Wu, and W. G. Read, 2013: Variability in the speed of the Brewer–Dobson circulation as observed by Aura/MLS. *Atmos. Chem. Phys.*, **13 (9)**, 4563–4575, doi:10.5194/acp-13-4563-2013.

Forster, P., and Coauthors, 2007: Changes in Atmospheric Constituents and in Radiative Forcing. *Climate Change 2007: The Physical Science Basis. Contribution of Working Group I to the Fourth Assessment Report of the Intergovernmental Panel on Climate Change*, S. Solomon, D. Qin, M. Manning, Z. Chen, M. Marquis, M. T. K.B. Averyt, and H. Miller, Eds., Cambridge University Press, New York, NY, USA, chap. 2.

Forster, P. M., and K. P. Shine, 1999: Stratospheric water vapour changes as a possible contributor to observed stratospheric cooling. *Geophys. Res. Lett.*, **26 (21)**, 3309–3312, doi:10.1029/1999GL010487.

Froidevaux, L., R. A. Fuller, A. Lambert, N. J. Livesey, P. F. Bernath, and K. A. Walker, 2013: GOZCARDS Source Data for Nitrous Oxide Monthly Zonal Averages on a Geodetic Latitude and Pressure Grid v1.01. NASA Goddard Earth Sciences Data and Information Services Center, URL `https://doi.org/10.5067/MEASURES/GOZCARDS/DATA3012`, doi:10.5067/MEASURES/GOZCARDS/DATA3012.

Fu, Q., P. Lin, S. Solomon, and D. L. Hartmann, 2015: Observational evidence of strengthening of the Brewer–Dobson circulation since 1980. *J. Geophys. Res.*, **120**, 10,214–10,228, doi:10.1002/ 2015JD023657.

Fueglistaler, S., B. Legras, A. Beljaars, J.-J. Morcrette, A. Simmons, A. M. Tompkins, and S. Uppala, 2009: The diabatic heat budget of the upper troposphere and lower/mid stratosphere in ECMWF reanalyses. *Q. J. R. Meteorol. Soc.*, **135 (638)**, 21–37, doi: 10.1002/qj.361.

Funke, B., and Coauthors, 2011: Composition changes after the "Halloween" solar proton event: the High Energy Particle Precipitation in the Atmosphere (HEPPA) model versus MIPAS data intercomparison study. *Atmos. Chem. Phys.*, **11 (17)**, 9089–9139, doi:10.5194/acp-11-9089-2011.

Funke, B., and Coauthors, 2017: HEPPA-II model–measurement intercomparison project: EPP indirect effects during the dynamically perturbed NH winter 2008–2009. *Atmos. Chem. and Phys.*, **17 (5)**, 3573–3604, doi:10.5194/acp-17-3573-2017.

Fusco, A. C., and M. L. Salby, 1999: Interannual variations of total ozone and their relationship to variations of planetary wave activity. *Journal of Climate*, **12 (6)**, 1619–1629, doi:10.1175/1520-0442(1999)012<1619:IVOTOA>2.0.CO;2.

Garcia, R. R., and W. J. Randel, 2008: Acceleration of the BrewerâĂŞDobson Circulation due to Increases in Greenhouse Gases. *J. Atmos. Sci.*, **65 (8)**, 2731–2739, doi: 10.1175/2008JAS2712.1.

Garcia, R. R., W. J. Randel, and D. E. Kinnison, 2011: On the Determination of Age of Air Trends from Atmospheric Trace Species. *J. Atmos. Sci.*, **68 (1)**, 139–154, doi: 10.1175/2010JAS3527.1.

Garcia, R. R., A. K. Smith, D. E. Kinnison, ï£¡lvaro de la Cï£¡mara, and D. J. Murphy, 2017: Modification of the Gravity Wave Parameterization in the Whole Atmosphere Community Climate Model: Motivation and Results. *J. Atmos. Sci.*, **74 (1)**, 275–291, doi:10.1175/JAS-D-16-0104.1.

Garny, H., T. Birner, H. Boenisch, and F. Bunzel, 2014: The effects of mixing on Age of Air. *J. Geophys. Res.*, **119**, 7015–7034, doi:10.1002/2013JD021417.

Garny, H., M. Dameris, W. Randel, G. E. Bodeker, and R. Deckert, 2011: Dynamically forced increase of tropical upwelling in the lower stratosphere. *Journal of the Atmospheric Sciences*, **68 (6)**, 1214–1233, doi:10.1175/2011JAS3701.1.

Gerber, E. P., 2012: Stratospheric versus Tropospheric Control of the Strength and Structure of the Brewer-Dobson Circulation. *J. Atmos. Sci.*, **69 (9)**, 2857–2877, doi:10.1175/JAS-D-11-0341.1.

Gerber, E. P., and L. M. Polvani, 2009: Stratosphere–Troposphere Coupling in a Relatively Simple AGCM: The Importance of Stratospheric Variability. *J. Climate*, **22 (8)**, 1920–1933, doi:10.1175/2008JCLI2548.1.

Gerber, E. P., and Coauthors, 2012: Assessing and Understanding the Impact of Stratospheric Dynamics and Variability on the Earth System. *Bull. Am. Meteorol. Soc.*, **93 (6)**, 845–859, doi:10.1175/BAMS-D-11-00145.1.

Haenel, F. J., and Coauthors, 2015: Reassessment of MIPAS age of air trends and variability. *Atmos. Chem. Phys.*, **15 (15)**, 13 161–13 176, doi:10.5194/acp-15-13161-2015.

Hall, T. M., and R. A. Plumb, 1994: Age as a diagnostic of stratospheric transport. *J. Geophys. Res.*, **99 (D1)**, 1059–1070, doi:10.1029/93JD03192.

Hall, T. M., and D. W. Waugh, 1998: Influence of nonlocal chemistry on tracer distributions: Inferring the mean age of air from SF6. *J. Geophys. Res.: Atmos.*, **103 (D11)**, 13 327–13 336, doi:10.1029/98JD00170.

Hall, T. M., D. W. Waugh, K. A. Boering, and R. A. Plumb, 1999: Evaluation of transport in stratospheric models. *J. Geophys. Res.*, **104 (D15)**, 18 815–18 839, doi:10.1029/1999JD900226.

Hardiman, S. C., N. Butchart, and N. Calvo, 2014: The morphology of the Brewer-Dobson circulation and its response to climate change in CMIP5 simulations. *Q. J. R. Meteorol. Soc.*, **140 (683)**, 1958–1965, doi:10.1002/qj.2258.

Hardiman, S. C., P. Lin, A. A. Scaife, N. J. Dunstone, and H.-L. Ren, 2017: The influence of dynamical variability on the observed Brewer-Dobson circulation trend. *Geophys. Res. Lett.*, **44 (6)**, 2885–2892, doi:10.1002/2017GL072706, 2017GL072706.

Hassler, B., G. E. Bodeker, S. Solomon, and P. J. Young, 2011: Changes in the polar vortex: Effects on antarctic total ozone observations at various stations. *Geophys. Res. Lett.*, **38 (1)**, doi:10.1029/2010GL045542, l01805.

Haynes, P., and E. Shuckburgh, 2000: Effective diffusivity as a diagnostic of atmospheric transport 1. Stratosphere. *J. Geophys. Res.*, **105**, 777–794.

Haynes, P. H., M. E. McIntyre, T. G. Shepherd, C. J. Marks, and K. P. Shine, 1991: On the âĂIJdownward controlâĂİ of extratropical diabatic circulations by eddy-induced mean zonal forces. *J. Atmos. Sci.*, **48 (4)**, 651–678, doi:10.1175/1520-0469(1991)048<0651:OTCOED>2.0.CO;2.

Hegglin, M. I., and T. G. Shepherd, 2009: Large climate-induced changes in ultraviolet index and stratosphere-to-troposphere ozone flux. *Nature Geosci.*, **2 (10)**, 687–691, doi:10.1038/ngeo604.

Held, I. M., and M. J. Suarez, 1994: A proposal for the intercomparison of the dynamical cores of atmospheric general circulation models. *Bull. Amer. Meteor. Soc.*, **75**, 1825–1830, doi:10.1175/1520-0477(1994)075<1825:APFTIO>2.0.CO;2.

Holzer, M., and T. M. Hall, 2000: Transit-Time and Tracer-Age Distributions in Geophysical Flows. *J. Atmos. Sci.*

Johnson, D. G., W. Jucks, W. A. Traub, K. V. Chance, G. C. Toon, J. M. R. Iii, and M. P. Mccormick, 1999: Stratospheric age spectra derived from observations of water vapor and methane. *J. Geophys. Res.*, **104 (D17)**, 21 595–21 602.

Kanu, A. M., L. L. Comfort, T. P. Guilderson, P. J. Cameron-Smith, D. J. Bergmann, E. L. Atlas, S. Schauffler, and K. A. Boering, 2016: Measurements and modeling of contemporary radiocarbon in the stratosphere. *Geophys. Res. Lett.*, **43 (3)**, 1399–1406, doi:10.1002/2015GL066921, 2015GL066921.

Karion, A., C. Sweeney, P. Tans, and T. Newberger, 2010: AirCore: An Innovative Atmospheric Sampling System, Journal of Atmospheric and Oceanic Technology. *J. Atmos. Ocean Tech.*, **27**, 1839–1853, doi:10.1175/2010JTECHA1448.1.

Kida, H., 1983: General circulation of air parcels and transport characteristics derived from a hemispheric GCM. 2. Very long-term motions of air parcels in the troposphere and stratosphere. *J. Meteorol. Soc. Japan*, **61 (4)**, 510–523.

Kobayashi, C., and T. Iwasaki, 2016: Brewer-dobson circulation diagnosed from jra-55. *J. Geophys. Res.: Atmos.*, **121 (4)**, 1493–1510, doi:10.1002/2015JD023476, 2015JD023476.

Kobayashi, S., and Coauthors, 2015: The JRA-55 Reanalysis: General Specifications and Basic Characteristics. *J. Meteorol. Soc. Japan*, **93 (1)**, 5–48, doi:10.2151/jmsj.2015-001.

Kovács, T., and Coauthors, 2017: Determination of the atmospheric lifetime and global warming potential of sulfur hexafluoride using a three-dimensional model. *Atmos. Chem. Phys.*, **17 (2)**, 883–898, doi:10.5194/acp-17-883-2017.

Kushner, P. J., and L. M. Polvani, 2006: Stratosphere-troposphere coupling in a relatively simple AGCM: Impact of the seasonal cycle. *J. Climate*, **19 (21)**, 5721–5727, doi:10.1175/JCLI4007.1.

Legras, B., B. Joseph, and F. Lefèvre, 2003: Vertical diffusivity in the lower stratosphere from Lagrangian back-trajectory reconstructions of ozone profiles. *J. Geophys. Res.*, **108 (D18)**, 4562, doi:10.1029/2002JD003045.

Leibensperger, E. M., and R. A. Plumb, 2014: Effective diffusivity in baroclinic flow. *J. Atmos. Sci.*, **71 (3)**, 972–984, doi:10.1175/JAS-D-13-0217.1.

Li, F., J. Austin, and J. Wilson, 2008: The Strength of the Brewer–Dobson Circulation in a Changing Climate: Coupled Chemistry–Climate Model Simulations. *J. Climate*, **21 (1)**, 40–57, doi:10.1175/2007JCLI1663.1.

Lin, P., Y. Ming, and V. Ramaswamy, 2015: Tropical climate change control of the lower stratospheric circulation. *Geophys. Res. Lett.*, **42 (3)**, 941–948, doi: 10.1002/2014GL062823, 2014GL062823.

Lin, S.-J., 2004: A "Vertically Lagrangian" Finite-Volume Dynamical Core for Global Models. *Monthly Weather Review*, **132 (10)**, 2293–2307, doi:10.1175/1520-0493(2004)132<2293:AVLFDC>2.0.CO;2.

Linz, M., R. A. Plumb, E. P. Gerber, and A. Sheshadri, 2016: The relationship between age of air and the diabatic circulation of the stratosphere. *J.. Atmos. Sci.*, **73 (11)**, 4507–4518, doi:10.1175/JAS-D-16-0125.1.

Livesey, N. J., and Coauthors, 2011: Earth observing system (eos) aura microwave limb sounder (mls) version 3.3 level 2 data quality and description document. Tech. Rep. 3.3x-1.0, Jet Propulsion Laboratory, Pasadena, California.

Lorenz, D. J., and D. L. Hartmann, 2001: Eddy-zonal flow feedback in the Southern Hemisphere. *J. Atmos. Sci.*, **58 (21)**, 3312–3327, doi:10.1175/1520-0469(2001)058<3312:EZFFIT>2.0.CO;2.

Mahieu, E., and Coauthors, 2014: Recent Northern Hemisphere stratospheric HCl increase due to atmospheric circulation changes. *Nature*, **515 (7525)**, 104–7, doi: 10.1038/nature13857.

Marsh, D. R., M. J. Mills, D. E. Kinnison, J.-F. Lamarque, N. Calvo, and L. M. Polvani, 2013: Climate Change from 1850 to 2005 Simulated in CESM1(WACCM). *J. Climate*, **26 (19)**, 7372–7391, doi:10.1175/JCLI-D-12-00558.1.

McIntyre, M. E., and T. N. Palmer, 1984: The 'surf zone' in the stratosphere. *J. Atmos. Terrestrial Phys.*, **46**, 825–849, doi:10.1016/0021-9169(84)90063-1.

McLandress, C., and T. G. Shepherd, 2009: Simulated Anthropogenic Changes in the Brewer-Dobson Circulation, Including Its Extension to High Latitudes. *J. Climate*, **22 (6)**, 1516–1540, doi:10.1175/2008JCLI2679.1.

Moore, F. L., E. A. Ray, K. H. Rosenlof, J. W. Elkins, P. Tans, A. Karion, and C. Sweeney, 2014: A cost-effective trace gas measurement program for long-term monitoring of the stratospheric circulation. *Bull. Am. Meteorol. Soc.*, **95 (1)**, 147–155, doi:10.1175/BAMS-D-12-00153.1.

Morgenstern, O., and Coauthors, 2017: Review of the global models used within phase 1 of the Chemistry–Climate Model Initiative (CCMI). *Geosci. Model Devel.*, **10 (2)**, 639–671, doi:10.5194/gmd-10-639-2017.

Mote, P. W., and Coauthors, 1996: An atmospheric tape recorder: The imprint of tropical tropopause temperatures on stratospheric water vapor. *J. Geophys. Res.: Atmos.*, **101 (D2)**, 3989–4006, doi:10.1029/95JD03422.

Murgatroyd, R. J., and F. Singleton, 1961: Possible meridional circulations in the stratosphere and mesosphere. *Q. J. R. Meteorol. Soc.*, **87 (372)**, 125–135, doi: 10.1002/qj.49708737202.

Nakamura, N., 1996: Two-dimensional mixing, edge formation, and permeability diagnosed in an area coordinate. *J. Atmos. Sci.*, **53 (11)**, 1524–1537, doi:10.1175/1520-0469(1996)053<1524:TDMEFA>2.0.CO;2.

Neale, R. B., J. Richter, S. Park, P. H. Lauritzen, S. J. Vavrus, P. J. Rasch, and M. Zhang, 2013: The Mean Climate of the Community Atmosphere Model (CAM4) in Forced SST and Fully Coupled Experiments. *J. Climate*, **26 (14)**, 5150–5168, doi:10.1175/JCLI-D-12-00236.1.

Neu, J. L., and R. A. Plumb, 1999: Age of air in a "leaky pipe" model of stratospheric transport. *J. Geophys. Res.*, **104 (D16)**, 19 243–19 255, doi:10.1029/1999JD900251.

Newman, P. A., M. R. Schoeberl, and R. A. Plumb, 1986: Horizontal mixing coefficients for two-dimensional chemical models calculated from national meteorological center data. *J. Geophys. Res.: Atmos.*, **91 (D7)**, 7919–7924, doi:10.1029/JD091iD07p07919.

Oberländer-Hayn, S., and Coauthors, 2016: Is the Brewer–Dobson circulation increasing or moving upward? *Geophys. Res. Lett.*, **43 (4)**, 1772–1779, doi:10.1002/2015GL067545.

Orbe, C., M. Holzer, and L. M. Polvani, 2012: Flux distributions as robust diagnostics of stratosphere-troposphere exchange. *J. Geophys. Res.*, **117 (D1)**, D01 302, doi: 10.1029/2011JD016455.

Orbe, C., M. Holzer, L. M. Polvani, D. W. Waugh, F. Li, L. D. Oman, and P. a. Newman, 2014: Seasonal ventilation of the stratosphere: Robust diagnostics from one-way flux distributions. *J. Geophys. Res.: Atmos.*, **119 (1)**, 293–306, doi:10.1002/2013JD020213.

Paul, J., F. Fortuin, and H. Kelder, 1998: An ozone climatology based on ozonesonde and satellite measurements. *J. Geophys. Res.: Atmos.*, **103 (D24)**, 31 709–31 734, doi: 10.1029/1998JD200008.

Perliski, L. M., S. Solomon, and J. London, 1989: On the interpretation of seasonal variations of stratospheric ozone. *Planet. Space Sci.*, **37 (12)**, 1527 – 1538, doi: http://dx.doi.org/10.1016/0032-0633(89)90143-8.

Ploeger, F., M. Abalos, T. Birner, P. Konopka, B. Legras, R. Müller, and M. Riese, 2015a: Quantifying the effects of mixing and residual circulation on trends of stratospheric mean age of air. *Geophys. Res. Lett.*, **42**, 2047–2054, doi:10.1002/2014GL062927.1.

Ploeger, F., M. Riese, F. Haenel, P. Konopka, R. Müller, and G. Stiller, 2015b: Variability of stratospheric mean age of air and of the local effects of residual circulation and eddy mixing. *J. Geophys. Res.*, **120 (2)**, 716–733, doi:10.1002/2014JD022468.

Plumb, R. A., 1996: A "tropical pipe" model of stratospheric transport. *J. Geophys. Res.: Atmos.*, **101 (D2)**, 3957–3972, doi:10.1029/95JD03002.

Plumb, R. A., 2002: Stratospheric Transport. *J. Meteor. Soc. Japan*, **80 (4)**, 793–809, doi:10.2151/jmsj.80.793.

Plumb, R. A., 2007: Tracer interrelationships in the stratosphere. *Rev. Geophys.*, **45**, RG4005, doi:10.1029/2005RG000179.

Plumb, R. A., and M. K. W. Ko, 1992: Interrelationships between mixing ratios of long-lived stratospheric constituents. *J. Geophys. Res.: Atmos.*, **97 (D9)**, 10 145–10 156, doi: 10.1029/92JD00450.

Plumb, R. A., and Coauthors, 2002: Global tracer modeling during SOLVE: High-latitude descent and mixing. *J. Geophys. Res.: Atmos.*, **107 (D5)**, doi:10.1029/2001JD001023, 8309.

Polvani, L. M., and P. J. Kushner, 2002: Tropospheric response to stratospheric perturbations in a relatively simple general circulation model. *Geophys. Res. Lett.*, **29 (7)**, 40–43, doi:10.1029/2001GL014284.

Polvani, L. M., D. W. Waugh, G. J. P. Correa, and S.-W. Son, 2011: Stratospheric Ozone Depletion: The Main Driver of Twentieth-Century Atmospheric Circulation Changes in the Southern Hemisphere. *J. Climate*, **24 (3)**, 795–812, doi:10.1175/2010JCLI3772.1.

Putnam, W. M., and S.-J. Lin, 2007: Finite–volume transport on various cubed–sphere grids. *J. Comput. Phys.*, **227**, 55–78, doi:10.1016/j.jcp.2007.07.022.

Pyle, J. A., and C. F. Rogers, 1980: A modified diabatic circulation model for stratospheric tracer transport. *Nature*, **287 (5784)**, 711–714, doi:10.1038/287711a0.

Randel, W. J., R. R. Garcia, and F. Wu, 2002: Time-dependent upwelling in the tropical lower stratosphere estimated from the zonal-mean momentum budget. *J. Atmos. Sci.*, **59 (13)**, 2141–2152, doi:10.1175/1520-0469(2002)059<2141:TDUITT>2.0.CO;2.

Ray, E. A., F. L. Moore, J. W. Elkins, K. H. Rosenlof, J. C. Laube, T. Röckmann, D. R. Marsh, and A. E. Andrews, 2017: Quantification of the $SF_6$ lifetime based on mesospheric loss measured in the stratospheric polar vortex. *J. Geophys. Res.: Atmos.*, doi:10.1002/2016JD026198, 2016JD026198.

Ray, E. A., F. L. Moore, K. H. Rosenlof, D. A. Plummer, F. Kolonjari, and K. A. Walker, 2016: An idealized stratospheric model useful for understanding differences between long-lived trace gas measurements and global chemistry-climate model output. *J. Geophys. Res.: Atmos.*, **121 (10)**, 5356–5367, doi:10.1002/2015JD024447, 2015JD024447.

Ray, E. A., and Coauthors, 2010: Evidence for changes in stratospheric transport and mixing over the past three decades based on multiple data sets and tropical leaky pipe analysis. *J. Geophys. Res.*, **115 (D21)**, doi:10.1029/2010JD014206.

Ray, E. A., and Coauthors, 2014: Improving stratospheric transport trend analysis based on SF6 and CO2 measurements. *J. Geophys. Res.: Atmos.*, **119 (24)**, 14,110–14,128, doi:10.1002/2014JD021802, 2014JD021802.

Reinsel, G. C., A. J. Miller, E. C. Weatherhead, L. E. Flynn, R. M. Nagatani, G. C. Tiao, and D. J. Wuebbles, 2005: Trend analysis of total ozone data for turnaround and dynamical contributions. *J. Geophys. Res.: Atmos.*, **110 (D16)**, doi:10.1029/2004JD004662, d16306.

Rienecker, M. M., and Coauthors, 2011: MERRA: NASA's Modern-Era Retrospective Analysis for Research and Applications. *J. Climate*, **24 (14)**, 3624–3648, doi:10.1175/JCLI-D-11-00015.1.

Rosenfield, J. E., M. R. Schoeberl, and M. A. Geller, 1987: A computation of the stratospheric diabatic circulation using an accurate radiative transfer model. *J. Atmos. Sci.*, **44 (5)**, 859–876, doi:10.1175/1520-0469(1987)044<0859:ACOTSD>2.0.CO;2.

Rosenlof, K. H., 1995: Seasonal cycle of the residual mean meridional circulation in the stratosphere. *J. Geophys. Res.*, **100**, 5173–5191.

Schoeberl, M. R., A. R. Douglass, R. S. Stolarski, S. Pawson, S. E. Strahan, and W. Read, 2008: Comparison of lower stratospheric tropical mean vertical velocities. *J. Geophys. Res.: Atmos.*, **113 (D24)**, doi:10.1029/2008JD010221, d24109.

Seinfeld, J. H., and S. N. Pandis, 2006: *Atmospheric Chemistry and Physics: From air pollution to climate change.* 2nd ed., John Wiley Sons, Inc., Hoboken, New Jersey.

Seviour, W. J. M., N. Butchart, and S. C. Hardiman, 2012: The Brewer-Dobson circulation inferred from ERA-Interim. *Q. J. R. Meteorol. Soc.*, **138 (665)**, 878–888, doi: 10.1002/qj.966.

Shepherd, T. G., and C. McLandress, 2011: A Robust Mechanism for Strengthening of the Brewer-Dobson Circulation in Response to Climate Change: Critical-Layer Control of Subtropical Wave Breaking. *J. Atmos. Sci.*, **68 (4)**, 784–797, doi:10.1175/2010JAS3608.1.

Sheshadri, A., R. A. Plumb, and E. P. Gerber, 2015: Seasonal variability of the polar stratospheric vortex in an idealized AGCM with varying tropospheric wave forcing. *J. Atmos. Sci.*, **72**, 2248–2266, doi:10.1175/JAS-D-14-0191.1.

Singh, M. S., and P. A. O'Gorman, 2012: Upward shift of the atmospheric general circulation under global warming: Theory and simulations. *J. Climate*, **25**, 8259–8276, doi: 10.1175/JCLI-D-11-00699.1.

Solomon, S., D. J. Ivy, D. Kinnison, M. J. Mills, R. R. Neely, and A. Schmidt, 2016: Emergence of healing in the Antarctic ozone layer. *Science*, doi:10.1126/science.aae0061.

Solomon, S., K. H. Rosenlof, R. W. Portmann, J. S. Daniel, S. M. Davis, T. J. Sanford, and G.-K. Plattner, 2010: Contributions of stratospheric water vapor to decadal changes in the rate of global warming. *Science*, **327 (5970)**, 1219–1223, doi:10.1126/science.1182488.

Sparling, L. C., J. A. Kettleborough, P. H. Haynes, M. E. McIntyre, J. E. Rosenfield, M. R. Schoeberl, and P. A. Newman, 1997: Diabatic cross-isentropic dispersion in the lower stratosphere. *J. Geophys. Res.*, **102 (D22)**, 25 817–25 829, doi:10.1029/97JD01968.

Stiller, G. P., and Coauthors, 2008: Global distribution of mean age of stratospheric air from MIPAS $SF_6$ measurements. *Atmos. Chem. Phys.*, **8 (3)**, 677–695, doi:10.5194/acp-8-677-2008, URL `http://www.atmos-chem-phys.net/8/677/2008/`.

Stiller, G. P., and Coauthors, 2012: Observed temporal evolution of global mean age of stratospheric air for the 2002 to 2010 period. *Atmos. Chem. Phys.*, **12 (7)**, 3311–3331, doi:10.5194/acp-12-3311-2012.

Stolarski, R. S., A. R. Douglass, E. E. Remsberg, N. J. Livesey, and J. C. Gille, 2012: Ozone temperature correlations in the upper stratosphere as a measure of chlorine content. *J. Geophys. Res.: Atmos.*, **117 (D10)**, doi:10.1029/2012JD017456, d10305.

Strahan, S. E., and Coauthors, 2011: Using transport diagnostics to understand chemistry climate model ozone simulations. *J. Geophys. Res.*, **116 (D17302)**, doi: 10.1029/2010JD015360.

Swanson, D. C., 2000: *Signal processing for intelligent sensor systems.* CRC Press.

Thompson, D. W. J., and S. Solomon, 2002: Interpretation of recent Southern Hemisphere climate change. *Science*, **296 (5569)**, 895–9, doi:10.1126/science.1069270.

Totterdill, A., T. Kovacs, J. C. Gomez Martin, W. Feng, and J. M. C. Plane, 2015: Mesospheric Removal of Very Long-Lived Greenhouse Gases SF6 and CFC-115 by Metal Reactions, Lyman-$\alpha$ Photolysis, and Electron Attachment. *J. Phys. Chem. A*, **119 (10)**, 2016–2025, doi:10.1021/jp5123344.

US Environmental Protection Agency, 2016: Climate change indicators in the United States. EPA 430-R-16-004, URL `https:// www.epa.gov/climate-indicators`.

Volk, C. M., and Coauthors, 1997: Evaluation of source gas lifetimes from stratospheric observations. *J. Geophys. Res.*, **102 (D21)**, 25 543–25 564, doi:10.1029/97JD02215.

von Clarmann, T., and Coauthors, 2003: Retrieval of temperature and tangent altitude pointing from limb emission spectra recorded from space by the Michelson Interferometer for Passive Atmospheric Sounding (MIPAS). *J. Geophys. Res.: Atmos.*, **108 (D23)**, doi: 10.1029/2003JD003602, 4736.

von Clarmann, T., and Coauthors, 2009: Retrieval of temperature, $H_2O$, $O_3$, $HNO_3$, $CH_4$, $N_2O$, $ClONO_2$ and ClO from MIPAS reduced resolution nominal mode limb emission measurements. *Atmos. Meas. Tech.*, **2 (1)**, 159–175, doi:10.5194/amt-2-159-2009.

Waugh, D., and T. M. Hall, 2002: Age of stratospheric air: Theory, observations, and models. *Rev. Geophys.*, **40 (4)**, 1010, doi:10.1029/2000RG000101.

Zhang, L., D. J. Jacob, X. Liu, J. A. Logan, K. Chance, A. Eldering, and B. R. Bojkov, 2010: Intercomparison methods for satellite measurements of atmospheric composition: application to tropospheric ozone from tes and omi. *Atmos. Chem. Phys.*, **10 (10)**, 4725–4739, doi:10.5194/acp-10-4725-2010.